

University of South Alabama

JagWorks@USA

Theses and Dissertations

Graduate School

12-2022

Seeing the Big Picture: System Architecture Trends in Endoscopy and LED-Based hyperspectral Subsystem Intergration

Craig M. Browning

Follow this and additional works at: https://jagworks.southalabama.edu/theses_diss



Part of the Bioimaging and Biomedical Optics Commons, Biomedical Devices and Instrumentation Commons, Cancer Biology Commons, Digestive System Diseases Commons, Gastroenterology Commons, Investigative Techniques Commons, Neoplasms Commons, Oncology Commons, Other Medicine and Health Sciences Commons, Research Methods in Life Sciences Commons, Semiconductor and Optical Materials Commons, and the Systems and Integrative Engineering Commons

SEEING THE BIG PICTURE: SYSTEM ARCHITECTURE TRENDS IN
ENDOSCOPY AND LED-BASED HYPERSPECTRAL SUBSYSTEM INTEGRATION

A Dissertation

Submitted to the Graduate Faculty of the
University of South Alabama
in partial fulfillment of the
requirements for the degree of

Doctorate of Philosophy

in

Systems Engineering

by

Craig M. Browning
M. S., University of South Alabama, 2018
December 2022

ACKNOWLEDGMENTS

I hope to convey my immense gratitude for the blessings, experiences and opportunities afforded to me throughout my journey in higher education. This section is one of the most important to me because without these people and so many more not listed, I would not be the man I am today or have achieved these accomplishments. Dr. Silas Leavesley, thank you for the many years as my professor, mentor and friend. Your support and counsel have produced the confidence I have in my work here and the projects to come. Dr. Thomas Rich, your advice and steadfast mentoring has helped me to stay cool under pressure and refined my research to cut through the jargon and ask the right questions. The knowledge, patience and loyalty you both give to your work and lab group has produced many great minds and I am thankful to have been a part of it. Thank you for completely changing the way I engineer Dr. Cloutier. Your training, commitment and counsel has made me a better engineer and I am forever grateful for it. Dr. Di Palma and Dr. Gong, I appreciate all of the viewpoints, advice and knowledge you have passed on to me. Finally, to my parents, sister, grandparents, uncle and close friends, thank you for the love, support, prayers, encouragement and (at times) distractions throughout this journey. The breadth of knowledge my family has passed on to me has made me the engineer I am today. Thank you for being there during the highs and lows and imparting wisdom to help me persevere. Thank you all!

TABLE OF CONTENTS

| | Page |
|---|------|
| LIST OF TABLES | v |
| LIST OF FIGURES | vii |
| LIST OF SYMBOLS AND ABBREVIATIONS | x |
| ABSTRACT..... | xiii |
| CHAPTER I: INTRODUCTION..... | 1 |
| Objective..... | 3 |
| CHAPTER II: BACKGROUND | 5 |
| Endoscopy..... | 5 |
| Hyperspectral Imaging..... | 7 |
| Spectral Data Analysis..... | 10 |
| Systems Engineering Tools and Analyses | 12 |
| CHAPTER III: ENDOSCOPY LIFETIME SYSTEMS ARCHITECTURE: SCOPING OUT THE PAST TO DIAGNOSE THE FUTURE TECHNOLOGY | 14 |
| Abstract..... | 14 |
| Introduction..... | 15 |
| Historical Overview | 19 |
| Presenting, the Endoscope | 29 |
| Conclusion | 45 |
| CHAPTER IV: EXCITATION-SCANNING HYPERSPECTRAL VIDEO ENDOSCOPY: ENHANCING THE LIGHT AT THE END OF THE TUNNEL..... | 49 |
| Abstract..... | 49 |
| Introduction..... | 50 |
| Methods..... | 55 |
| Results and Discussion | 68 |
| Future work..... | 87 |
| CHAPTER V: MICROSCOPY IS BETTER IN COLOR: DEVELOPMENT OF A STREAMLINED SPECTRAL LIGHT PATH FOR REAL-TIME MULTIPLEX FLUORESCENCE MICROSCOPY..... | 90 |

| | |
|---|-----|
| Abstract | 90 |
| Introduction..... | 92 |
| Methods..... | 96 |
| Results..... | 104 |
| Discussion..... | 120 |
| CHAPTER VI: DISSERTATION PORTFOLIO SUMMARY AND FUTURE DIRECTIONS..... | 128 |
| REFERENCES | 135 |
| APPENDICES | 151 |
| Appendix A: Supplemental Document 1 | 151 |
| Appendix B: Supplemental Document 2 | 153 |
| Appendix C: Copyright Permission | 162 |
| BIOGRAPHICAL SKETCH | 163 |

LIST OF TABLES

| Table | Page |
|--|------|
| 1. Pugh matrix ranking alternative technologies compared to the gold standard. | 44 |
| 2. Key parameters used for ray trace simulations of the alpha phase multi-furcated light guide..... | 57 |
| 3. Key parameters used for ray trace simulations of the beta phase multifurcated light guide..... | 62 |
| 4. Manufacturer-supplied properties of the high-powered surface mount LEDs used in the beta phase simulations and in the alpha phase prototype. | 65 |
| 5. Summary of results from the alpha phase multi-branched solid light guide ray tracing modeling. | 70 |
| 6. Individual geometric parameters simulated in TracePro for iterations of the beta phase multi-branched solid light guide. | 80 |
| 7. Tabulated data from Figure 15 comparing the required (Column 2) and desired (Column 3) transmission of each λ LED (from Table 4) to the simulated (Column 4) transmission results (also plotted in Figure 14.D). | 87 |
| 8. Optical components used for ray trace simulations. | 98 |
| 9. Two microscope platform configurations including the components and parameters used for imaging. | 102 |

| | |
|--|-----|
| 10. Cellular components labeled and the corresponding fluorescent label for six-labeled slides used for spectral imaging feasibility testing. | 103 |
| 11. Transmission maximums for each lens configuration using the three different diameter mirrors..... | 105 |
| Appendix Table | |
| A1. Product specifications for the LEDs used in prototype light source..... | 153 |

LIST OF FIGURES

| Figure | Page |
|---|------|
| 1. Condensed system architecture for the original (Lichtleiter) endoscope..... | 21 |
| 2. System architecture for the endoscope integrating the electric light bulb.. | 23 |
| 3. The endoscope milestone involving significant optical updates..... | 26 |
| 4. Digital imaging endoscope system architecture | 28 |
| 5. Current endoscope condensed system architecture..... | 30 |
| 6. Trends for components within subsystems..... | 34 |
| 7. Timeline comparing technology invention dates to the time it was integrated into endoscopy | 36 |
| 8. Mind map for design of a next generation endoscopic system..... | 37 |
| 9. Rendering of the alpha phase multi-branched solid light guide in ray tracing software for simulated optical analysis..... | 58 |
| 10. A systems architecture internal block diagram view of the electric interface of the hyperspectral endoscopic light source, specifically for the alpha design proof-of-concept light source..... | 60 |
| 11. Complete proof-of-concept spectral endoscope system overview..... | 60 |
| 12. TracePro rendering of the models used in simulation to observe the transmission of light through a multi-branched solid light guide..... | 68 |

| | |
|---|-----|
| 13. Results from benchtop testing the proof-of-concept light source for spectral LED (λ LED) | 74 |
| 14. Results of the ray tracing simulations for the beta light guide models showing optical transmission as a function of % transmission vs. branch illuminated | 84 |
| 15. Comparison of the required outputs of each λ LED to the theoretical output of the simulation model Wave Design 2 in Figure 12.I | 85 |
| 16. Conceptual illustration for the spectral illuminator to combine optical output from multiple wavelength-specific LEDs located in a ring and reflected to a common location | 97 |
| 17. Light path schematics for the two spectral illumination pathways used in hyperspectral image acquisition..... | 102 |
| 18. Fabrication of the dual mirror spectral illuminator prototype | 107 |
| 19. Prototype sensitivity response to optical component position and comparison to ray trace simulations | 109 |
| 20. Spectral image data acquired from a 6-label slide using a TFTF-based system for excitation-scanning spectral imaging microscopy | 116 |
| 21. Spectral image data acquired from a 6-label slide using the prototype LED-based system for excitation-scanning spectral imaging microscopy | 118 |
| 22. A side-by-side comparison excitation-scanning spectral image data acquired from the same field of view using: (a) a TFTF-based system when imaging with 38 wavelength bands, (b) a TFTF-based system when imaging with 13 wavelength bands (c) and the prototype LED-based system when imaging with 13 wavelength bands. | 120 |

Appendix Figures

A1. Image data corresponding to Figure 13.E where reflectance spectral images have been divided by wavelength band and false colored for visualization. 151

A2. Data from Figure A1 and corresponding Figure 13.E, where the look-up table for each wavelength band has been scaled independently. 152

A3. Summary of the TracePro simulation irradiance data for a one lens configuration. 154

A4. LED measurements for irradiance control. 155

A5. Test for photobleaching on the TFTF-based system and the LED-based system for repeated imaging (5x) of the same FOV..... 156

A6. Manufacturer-supplied spectral data for the labels used for the labels used in this study..... 157

A7. Validation of spectral specificity for the TFTF-based system..... 158

A8. Validation of spectral specificity for the LED-based system. 159

A9. Comparison of individual endmember spectra utilized for linear unmixing for the TFTF-based system and the LED-based system..... 160

A10. A comparison of manufacturer-supplied spectral data and measured excitation spectrum using both the TFTF- and LED-based spectral light sources..... 161

LIST OF SYMBOLS AND ABBREVIATIONS

AF = Autofluorescence

AFI = Autofluorescence Imaging

AI = Artificial Intelligence

AOTF = Acousto-Optic Tunable Filters

CAD = Computer Aided Design

CCD = Charge Coupled Device

CE = Chromoendoscopy

CMOS = Complementary Metal Oxide Semiconductor

CNN = Convolutional Neural Network

ConOps = Concept of Operations

CT = Coherence Tomography

dsDNA = Double Stranded DNA

DSP = Digital Signal Processor

FICE = Flexible Intelligent Color Enhancement

FL = Focal Length

FOV = Field of View

FWHM = Full Width at Half Maximum

GI = Gastrointestinal Tract

HSI = Hyperspectral Imaging

IBD = Internal Block Diagram

ICA = Independent Component Analysis

LCTF = Liquid Crystal Tunable Filter

LED = Light Emitting Diode

LLG = Liquid Light Guide

LP = Long-pass

MBSE = Model Based Systems Engineering

ML = Machine Learning

MRI = Magnetic Resonance Imaging

NA = Numerical Aperture

NBI = Narrow-Band Imaging

NIR = Near Infrared

NN = Neural Network

NPP = Nuclear Pore Protein

OCT = Optical Coherence Tomography

PBS = Phosphate Buffered Saline

PCA = Principle Component Analysis

PCB = Printed Circuit Board

R-EBUS = Radial Endobronchial Ultrasound

RGB = Red-Green-Blue

RMS = Root Mean Square

ROI = Region of Interest

SE = Systems Engineering
SNR = Signal to Noise Ratio
SVM = Support Vector Machines
TFTF = Thin-Filmed Tunable Filters
TIR = Total Internal Reflectance
UAV = Unmanned Aerial Vehicle
UV = Ultraviolet
VE = Virtual Endoscopy
WLB = White Light Bronchoscopy
WLE = White Light Endoscopy
 λ LED = Wavelength-Specific LED
 $^{\circ}$ = Degrees
cd = Candela
lm = Lumen
 μ W = Microwatt
mW = Milliwatt
mA = Milliamps
V = Volts
mm = Millimeter
cm = Centimeter
m = Meter
ms = Millisecond
s = Second

ABSTRACT

Browning, Craig M., Ph.D., University of South Alabama, December 2022. Seeing the Big Picture: System Architecture Trends in Endoscopy and LED-Based Hyperspectral Subsystem Integration. Chair of Committee: Silas Leavesley, Ph.D.

Early-stage colorectal lesions remain difficult to detect. Early development of neoplasia tends to be small (less than 10 mm) and flat and difficult to distinguish from surrounding mucosa. Additionally, optical diagnosis of neoplasia as benign or malignant is problematic. Low rates of detection of these lesions allow for continued growth in the colorectum and increased risk of cancer formation. Therefore, it is crucial to detect neoplasia and other non-neoplastic lesions to determine risk and guide future treatment. Technology for detection needs to enhance contrast of subtle tissue differences in the colorectum and track multiple biomarkers simultaneously.

This work implements one such technology with the potential to achieve the desired multi-contrast outcome for endoscopic screenings: hyperspectral imaging. Traditional endoscopic imaging uses a white light source and a RGB detector to visualize the colorectum using reflected light. Hyperspectral imaging (HSI) acquires an image over a range of individual wavelength bands to create an image hypercube with a wavelength dimension much deeper and more sensitive than that of an RGB image. A hypercube can consist of reflectance or fluorescence (or both) spectra depending on the filtering optics involved. Prior studies using HSI in endoscopy have normally involved *ex vivo* tissues or

optics that created a trade-off between spatial resolution, spectral discrimination and temporal sampling.

This dissertation describes the systems design of an alternative HSI endoscopic imaging technology that can provide high spatial resolution, high spectral distinction and video-rate acquisition *in vivo*. The hyperspectral endoscopic system consists of a novel spectral illumination source for image acquisition dependent on the fluorescence excitation (instead of emission). Therefore, this work represents a novel contribution to the field of endoscopy in combining excitation-scanning hyperspectral imaging and endoscopy. This dissertation describes: 1) systems architecture of the endoscopic system in review of previous iterations and theoretical next-generation options, 2) feasibility testing of a LED-based hyperspectral endoscope system and 3) another LED-based spectral illuminator on a microscope platform to test multi-spectral contrast imaging.

The results of the architecture point towards an endoscopic system with more complex imaging and increased computational capabilities. The hyperspectral endoscope platform proved feasibility of a LED-based spectral light source with a multi-furcated solid light guide. Another LED-based design was tested successfully on a microscope platform with a dual mirror array similar to telescope designs. Both feasibility tests emphasized optimization of coupling optics and combining multiple diffuse light sources to a common output. These results should lead to enhanced imagery for endoscopic tissue discrimination and future optical diagnosis for routine colonoscopy.

CHAPTER I: INTRODUCTION

The adage “Every Picture Tells a Story” has been quoted through history from Charlotte Brontë’s novel *Jane Eyre* in 1847 to Doan’s Backache Kidney Pills advertisement at the beginning of the 20th century to Rod Stewart’s album and title track released in 1971 and likely every art class in between¹⁻³. Art and history connoisseurs can take this phrase to heart when reflecting on a given picture. Now imagine the same relationship when translated to clinicians and biomedical imaging. Biomedical imagery has told “stories” for centuries, from external skin rashes to synaptic nerve transmission. Modern medicine continues to find new, deeper stories within biomedical images through multidimensional data acquisition. The goal of this dissertation is to develop a next generation tool for enhancing biomedical imaging, specifically endoscopy.

Endoscopy has been the gold standard screening procedure for viewing internal organs or cavities for more than a half of a century. Endoscopic tools have allowed visualization of the entire gastrointestinal (GI) tract, the respiratory tract to the level of the bronchioles and numerous body cavities accessible for lower risk, minimally invasive laparoscopic surgeries. This work will focus on GI related endoscopes (esophagogastroduodenoscopes, colonoscopes and sigmoidoscopes). Colonoscopy is the standard procedure to screen for colorectal cancer; the 3rd highest risk cancer for incidence and mortality in the United States⁴⁻⁷. The 5-year survival rates of colorectal

cancer for local or Stage I, regional or Stage II/III and distant or Stage IV are 90%, 71% and 14%, respectively, for all ages⁷. Studies have shown a 20% - 25% miss rate for small (≤ 10 mm) and/or flat, sessile polyps regardless of location and risk assessment⁸⁻¹². Missed detection of early-stage colorectal cancer leads to increased risk of mortality. Therefore, enhanced contrast visualization could increase the detection of early, small polyp growths in the colorectum. Possible enhancements include: improved contrast between lesion and surrounding mucosa, assessment of lesion depth or penetration into the mucosa or risk assessment (non-cancerous, pre-cancerous or cancerous). Enhanced contrast would in turn improve detection and characterization of all polyps providing increased information for diagnosis.

This dissertation contains a historical review with coinciding systems architecture and a series of experiments to evaluate the feasibility of excitation-scanning hyperspectral imaging (HSI) for endoscopic procedures. Hyperspectral imaging is a spectroscopic technique which acquires spatial image data over a range of wavelength intervals creating a 3-dimensional hypercube. The combination of all wavelength channels provides a spectrum per image pixel. The wavelength-specific interaction of illumination with a given substance in the field of view (FOV) creates a unique spectral signature. The utility of HSI has been observed across studies in remote sensing, agriculture monitoring, food processing, archaeology, historical artifact restoration and *ex vivo* medical imaging¹³⁻¹⁷. Furthermore, within a subset of these studies, hyperspectral imaging has provided additional information by utilizing both reflectance and (endogenous or exogenous) fluorescence spectroscopic analysis. The advantages of HSI in these studies include: biomarker discrimination, nutrient content, component isolation

and component separation. These factors would benefit endoscopy by generating increased contrast between structures, determining abundance and classifying normal and lesional tissue. Hence, the objective of this work is provided below and the following chapters detail projects completed to meet these goals.

Objective

Integrate hyperspectral imaging into an endoscopic platform to provide reflectance, fluorescence or mixed spectroscopic data as a technique to enhance contrast in endoscopic screening.

The approach to meet the objective is as follows: Chapter II provides a literature review of the fundamental aspects of this work to support the subsequent manuscripts. A historical review of endoscopy from a systems engineering perspective is provided in Chapter III. Additionally, systems architecture for endoscopy was constructed and concepts for a future endoscopic system are outlined. Chapter IV details benchtop feasibility of a LED-based excitation-scanning endoscopic platform and the potential for future clinical trials. A different LED-based spectral illuminator was tested (Chapter V) on a microscope platform for excitation-scanning hyperspectral imaging of multi-labeled samples. This has been organized as a dissertation by portfolio with Chapter III corresponding to a manuscript that is ready for journal submission and Chapters IV and V corresponding to articles published in peer-reviewed scientific journals (details at the beginning of each chapter). Finally, Chapter VI reviews all the work of the previous chapters to show the “big picture” and validate the objective. The appendices provide additional information and data for the testing in Chapters IV and V.

The novelty of this dissertation comes in two parts: the systems engineering analysis of the endoscope and the LED-based hyperspectral modules. To our knowledge, this is the first of its kind of a systems architecture analysis for the endoscopic system. The analysis is unique architecting historic milestones in the lifetime of the system and using these models to track the trends in technology. Documenting this systems architecture could be a basis for future systems engineering design for the endoscope system or translation to other biomedical systems. In addition, there is novelty in the optical geometry designs of LED-based array for hyperspectral imaging. These systems eliminate excitation filtering, mechanical stress and allow for high-speed excitation-scanning hyperspectral imaging that is no longer dependent on mechanical tuning for acquisition speeds. An endoscope based on these LED-based hyperspectral imaging designs could ultimately produce high definition, video-rate, spectroscopically diverse image data for analysis, contrast and enhancements.

CHAPTER II: BACKGROUND

The background for this work is multidisciplinary and covers a diverse knowledge base for the different aspects contained in these manuscripts. The literature is divided into four sections: endoscopy, hyperspectral imaging, data science or analysis methods and systems engineering tools for decision-making and multi-objective trade-off analyses. These categories are self-contained; however, this work is interdisciplinary and the background will highlight the necessary connections between fields.

Endoscopy

As mentioned previously, endoscopy is the gold standard for screening luminal organs and cavities *in situ*. For the specific case of colonoscopy, colonoscopes are a tool to screen the colon, typically visualized with a broad-band white light source. The limitations of current colonoscopy techniques include undetected small (≤ 10 mm) polyps (miss rates: 20%-25%)^{8,9,11,12} that can be correlated to early lesion growth or flat, sessile lesions. Colorectal screening is recommended every 5-10 years for adults ages 50 and older. Shorter screening intervals may be advised based upon risk factors. Based on colorectal polyp growth rates^{18,19}, 5-10 years of growth, if cancerous, causes the survivability rate of the patient to diminish. This is one of several factors that explain why colorectal cancer is ranked 3rd for incidence and mortality rates⁴⁻⁷. A major

limitation in detecting small neoplasia or polyps is the minimal contrast with surrounding mucosa. The reflected white light does not highlight a noticeable difference between tissue types for very small lesions and flat or depressed lesions. Due to low contrast, other screening techniques have been developed to aid in visualization of the colorectum: chromoendoscopy, narrow-band imaging and autofluorescence imaging.

Chromoendoscopy (CE) is an addition to white light endoscopy (WLE) by introducing a blue dye that adheres to the mucosa to express structures, pits and crevices to enhance dysplasia. An alternative is electronic or virtual CE which uses bandwidths of light and software to replicate a similar outcome as standard CE (Pentax's i-scan or Fujinon's flexible spectral image color enhancement – FICE). Overall, the enhancements provided by CE have produced nominal improvements to detection accuracy of abnormal growth in the colorectum when compared to WLE (studies are post-procedure optical diagnoses of images and verified by histopathology)²⁰⁻²⁵. The limitations of standard CE include additional time and cost of the dye that provide minimal overall improvements to screenings. Virtual CE introduces the possibility of digital aberrations during the screening that could obscure optical diagnoses.

Narrow-band imaging (NBI) selects narrow bandwidths of the WLE light source to provide illumination peaks in the blue and green region of the spectrum. Illumination at these wavelengths is preferentially absorbed by the vasculature creating a darker, brownish contrast to the mucosa. Lesions tend to have a higher density of blood vessels so NBI will create a condensed, brown region disrupting the normal vasculature pattern. NBI is paired often with magnification endoscopy to focus on a region of interest (ROI) for a highly defined vascularized image^{26,27}. Comparing NBI to WLE, studies show an

increase in sensitivity (true positive rate) for optical diagnosis but a decrease in specificity (true negative rate)^{20,21,28-30}. The limitations of NBI include reduced illumination or visualization due to filtering the light source and the vasculature contrast has not provided a definitive measure of lesions.

Autofluorescence imaging (AFI) uses a separate light source and path to illuminate with an excitation band in the 370-470 nm range (usually 408 nm) and detect autofluorescence of the tissue. This range excites molecular components such as collagen or protoporphyrin IX (collects in tumor cells) to create the autofluorescent contrast between non-lesional and lesional tissue³¹. Similar to NBI, studies comparing AFI to alternative imaging techniques occasionally show an increase in sensitivity of histological predictions but a decrease in specificity^{20,29,32,33}. Limiting factors in the use of AFI include the inherent low signal output of autofluorescence, especially single source autofluorescence. When comparing the autofluorescence of normal and lesion tissue, the spectra shape is similar but the power difference is the delimiter and some cases can be difficult to separate.

Hyperspectral Imaging

A hyperspectral image is a two-dimensional (spatial) image acquired over a range of wavelengths creating a three-dimensional hypercube. The pixels of a hyperspectral image are referred to as voxels (volumetric pixels) with the spectroscopic data as the depth information. The light acquired through reflectance, fluorescence or transmission creates the unique spectrum for each pixel. Spectroscopic data provide a new layer of information within an image and can be used to enhance the contrast between image

components. HSI originated with satellite imagery and remote sensing to show spectroscopic differences between waterfronts, vegetation and mineral aggregates^{14,16,34}. An extension of remote sensing has benefitted agriculture through crop monitoring of water content, nutrient distribution and pest infestation^{15,35-37}. Alternatively, archaeologists have harnessed satellite HSI to determine materials and layouts of ancient building remnants^{16,38}. Other examples of HSI utility include food analysis and historic document restoration. Studies have shown the ability to determine water, sugar or fat content in certain types of food^{15,39,40}. HSI has been used to digitally preserve and restore historical documents through scanning and digitally removing stains and aging by analysis of spectroscopic differences^{41,42}.

Biomedical imaging has benefitted from hyperspectral imaging in studies of tissue classification, both *ex vivo*^{43,44} and *in vivo*⁴⁵⁻⁴⁸. Within these studies, a range of techniques have been used to acquire hyperspectral biomedical image data with initial success in endoscopy. These include: point scanning, line scanning, spectral scanning and snapshot.

Point scanning or whiskbroom HSI scans a FOV pixel by pixel (or small group of pixels) and measures the spectrum by passing the light through dispersive optics. This builds a hyperspectral image cube voxel by voxel. This can provide a high-resolution image but the acquisition speed is slow as the scanning process is extensive. Point scanning has been used in remote sensing, satellite imagery and confocal microscopy.

Line scanning (pushbroom) is an extension of point scanning where the FOV is scanned pixel line by pixel line. Spectral information is extracted the same way as point scanning, building the hyperspectral image line by line of voxels. The image quality

remains high and the acquisition time is reduced due to the larger area scanned. Line scanning has also been utilized in satellite imagery.

Spectral scanning (starring) is opposite from previous examples as it scans the entire FOV by detecting reflected or emitted light using band-pass spectral filtering. The image cube is built wavelength band by wavelength band. Image quality can range from low to high resolution depending on the FOV size and the spectral specificity of the scanning process. Likewise, the acquisition of the image cube is dependent on the same factors as point scanning of pixel area and bandwidths used.

Snapshot HSI captures an entire spectral image cube in a single scan. Snapshot scans the entire FOV and the acquired light is filtered through an array of prisms to map the image spatially and separate the image spectrally. This provides data in a single spectral image cube and can image multiple frames in a short period of time. While the spectral image acquisition time is short for snapshot HSI, the resolution can vary depending on the detector pixel count, dynamic range and how many separate bandwidths the spectral prisms delineate.

Both spectral scanning and snapshot HSI have been used for food analysis and document preservation. Recent work integrating HSI techniques into endoscopy have shown the potential of spectral scanning and snapshot spectral imaging to acquire video rate HSI images (four-dimensional snapshot) and classify tissue samples as normal and cancerous, as well as demonstrate potential utility for diagnosis and surgery guidance^{45,47,49}. These data highlight the same drawbacks of the current technology, achieving high resolution data and low acquisition speeds (~6 fps)⁴⁹ or trade a low resolution hyperspectral image to attain video rate speeds⁴⁵. Additionally, the majority of

studies thus far have been *ex vivo* for initial verification and technologies have not been translated to *in vivo* settings, which present additional limitations by miniaturizing components (i.e. the detector and the illumination source)^{47,49} and requirements for real time navigation. An optimal implementation of HSI technology would provide high resolution image data at video rate acquisition speeds on a scale that fits the domain of endoscopy. An additional aspect of HSI endoscope implementation is the data accumulated should be analyzed and presented to end users to visualize the contrast created by the HSI.

Spectral Data Analysis

Spectral images create a signature for every pixel providing enhanced contrast through spectroscopic differences (e.g., hemoglobin absorbs blue wavelengths creating a contrast to the surrounding mucosa) and spectral unmixing of biomarkers. Analyzing spectral image data needs to account for the size of the data (hypercube of X x Y x Z) and discriminating multiple components. Common spectral image analysis techniques include: subpixel abundance estimation, such as linear unmixing, dimensionality reduction techniques, such as principle component analysis and trained machine learning classifiers, such as support vector machines and neural networks.

Spectral unmixing estimates the abundance of individual components in a pixel (also known as sub-pixel analysis). This is accomplished by comparing a mixed pixel spectrum to a library of component spectra (endmembers) regressing the mixture spectrum to a combination of singular component spectra. Unmixing can be implemented using linear or nonlinear algorithms based on the composition of the pixel (linear:

separate components per pixel, nonlinear: component mixture per pixel). Linear unmixing has provided good separation for image data using several biomarkers^{50,51}.

Abundance classification is another version of spectral unmixing is a “macroscopic” pixel analysis to determine if the pixel is A or B (e.g., the spectrum of the pixel is analyzed as non-cancerous or cancerous). The unmixing process in these cases are not based on the component abundances (% of A, B and C) but how close the pixel spectrum matches the spectral library of A or B⁵²⁻⁵⁵.

Principle component analysis (PCA) is a statistical analysis that separates a component with the highest variance from the rest (principle component) and repeats with the next highest until all the components are separated. PCA is commonly used in studies to discriminate hyperspectral image data, especially in cancer studies^{43,46,55,56}. Another component analysis is independent component analysis (ICA), which separates components independent of their variance and dependent on user input prioritization⁵⁷. PCA variance separation has the potential to cause an error in the analysis when the variance is small. That is the justification for ICA to prioritize the analysis differently to avoid the low variance/high spectral resolution. However, the same study advised against ICA for separating many components (such as 100's to 1000's of spectral bands in remote sensing or several biomarkers) due to the user's bias in component weighting for separation. Despite the trade-offs, PCA is still widely used for spectral image analysis.

Support vector machine (SVM) is a machine learning model that trains and learns to classify data into two categories for a binary approach. Separation is determined by mapping the data into a higher dimensional space to find a new vector of separation that was not discernable in the original finite dimension. SVMs have been used more for

spectral separation of normal and cancerous tissue⁴⁶. However, there is potential to categorize multiple fluorescent markers using multi-class or hierarchical tree SVMs³⁴.

Neural networks are another machine learning model that replicates neurons in the human nervous system to break down data into branches and nodes respectively to determine the contents of the data. There are numerous designs and functions of neural networks depending on the needs of the analysis such as: perceptron, feed forward, recurrent and convolution. In the case of image and video data, convolution neural networks (CNN) are the models of choice⁵⁸⁻⁶². These methods separate the data into spatial and temporal aspects for analysis to track changes in video feed.

Systems Engineering Tools and Analyses

The previous sections highlight the need to evaluate alternative design approaches that could achieve the objective of this work. There are many avenues to explore but with limited time and resources there needs to be concise determination of the alternatives to maximize options useful for the objective. Therefore, creating system boundaries (black-box) for the endoscope and using systems engineering (SE) tools will benefit and accelerate the continued development of endoscopic technologies. Standard SE analyses include stakeholder inputs, and system use cases, requirements documentation (desires, functional, validation and verification) and system architecture (logical and physical). This section outlines other analyses and tools beyond the traditional SE toolbox which include the following topics: multi-objective trade-off analysis and changeability.

For a top-down systems engineering approach, decision-making is critical before any physical designing, prototyping or testing of a system is accomplished. This makes

realizing a system difficult without many of the physical or functional aspects. Decisions must satisfy customers or stakeholders in order to determine system characteristics and requirements. This high-level determination also aids in weighing possible design alternatives. A standard decision-making tool is the Pugh matrix for listing all the options and scoring them on how they meet certain criteria^{63,64}. Scoring, from a Pugh matrix, can aid in determining future endoscope systems. Considering system alternatives, trade-off analyses are critical for screening options on a multi-functional, multi-criteria system. Compromises begin at the stakeholder level to accommodate requirements and as many desires as possible. The challenges continue downstream for decisions on functionality or outputs of the various aspects of the system. Depending on system complexity, options could be as simple as choosing the best outcome out of two options or filtering through multiple alternatives⁶⁵. The latter has been studied using neural networks and Bayesian algorithms for multi-objective scenarios^{66,67}. As endoscopy becomes more complex and the process produces more data, trade-offs will result and approaches are needed to resolve or diminish these compromises.

Finally, another key to system improvements or modifications is changeability⁶⁸. This is an encompassing term for metrics such as flexibility, adaptability and modifiability. Endoscopy has evolved through multiple iterations and this work anticipates to provide another. Determining and quantifying the changeability of current endoscope systems will aid in future designs and integrations.

CHAPTER III: ENDOSCOPY LIFETIME SYSTEMS ARCHITECTURE: SCOPING OUT THE PAST TO DIAGNOSE THE FUTURE TECHNOLOGY

This manuscript develops the system architecture for the endoscope at key iterations throughout the system's lifetime. The "results" section determines trends in subsystem technology and provides concepts for the next-generation of endoscope. This manuscript has been peer reviewed and published in MDPI's Systems journal.

Browning, C.M., Cloutier, R., Rich, T.C., and Leavesley, S.J., "Endoscopy Lifetime Systems Architecture: Scoping Out the Past to Diagnose the Future Technology," Systems 10(5), (2022).

© 2022 by the authors. Licensee MDPI, Basel, Switzerland. This article is an open access article distributed under the terms and conditions of the Creative Commons Attribution (CC BY) license (<https://creativecommons.org/licenses/by/4.0/>).

Abstract

Systems engineering captures the desires and needs of the customer to conceptualize a system from the overall goal down to the small details prior to any physical development. While many systems projects tend to be large and complicated (i.e., cloud-based infrastructure, long-term space travel shuttles, missile defense systems), systems engineering can also be applied to smaller, complex systems. Here, the system of

interest is the endoscope, a standard biomedical screening device used in laparoscopic surgery, screening of upper and lower gastrointestinal tracts, and inspection of the upper airway. Often, endoscopic inspection is used to identify pre-cancerous and cancerous tissues, and hence, a requirement for endoscopic systems is the ability to provide images with high contrast between areas of normal tissue and neoplasia (early-stage abnormal tissue growth). For this manuscript, the endoscope was reviewed for all the technological advancements thus far to theorize what the next version of the system could be in order to provide improved detection capabilities. Endoscopic technology was decomposed into categories, using systems architecture and systems thinking, to visualize the improvements throughout the system's lifetime from the original to current state-of-the-art. Results from this review were used to identify trends in subsystems and components to estimate the theoretical performance maxima for different subsystems as well as areas for further development. The subsystem analysis indicated that future endoscope systems will focus on more complex imaging and higher computational requirements that will provide improved contrast in order to have higher accuracy in optical diagnoses of early, abnormal tissue growth.

Introduction

Systems engineering (SE) is a holistic engineering skillset and mindset structured to decompose large, complex systems down to nuts and bolts and ones and zeros prior to “breaking ground” on design and fabrication. The documentation produced from SE procedures is comparable to an instruction manual that traces those bolts and bytes into components, assays, and subsystems culminating to the final system. Simultaneously, the

“manual” provides parameters and verification metrics that should be met at every level of decomposition to ensure the end product’s output is productive, safe, and correct for all stakeholders involved. A note of importance in the SE process is that the documentation produced should maintain a level of abstraction to allow for creative, inventive, and cost-effective design when producing physical aspects of the system. For example, a future smart city system needs to dynamically transmit data to the populous of autonomous vehicles on the street at X Mb/s. The requirement does not dictate that it should be Bluetooth or 5G link; it could be a new method of data transfer.

Systems engineering also tracks a system throughout its lifecycle, from conception to retirement and disposal. For this manuscript, we coin a new term called “system lifetime”, which considers many different lifecycles of a system throughout history, in other words, many generations of development of a system. Noteworthy models for lifecycle processes are the waterfall and spiral model⁶⁹. These models are primarily used for software systems, but are also exemplary models for the iterative process of producing a physical system to meet the requirements set forth in the conceptual phase. These models have been beneficial to the structuring of this work considering the lifetime of a system. Considering the waterfall or spiral in a three-dimensional space with lengths of time between new waterfalls or spirals provided a unique concept to organize the many lifecycles of system development over the course of the system lifetime. Furthermore, Hossain and colleagues have recently detailed a review of systems thinking topics through a bibliometric analysis to highlight past trends and determine current gaps in knowledge of systems thinking⁷⁰, and we made use of some of the approaches presented in this review to analyze the development of endoscope

systems and potential future directions. While SE is beneficial for new, large, complicated systems such as smart cities, green energy infrastructure, and digital medical recording techniques, it can also be utilized to review and optimize smaller, complex, existing technology such as the endoscope.

Endoscopy is a medical screening process by which internal (normally hollow) organs are imaged by the insertion of a scope with illumination and imaging capabilities. Through visualization, clinicians can optically diagnose infection, inflammation, or lesion growth and resect portions of tissue for pathological diagnostics. There are four major endoscopic techniques widely used today: white light endoscopy (WLE), narrow-band imaging (NBI), Fujifilm flexible spectral imaging color enhancement (FICE), and virtual endoscopy (VE). WLE is the gold standard technique used for decades to capture a typical RGB (red–green–blue) image providing reflectance-based images of the luminal wall^{28,71,72}. NBI illuminates body cavities with blue and green light to harness the light absorption of the vasculature at these wavelengths providing additional contrast to the image^{21,73}. FICE is a post-acquisition process that divides the RGB image into the respective three colors and digitally alters wavelengths to enhance the contrast^{74,75}. VE uses coherent tomography scanning (CT scan) or magnetic resonance imaging (MRI) to render a 2D or 3D model of the hollow cavities traditionally imaged with an endoscope⁷⁶. These techniques are detailed further for their strengths and weaknesses in Section 3. Pathologies of the gastrointestinal (GI) tract can at times be difficult to differentiate from the surrounding mucosa^{11,22,28,77}. While current techniques provide several complementary modes for visualizing internal body cavities, the contrast and definition between healthy and afflicted tissue is limited, especially in early-stage cancer. The

limited contrast between some cancers and the surrounding mucosa can have downstream consequences on detection accuracy and patient outcomes, for example in colorectal cancer, which is the third-ranking cancer in the United States for incidence and mortality rates^{4-6,78}. Neoplasia (abnormal cellular growth) can be difficult to observe within the mucosal lining. If missed, neoplasia can become invasive and malignant (cancerous); in essence, we have let a cellular vehicle run a red light without getting ticketed. Tumor growth 1) can approximately double in volume annually^{18,79}, 2) the standard of care for interval routine endoscopic screenings is 5 years⁷². Further, 3) a missed colorectal tumor could approximate a minimum 32X volume increase (assuming a constant exponential growth rate) before being detected at a subsequent colonoscopy. Therefore, it is important to develop improved technologies that provide high contrast and the ability to visualize neoplasia or early-stage cancer when viewing the hollow organs endoscopically.

Here, we aimed to present a historical review of the origins and development of the endoscope similar to the approach described in Julius H. Comroe, Jr.'s Retrospectroscope⁸⁰. Comroe's work reviewed technologies that were created secondary to the original intent or a culmination of separate inventions. The objectives of this review are to: (1) highlight major milestones throughout the lifetime of the endoscopic system (in the following section), (2) track changes or improvements of different components or subsystems, and (3) theorize what future endoscope systems will involve based on the review and existing (potentially unrelated) technologies. To achieve these objectives, a review of the endoscope was performed, system-level requirements and architecture were constructed at predetermined milestones, system elements were observed throughout the review to acknowledge areas for future improvement, and a

Pugh matrix scoring method was constructed to assess potential technology improvement areas for future endoscopes. A unique aspect of this work is a first-of-its-kind system engineering analysis for the endoscope by deconstructing major aspects of the system using model-based systems engineering (MBSE). The review then allows for speculation of what the future of the technology will be using preliminary decision-making tools. SE diagrams and graphical representations of component upgrades (i.e., light source evolving from a candle to high-powered LEDs) were used to visualize the evolution of the endoscope system. The architecture was developed in a system modeling software (Astah) and for the brevity of the review section, key elements of the system in each milestone are condensed into a figure for respective subsections. This provided insight into which aspects of endoscopy have been fully optimized and which can still be enhanced. Areas of improvement lead to the final section theorizing the future directions of endoscope technologies. Endoscopy has been reviewed multiple times⁸¹⁻⁸⁵; however, this article combines the historical perspective with a SE structure. System architecture highlights the traceability of a component throughout the endoscopic system and throughout its lifetime in the system. The overall goal of this historical perspective is to provide a system-level understanding of the endoscope that will serve as the basis for developing the next generation of endoscopic technology for enhanced contrast of tissue components, especially neoplastic growth.

Historical Overview

The historical overview of the endoscopic system is sectioned into 5 milestones that marked significant leaps in functionality: origin, electricity and the light bulb, fiber

optics, imaging and video, and finally the current version(s). Several other achievements are noted within these milestones to provide a comprehensive history of the endoscope. At each milestone, the systems architecture is updated to reflect the major changes to the system.

The Origin Story

Philipp Bozzini, a German physician, is credited as inventing the first endoscope (the Lichtleiter – light conductor) in 1806^{86,87}. Bozzini's manuscript states that there was a desire to be able to visualize the internal hollow cavities and organs such as the bladder, rectum, and pharynx. Hence, by this period in time, medicine had developed sufficiently that physicians knew that optimal care and treatment could come from visualizing the internal organs of the body. Bozzini had defined requirements needed for the original endoscope and the resulting system was impressive because most of the metrics still apply today (Figure 1)^{86,88}.

In the design of the first endoscope, Bozzini implemented concepts that are still in use today (in a modern form). Illumination was held constant by placing the candle on a spring within the housing so that as the candle burned the spring would keep the flame in the same position. The Lichtleiter insertion tubing was designed to expand the naturally compressed hollow organs. Additionally, there were various-sized insertion attachments to minimize discomfort for the respective human orifices. The original endoscope only scratched the surface of visualizing the internal organs with the short depth of insertion and low illumination of the candle, but this was an amazing foundation system because

the main function and concepts have been applicable throughout this system's lifetime, even for the technology we know today.

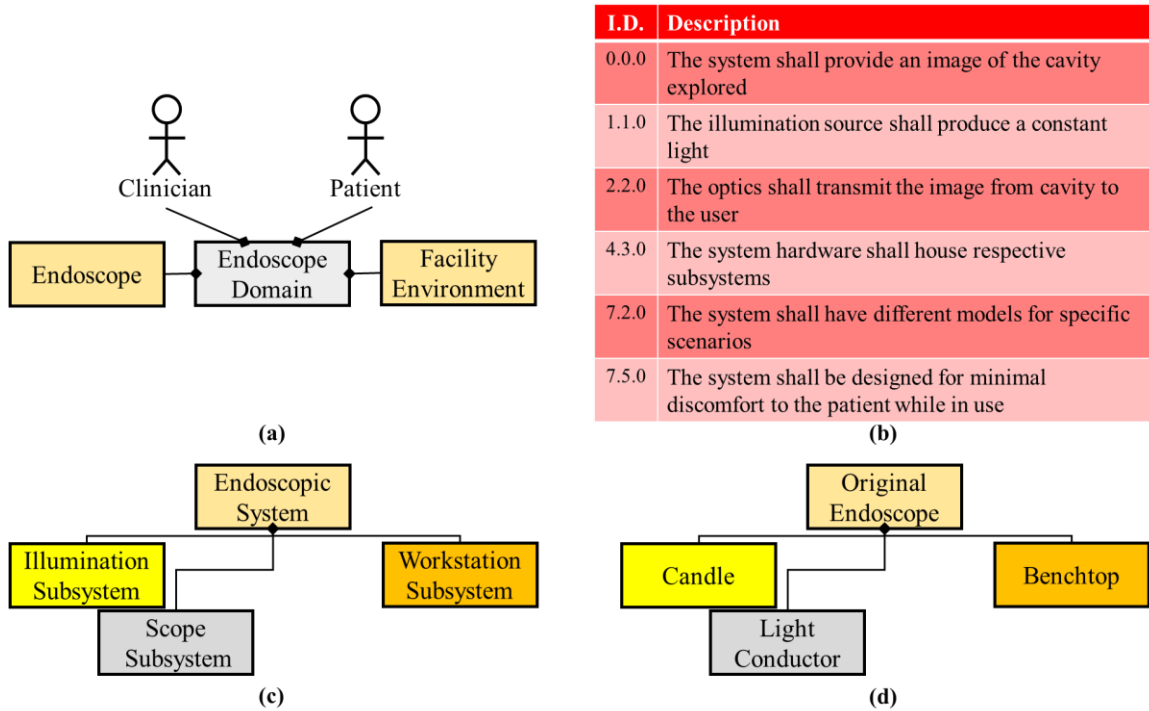


Figure 1. Condensed system architecture for the original (Lichtleiter) endoscope. (a) Domain diagram representing all actors and systems involved in the endoscopic domain. The original domain only concerned two actors (clinician/user and patient), the endoscope system and the environmental system. (b) A sub-selection of the requirements necessary for the original design extracted from Bozzini's documents which state some basic requirements that have carried through to the current version of the system. (c) Logical architecture of the system and a decomposition into subsystems. The system was broken down into 3 subsystems. (d) Physical architecture of the endoscope system highlighting major components within each subsystem (i.e., the candle and the light conducting hardware).

Antonin Desmoreaux improved the endoscopic system by replacing the candle with a gasogene (alcohol and turpentine) lamp for illumination (1853). He also coined the term endoscopy for the first time. This was the best and the brightest option for the time period; however, these light sources were only practical for illuminating internal tissues at short depths.

A Bright Idea

Illumination changed when society began to harness electricity via electric cells (Alessandro Volta, 1800)⁸⁹ and electric generators (Michael Faraday, 1831)⁹⁰. This spurred the invention of the light bulb and long-term electric lighting. Humphry Davy illuminated a charcoal strip wired to a battery, the first “light bulb” (1809)⁹¹. A platinum filament illuminated in a vacuum tube by Warren de la Rue (1840)⁹² presented an expensive, long-lasting light source. In 1867, Julius Bruck used this same technique in an endoscope system as the first hot illumination source (light source at the distal end of the scope)⁹³. Henry Woodward and Matthew Evans patented the light bulb in 1875⁹⁴. Joseph Swan enclosed the light bulb in a glass bulb (1878)^{95,96}. The original light bulb patent was bought by Thomas Edison (1879) and updated to the commercially available incandescent light bulb⁹⁷⁻⁹⁹. This technology was miniaturized and implemented into endoscopy by David Newman and Maximilian Nitze eight years later¹⁰⁰. This chain of events made the illumination source for endoscopy much brighter but the system architecture more straightforward (Figure 2).

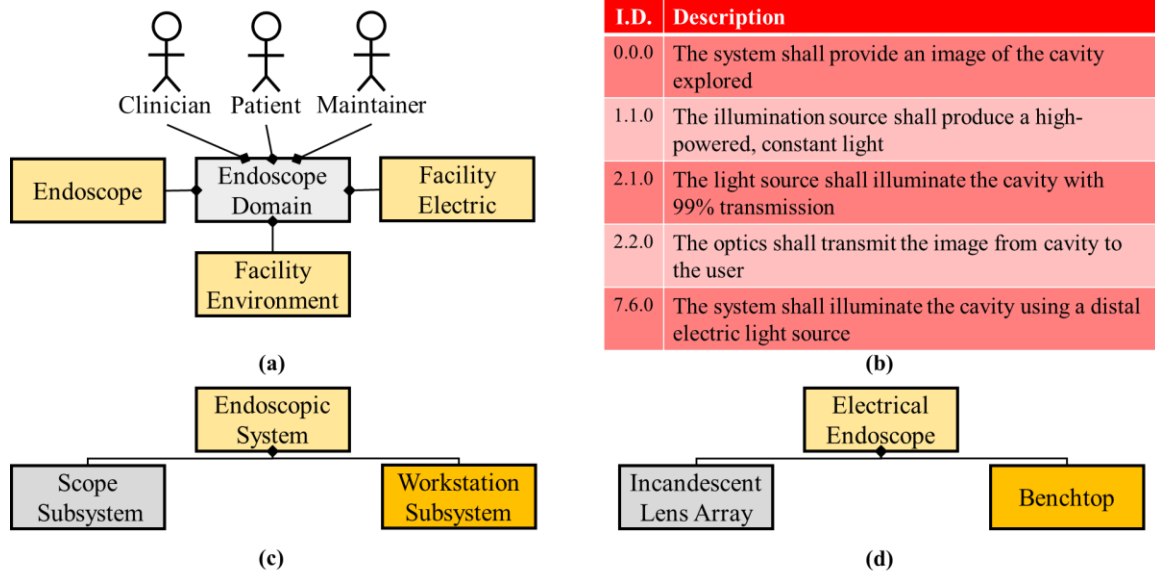


Figure 2. System architecture for the endoscope integrating the electric light bulb. (a) A maintainer actor has been added to the domain diagram due to a more complex system with components that degrade. The facility electric system was included in the domain as well due to the light bulb integration. (b) The requirements are updated in addition to the requirements presented in Figure 1b. (c) Logical architecture is peculiar in this generation of endoscopes because an illumination subsystem does not exist, and hot illumination (miniature light bulb on the distal tip) is within the scope subsystem. (d) Physical architecture included the light bulb (incandescent) and Nitze’s lens array.

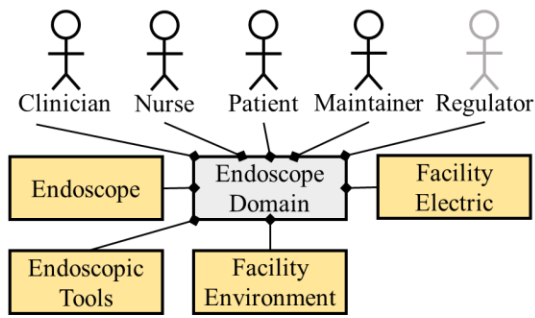
Ironically, the original requirements (Figure 1.B) still apply at this milestone although an electric light bulb has been added. Updated requirements were implemented due to the use of a “hot illumination” electric light source and accounting for illumination transmission through the system. Other updates to the endoscopic system during this time period included increased length of scope and advanced optics to transmit the image back to the user. Adolph Kussmaul visualized the upper GI with a 0.47 m long tube, a gas lamp (before the implementation of electric lighting), and the help of a sword-swallower in 1868 (the first esophagoscope)¹⁰¹. After the inclusion of filament lighting, Max Nitze implemented a lens array¹⁰² (design for telescopes) into a longer rigid endoscope to enhance the image (1879). However, the enhancements were nominal due to miniature

light bulbs that produced inadequate illumination and the large air gaps in Nitze's lens array.

“Savings” When You (Fiber) Bundle

From 1900 through to 1950, the advancement of endoscopic techniques was minimal—a proverbial dark age—until Harold Hopkins made several significant contributions to the fields of optics that would further endoscope capabilities^{103,104}. First, he created the zoom lens (1948) as a general optics assembly that would later be integral in endoscopy. In 1959, Hopkins created a rod-lens system that was an optical inversion of Nitze's lens array because Hopkin's design created “air lenses” from the small gaps between the glass rods. The rod-lens array was designed to minimize light loss via refraction, resulting in a ninefold increase in illumination transmission over Nitze's design. Additionally, seven years earlier (1952), Fourstier, Bladu, and Valmier made the light source of an endoscope external again (or cold illumination) due to the heat generated by distal (hot) illumination started by Bruck and Nitze⁸⁴. This was accomplished by transmitting light down a quartz rod in the rigid scope. At this point, if a photon were personified, it would run a relay race from the light source through optics to the internal organs, and then reflect back through separate optics, resulting in an image for the user. Due to longer light paths, it was imperative that transmission was at an all-time high. This is where Hopkins' third endoscopic achievement comes into play: the fiber bundle. Originally developed by Heinrich Lamm, the fiber bundle transmitted light from one end of these flexible silica fibers to the other^{82,84}. However, Lamm was ahead of his time because the fiber's utility was wasted until 1954 when Hopkins, with Narinder Kapany, applied the technique for illumination in endoscopy. They developed incoherent

(fiber orientation irrelevant) and coherent (fiber orientation accounted for) bundles to transmit illumination and the image, respectively. This was the era of the flexible endoscope. The orientation of the fibers and therefore the image matter because around this same time photography was becoming instrumental in the medical field. The architecture for this milestone is visualized in Figure 3. During this time period, the Food and Drug Administration (FDA) was created in 1906, marking the inclusion of regulatory oversight in biomedical equipment¹⁰⁵. In addition, within this century, nursing, nursing education, and the need for increased medically-trained staff were apparent¹⁰⁶. Hence, a regulator and nurse stakeholder are now considered in the endoscope system domain diagram (Figure 3a). Another notable development was the inclusion of air irrigation to expand (insufflate) a body cavity so as to obtain a larger field of view¹⁰⁷. Initially developed as a hand pump attachment (similar to a blood pressure cuff), this technique was later translated to a mechanical pump to provide automatic continuous insufflation. Therefore, a new subsystem (fluid) was added to the logical and physical architectures (Figure 3c, d, respectively).



| I.D. | Description |
|-------|---|
| 0.0.0 | The system shall provide an image of the cavity explored |
| 2.2.0 | The optics shall transmit (min. 90%) the image from cavity to the user |
| 3.0.0 | The fluids shall clear obstructions from field of view |
| 4.2.1 | The illumination shall couple to align with scope optics |
| 6.0.0 | The system shall have accessory tools to obtain more data beyond images |
| 7.6.0 | The system shall transmit light farther into the body |

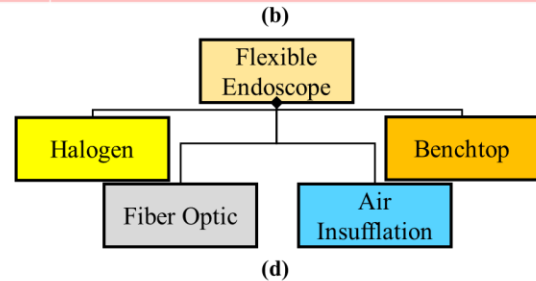
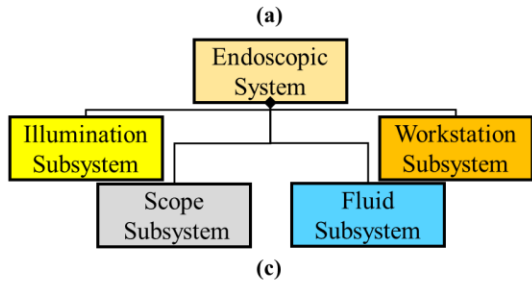


Figure 3. The endoscope milestone involving significant optical updates. (a) The domain diagram for the optical milestone includes the additional actors of the regulator (the FDA was established in 1906) and the nurse (nursing programs were commonplace by 1950), as compared to the domain diagram of the electrical milestone (Figure 2a). The regulator is a passive stakeholder denoted by increased transparency. Around this time endoscopic tools were introduced during procedures and are indicated in the domain diagram as a secondary system. (b) A summary of the requirements for this milestone. These requirements are updated or in addition to the requirements presented in Figure 1b and Figure 2b. (c) The illumination and the fluid subsystem were added to the logical diagram due to cold illumination and insufflation. (d) Physical components of the system include halogen bulbs, the fiber optic bundle, and air insufflation.

Smile, You're on Camera

The first endoscopic image was acquired by Nepomuk Czermak in 1860, of his own larynx¹⁰⁸. Theodor Stein developed cameras that were lighter and smaller in 1873 for imaging the larynx. Max Nitze created the first endocamera in 1894, among his other notable endoscopic achievements. Paper film was produced in 1885 and celluloid in 1888 by George Eastman¹⁰⁹. Color photography was theorized by James Maxwell (1861)¹¹⁰, commercialized (with limited practicality) by Frederic Ives (1890)¹¹¹ and John Joly (1894)¹¹², and prized by Gabriel Lippmann (1908)¹¹³. Gastroenterologist N. Henning reported the first color endoscopic photograph in 1938⁸¹. Photographic documentation for

endoscopy became the status quo in 1954 marking a milestone in the screening process of endoscopy¹⁰⁸.

Early moving pictures notably began with devices such as the Praxinoscope and Phènakiscope in the 19th century¹¹⁴. Thomas Edison and William Dickson made another noteworthy contributions with the invention of the Kinètographe camera that filmed a video on a film reel (1891)¹¹⁵. The Lumière brothers (Auguste and Louis) popularized video documentation in 1895 with the Cinématographe, the first camera projector, and hosted the first public film¹¹⁶. Auguste Lumière acquired the first medical film that same year of a military doctor treating three patients in the barracks. However, video film was not used in endoscopic procedures until the 1950's, with the first televised bronchoscopy and recorded laparoscopy¹¹⁷.

Imaging and video acquisition was further advanced in 1969 with the invention of the charged coupled device (CCD) from Boyle and Smith at AT&T Bell Labs (additionally the complementary metal oxide semiconductor – CMOS from NASA in 1992)^{118,119}. The CCD, originally developed for solid state data transfer, became a noteworthy component for digital photography. Integrated circuitry continued to improve (Moore's Law) creating smaller pixels, more densely packed pixel areas, and therefore smaller image sensors¹²⁰⁻¹²³. The resulting component was small, cheap to produce, with low power consumption, and continually upgraded image quality. Interestingly, the combination of the camera phone in 2000¹²⁴ and the exponential popularity of Apple's iPhones (beginning in 2007)¹²⁵ created the driving factor for image sensor improvements and manufacturing. While the chip-on-tip image sensor was implemented for laparoscopic surgery in the 1980s¹²⁶, the image improvements for endoscopy can be

correlated to the desire to improve image quality in cellular devices. Digital imaging for endoscopy, specifically laparoscopy, improved visualizing body cavities, optical diagnoses and surgical procedures. As compared to standard open surgical techniques, laparoscopic surgery allowed for smaller incisions, reduced recovery times, and improved patient outcomes, especially for common procedures such as hernia repair, gallbladder removal, and appendectomy. The system architecture overview for the imaging milestone is shown in Figure 4.

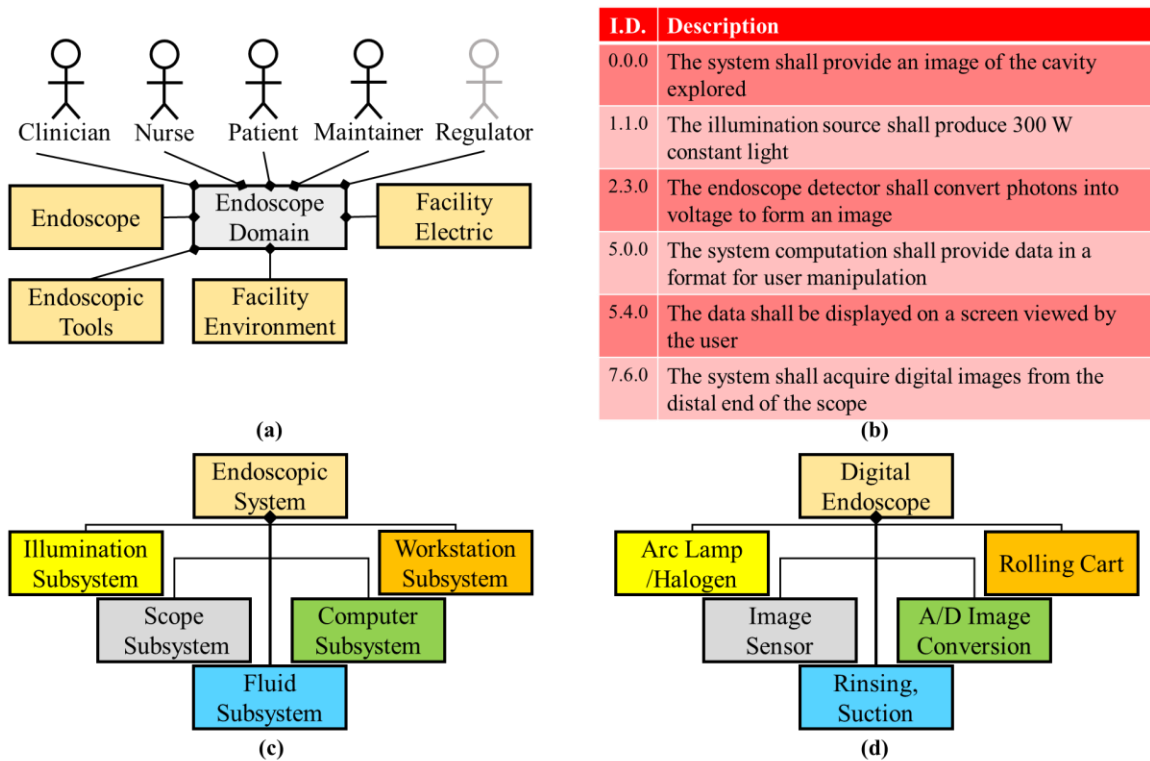


Figure 4. Digital imaging endoscope system architecture. (a) The domain diagram remains the same for this milestone when compared to the domain of Figure 3a. (b) The requirements assessment reflects the high-powered light sources of this era and digital imaging. (c) A computer subsystem was added to the logical diagram of the previous milestone (Figure 3c) due to digital imaging. (d) Arc lamps, CCD cameras, rinsing, and digital imaging conversion are physical component examples of this architecture.

Presenting, the Endoscope

Current state-of-the-art endoscope systems utilize a combination of broadband light sources (xenon arc lamps, halogens, or LEDs), bandwidth filtering, and digital analyses to produce WLE (gold standard), NBI, or FICE. One limitation of WLE is that small and subtle changes within the lumen may not generate sufficient contrast to be detected. In addition, abnormal, irritated, inflamed, or neoplastic tissue may appear very similar to normal tissue, resulting in difficulty determining potential areas of risk, especially for patients with underlying inflammatory conditions. To improve detection sensitivity and specificity, a range of correlating factors are often considered, such as: irregular mucosal patterns, condensed vasculature, and definitive redness. Introduced briefly before, NBI and FICE are two complementary modalities to WLE that can provide enhanced contrast of tissue structures between mucosa and lesions. NBI filters utilize narrow spectral bands in the blue and green regions to illuminate the tissue, harnessing the absorption of blood at those wavelengths and creating an image that contrasts vasculature as brown²¹. Condensed vasculature has been associated with lesional tissue due to its invasive, nutrient-draining nature. FICE is an image algorithm that uses the RGB image acquired through normal screenings and processes individual color channels into unique wavelengths (within the respective color range) that accentuates tissue differences greater than the original colored image⁷⁴. This method has defined mucosal irregularities and tissue irritation more effectively than traditional WLE due to post-imaging processing. These techniques are included in aspects of the current architecture (Figure 5).

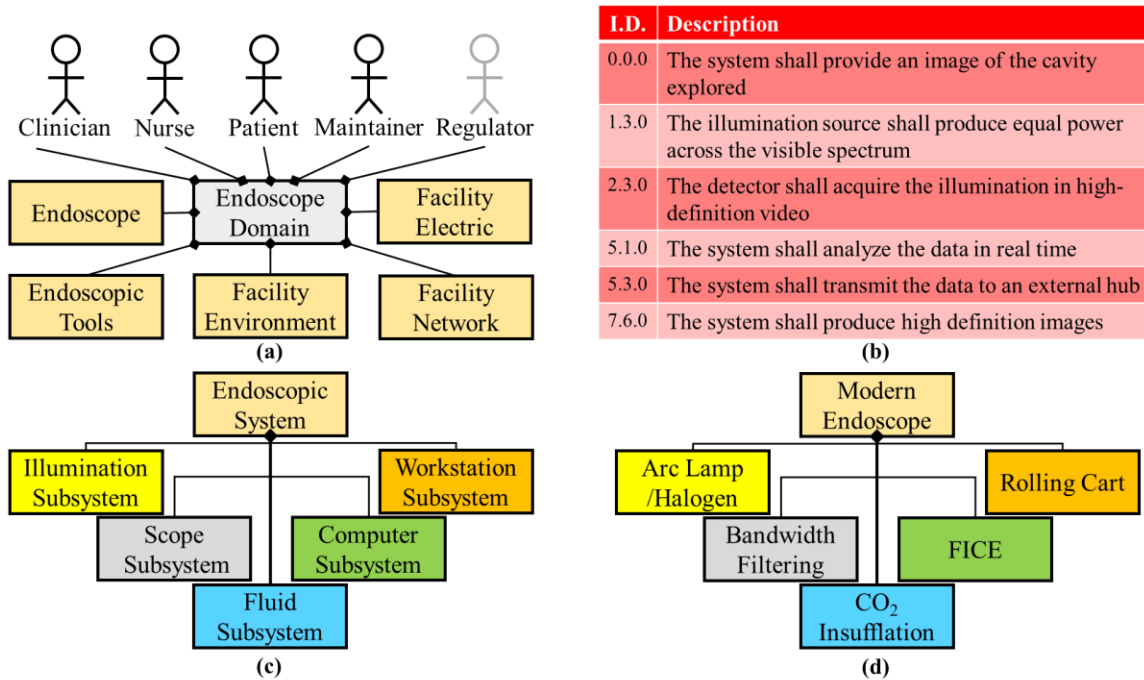


Figure 5. Current endoscope condensed system architecture. (a) The facility network external system was added to the domain diagram of the current system, compared to that of the imaging milestone domain (Figure 4a), because of the use of the internet and cloud storage. (b) High-definition and spectral aspects are stated in the requirements for the current system. (c) The logical diagram remains the same as the previous milestone (Figure 4c). (d) Physical components and software are bandwidth filters and FICE software for this architecture milestone.

Another modern endoscopic screening technique is virtual endoscopy (VE) or computed tomography (CT) endoscopy^{76,127}. Using CT creates a volumetric image of the entire colon or tracheobronchial tree with a noninvasive technique. VE is a beneficial screening for patients with occlusions prohibiting traditional WLE, providing a complete image of the respective body cavity and the best option for older patients or patients who are contraindicated from standard endoscopic procedures. CT data provides cross-sectional views of the organs and 3-dimensional reconstruction to create a virtual scan that resembles a WLE procedure.

Another alternative to WLE is capsule endoscopy^{128,129}. Capsule endoscopy is more invasive than VE, but still requires less hospital procedure time than standard WLE colonoscopy. An endoscopic camera and illumination source in capsule form is ingested and transmits video feed to wearable receiver for clinicians to view post ingestion. Current models are intuitive to their location in the gastrointestinal tract with automated data acquisition rates depending on the rate of capsule movement (data acquisition would decrease in the stomach and if the capsule slowed or stopped) and have two wide angle cameras to ensure full view of the colon. The fact that the capsule primarily images the small and large intestines highlight that capsule endoscopy is currently utilized primarily for colonoscopy imaging and the optimal scenario to image or view the small intestine.

Modern endoscopic techniques are a definite advancement from Bozzini's original endoscope. Current state-of-the-art endoscopes are focused on contrasting and detecting minute tissue changes to diagnose early, screening processes that are minimally invasive, and providing as much information (the "big picture") to benefit the patient. In the previous section, the history of the endoscope was detailed and the system upgrades were traced. Next, individual subsystems of the endoscope system were analyzed to view the trends through the endoscope lifetime and discuss where components or subsystems are currently optimal and can be improved or upgraded.

What's Trending

Systematic decomposition of previous and existing endoscopic systems highlights the improvements of subsystems and elements within the system, as well as areas for potential upgrades. Here, the current milestone logical architecture is highlighted and the

trends in technology are shown for particular subsystems (Figure 6). A primary advancement is the illumination source from candles to incandescent bulbs to LEDs (Figure 6a). Light sources have shown a substantial improvement in luminosity, decreased power consumption, and increased component longevity. Some literature theorizes that illumination technology is reaching maximum potential in white light luminous efficacy¹³⁰.

With regard to the computational subsystem, we examined the trend in the literature of endoscope-related computer science publications. We searched the Scopus database for publications in the field of computer science using the keywords “gastroenterology” or “endoscopy” and a date range of 1990–2019, divided into five-year increments (Figure 6b). Results indicated that the last two decades have shown a 50X increase in the number of publications fitting these parameters. Examples of the increased computational demand of such components begin with the image sensor digital signal processor (DSP) to convert photons to digital signals¹³¹ and expand to three-dimensional (VE and optical coherence tomography—OCT)¹³² and wireless or self-contained (capsule endoscopy) or enhanced channel contrast (FICE).

The optical light path which carries illumination to the patient cavity and the image back to the user or imager has also been optimized through the years (Figure 6c). The Lichtleiter with a length of ~10 cm increased to the current colonoscopes with a length over 1.5 m, capable of spanning the entire large intestine and a portion of the small intestine. These depths would not be possible if fiber optics were not introduced, creating flexible endoscopes. Furthermore, a smaller fiber optic bundle and overall endoscopic diameter allowed for the development of smaller systems such as bronchoscopes,

cystoscopes, laparoscopes, and ureteroscopes for lungs, bladder, small surgical openings, and ureter, respectively¹³³. Flexible endoscopy has not extended the working length further into the small intestine due to the tortuous and compact nature of the organ¹³⁴. Maneuvering a flexible scope through the small intestine could perforate the mucosal lining or damage the fiber optics of the endoscope. Furthermore, the amount of articulation and force that could be applied to the endoscope tip decreases with increased length and depth into the lower GI. Smaller endoscopes are limited in illumination and detection due to size constraints. Therefore, the output of these smaller systems has lower spatial resolution and potentially lower contrast between normal and abnormal tissue.

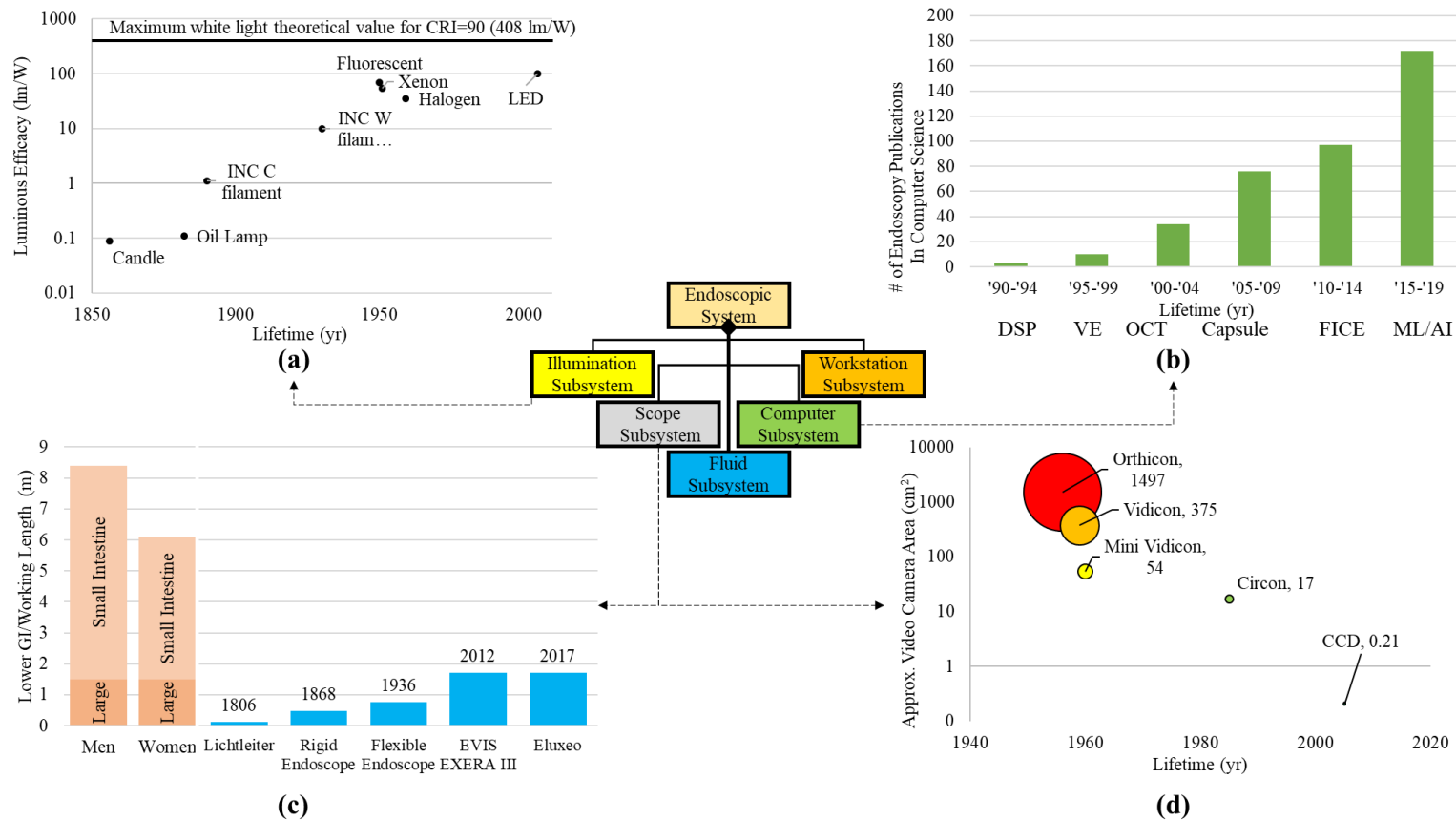


Figure 6. Trends for components within subsystems. **(a)** Light sources in the illumination subsystem presenting the luminous efficacy from the candle to arc lamps and LEDs. Illumination data were extracted from Azevedo et al.'s paper on solid state lighting¹³⁰. **(b)** Advancements in computational aspects of endoscope systems were visualized by plotting the increase in endoscope-related publications within the computer science field (publication search for “endoscopy” in the computer science category per quinquennium—Source: <http://www.scopus.com>, accessed on 28 July 2022)¹³⁵. Some examples of imaging processing technologies that were found include: digital signal processing (DSP), virtual endoscopy (VE), optical coherence tomography (OCT), capsule endoscopy (Capsule), Fujinon's flexible spectral imaging color enhancement (FICE), and machine learning (ML)¹³⁶. **(c)** Optical pathway (working length)^{82,88,101} for the scope subsystem showing the depth the endoscope has traversed throughout the milestones compared to the length of human body intestinal tract¹³⁷. **(d)** Approximate camera/detector area for various cameras (both film and digital) throughout imaging in endoscopy. Camera and detector areas were assumed from dimensions given in literature^{82,117,138–140}.

Creating physical records of endoscopic screenings is one of the most important aspects of the field today. The transition from clinician hand-drawn images to film photography lessened the workload and provided an objective image to support diagnosis. Ironically, cameras continued to improve by creating clearer pictures while becoming smaller components within the system (Figure 6d). Film-based cameras were large additions to system on the proximal end. Now, digital image sensors are miniaturized on the distal end of scopes providing real-time, high-definition images and video.

Endoscopy: The Next Generation

Using systems engineering architecture as a tool for review, we can exhaustively survey the needs of the range of subsystems and components, as well as environmental constraints and current technologies. We can predict which technologies may need to evolve and what a next generation endoscope would provide. Based on Figure 6, illumination is at a current maximum, digital sensors can accommodate any endoscope diameter with the caveat of limited resolution for smaller sensor sizes, the working length of the scope cannot get any longer due to highly condensed and tortuous nature of the small intestine and there is a high interest in the computational capabilities of the endoscopic technologies. Reviewing past inventions that were implemented into endoscopy, Figure 7 shows the importance of looking at off-the-shelf components and technology.

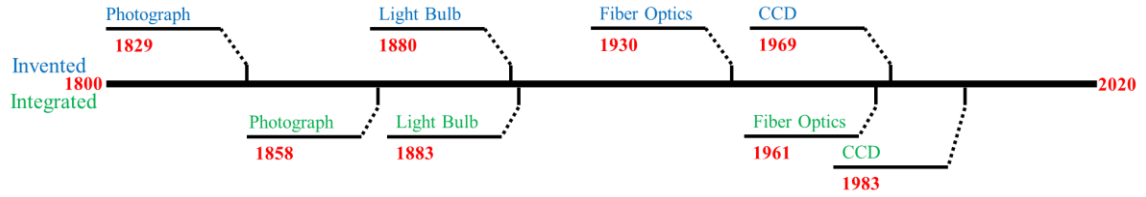


Figure 7. Timeline comparing technology invention dates to the time it was integrated into endoscopy. Blue text denotes invention and green for integration.

The endoscopic community was quick (3 years) to integrate incandescent light bulbs to the endoscope design, but it was over 30 years between invention and implementation of the fiber optics, creating the flexible endoscope. Therefore, a technology might already exist with the potential to benefit the output of endoscopy. For the scope of this manuscript, we reference the previous upgrades and potential gaps in the system while acknowledging the technologies that exist outside the field of endoscopy. To begin justification for these possible upgrades, a mind map was constructed to outline the avenues (Figure 8).

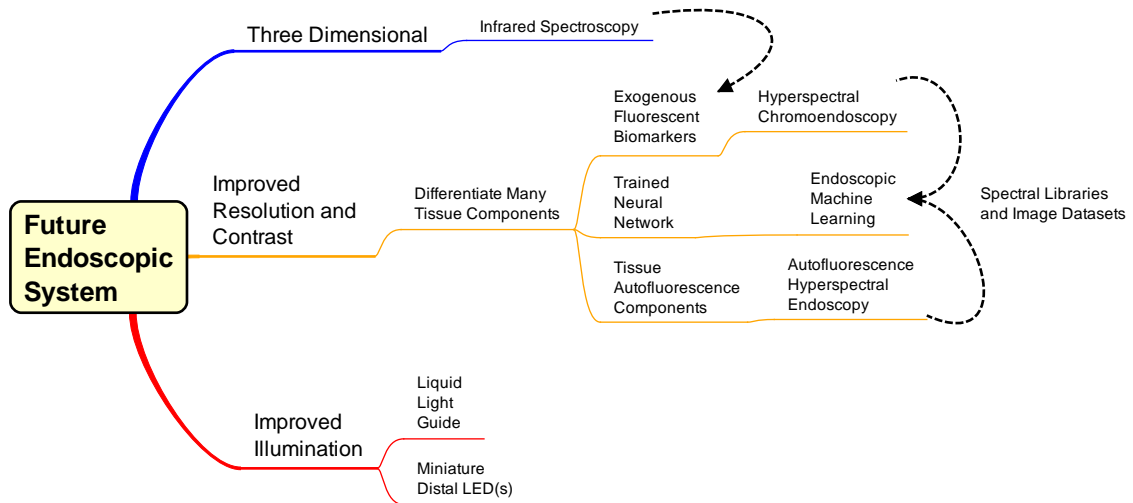


Figure 8. Mind map for design of a next-generation endoscopic system. The middle and top pathways are considerations of techniques to implement, and the bottom pathway is component upgrades of the current endoscope system. Dashed lines convey interconnectivity between topics: Infrared analysis could implement with exogenous fluorescent biomarkers and hyperspectral chromoendoscopy and autofluorescence hyperspectral endoscopy could be analyzed and displayed via machine learning algorithms.

The mind map has two parts: technology for implementation (top two pathways) and components to improve current systems (bottom pathway). Components for increased illumination throughput include miniature LEDs at the distal end of the scope and/or a liquid light guide instead of fiber bundles. When digital camera sensors became small enough, they were integrated at the distal end of endoscopes, reducing transmission losses by eliminating the secondary (imaging) light guide. If white light LEDs or three respective RGB LEDs were small enough to replace the illumination fiber optic area of the distal tip, then transmission losses would be further reduced. A major factor in creating a new hot illumination is the potential for heat dissipation and mitigating damage to the patient cavity. Another option is exchanging illumination fiber bundles for liquid light guides (LLG) to increase the throughput of the endoscope. An LLG has no void fraction, a higher numerical aperture, and a higher acceptance angle compared to fiber

optic bundles accepting more illumination proximally, minimal internal refraction, and a diffuse illumination at the distal end (potentially illuminating a larger area). A limitation to using LLGs would be a slightly smaller spectral transmission range (normally 200–600 or 400–2000 nm) than that of a fiber optic bundle with broader transmittance (200–2000 nm).

Another option is infrared spectroscopy for additional information to WLE. Infrared wavelengths are longer and penetrate deeper than visible wavelengths. Therefore, there is potential for image information within deeper layers of tissue beyond the mucosa. A benefit of extended optical penetration depth could be identifying density variations in the tissue beyond the mucosal wall^{141–143}. Similar to the vasculature, higher density could correlate to lesion growth, and this could enable early detection. Infrared illumination and imaging also has the potential to discriminate neoplasia from inflammation¹⁴⁴. The limitation here is the need for a separate detector and illumination to outfit the infrared technology necessary to produce visible images for the user.

The mind map topics which combine new and old technologies to enhance contrast the images produced are detailed below. Here, they are labeled as: endoscopic machine learning, autofluorescence hyperspectral endoscopy, and hyperspectral chromoendoscopy. Machine learning has become an integral part of many fields, especially in applications that produce large datasets. Machine learning (ML), if implemented on a computational platform capable of real-time operation, could provide automated cues to clinicians that would aid in identifying potential abnormalities. ML outputs could be false-colored or overlaid in some other form with traditional WLE, NBI, AFI, or CE image data such that the cues are visible during a standard endoscopic

technique. The requirements for ML in endoscopy need to focus on computation functioning in real-time. Hence, computational capabilities would have to be sufficiently developed to allow real-time classification and false coloring or superposition of classification results with traditional endoscopic procedures in order for this approach to be viable.

The specificity of AFI endoscopy techniques could be improved through enhanced contrast created by several endogenous fluorophores (native autofluorescence) in human tissue¹⁴⁵⁻¹⁴⁷. An optimal way to excite these autofluorescent biomarkers is hyperspectral imaging (particularly spectral scanning). Hyperspectral imaging generates complex image data, hypercubes, in which two dimensions represent spatial data and the third dimension represents spectroscopic data. Spectral hypercubes can be analyzed to estimate the contributions of different molecules, such as autofluorescent molecules, and these signatures can be false-colored and overlaid to generate added contrast in endoscopy images. However, autofluorescence is an inherently low signal, so the spectral illumination has to be powerful enough to provide sufficient excitation and emission signals for the detector. Current autofluorescence imaging in endoscopy typically highlights one or two endogenous molecules with one or two excitation sources^{29,148-151}. Minimal excitation sources allow for longer acquisition and higher signal while maintaining video rates. For hyperspectral autofluorescence imaging of 5 or more endogenous molecules (assuming notable unique molecular and spectral contributions), shorter acquisition is required for the video rate, lowering the excitation signal. However, the excitation overlap could compound the excitation signal for each fluorescent biomarker. Most hyperspectral setups of this nature come with a trade-off between spatial

resolution, acquisition rates, and spectral sampling. We would expect that future endoscopic system will mitigate this trade-off in order to maintain the requirements of high definition and video rate imaging, while providing hyperspectral imaging capabilities.

The requirements discussed above for autofluorescence hyperspectral endoscopy would also apply for hyperspectral chromoendoscopy to be a viable addition to the endoscopic system. In this case, exogenous fluorophores (fluorescent dyes and stains) could be used to identify certain components, tissue types, or proteins, creating a list of biomarkers to image. This fluorescence mixture could be administered during bowel preparation or during the procedure, as is performed in traditional chromoendoscopy. Hyperspectral imaging, as described above, could then be performed to allow the identification of each of the many fluorescent labels. An additional benefit to exogenous fluorophores is that they produce greater emission signaling than autofluorescence. There are also exogenous fluorophores in the near-infrared range to expand components stained and increase the contrast^{152,153}. Importantly, both of these hyperspectral techniques can provide new or complimentary data for machine learning scenarios to automatically identify and flag suspicious regions for further investigation.

To understand the potential technologies that could be incorporated into a next-generation endoscope, a Pugh matrix (Table 1) was constructed. The Pugh matrix is a system engineering tool that can be used to evaluate the importance and potential impact of each endoscope technology when considering a range of parameters. Modern endoscopic procedures are included as well for reference. Scoring parameters for the Pugh matrix were determined by first considering the patient (safety, invasiveness, and

comfort), then prioritizing clinician training and technology implementation (i.e., operational training and implementation cost), and finally considering the additional image data and information that could be produced (new image data and contrast). Scoring (described below) was conducted by a panel of six gastroenterologists from the University of South Alabama Division of Gastroenterology. Each category (column) within the technology row was averaged among the $n = 6$ responses and the standard deviation was calculated. The matrix did not include any weighted metrics and was primarily used to compare new or potential technologies to the gold standard of WLE (labeled as Current Endoscopy) and to consider which technology could represent a future next-generation endoscope. The metrics were graded as follows: Safety—How safe would this procedure be? 5 = most, 1 = least. Invasive—How invasive would this procedure be? 5 = highly, 1 = minimally. Patient Comfort 5 = comfort, 1 = discomfort. Operational Training—How much operational training would be required? 5 = extensive, 1 = minimal. Example Image Training—How much training with example images is needed? 5 = extensive, 1 = minimal. Implementation—How easy would the technology be implemented? 5 = challenging, 1 = easy. Cost to Implement—How much would this technology cost to integrate? High = \$\$\$ = 5, Low = \$ = 1. Additional Image Data—How much additional image information would be produced? 5 = substantial, 1 = minimal. High Contrast—Would this technique produce a higher contrast than WLE? 5 = substantial, 1 = minimal. The final column of the matrix totals the scores for comparison (the values are in bold to highlight the overall results of the table). For this work, Invasive, Operational Training, Training Image Data, Implementation, and Cost were all subtracted from four, so the total was the summation of the positive connotations for each

technology (i.e., the “inverse” of the aforementioned metrics were considered for the total—Invasive: five translated to a one for noninvasive).

The results of this Pugh matrix, based on the criteria selected, show that any new version of the system comes with some drawbacks, mainly the time to make operational (i.e., clinical trials, FDA approval, clinical acceptance). The technological trend of the future is big data and with that comes the bottleneck of analyses and results selection that are useful for the end product. All options were comparable in safety measures and patient comfort as physical procedures remain similar to WLE. Additional training requirements were anticipated with more advanced image data and analysis technologies (i.e., hyperspectral options). However, operational training should be comparable to WLE with the exception of some software interface changes. Interestingly, the (hardware and/or software) implementation of these technologies should be a streamlined process. These alternatives do not require redesigns, but component or subsystem exchanges that should minimize design costs and fabrication challenges. The cost of implementation would be high due to training (both user training and training data) and changing subsystems (i.e., illumination and scope subsystems). Current endoscopic systems scored the highest according to the matrix, but the long-term potential and in-depth data (Additional Data column of Table 1) provided by the alternatives make the initial drawbacks or cost worth the transition. The trade-off is noticeable when comparing the hyperspectral options to WLE. The hyperspectral technologies would need advanced training (especially example imagery for users and training data for neural networks, if applicable) but are anticipated to provide increased information and increased contrast for identifying suspect lesions (as seen in the Additional Data and Contrast columns).

Integrating a neural network or artificial intelligence into endoscopy also has a trade-off, as the additional information or contrast is also accompanied by a more complex data type that the clinician may have to interpret, if not sufficiently processed and summarized. Infrared imaging scored the lowest on the matrix due to the unknown factors of how the technology would integrate with an endoscope platform and how best to present the data to clinicians. Infrared imaging would require the most design-intensive change to implement a widefield technique infrared imager at the distal end of an endoscope. Regardless, the next generation of endoscopy will likely involve some aspect of machine learning and a technological advancement to improve contrast between normal and lesional tissue. Future system architectures will probably see a large increase in complexity for computing and illumination subsystems.

Table 1. Pugh matrix ranking alternative technologies compared to the gold standard (WLE). Metrics for scoring include safety, training, implementation, and added information. The scores are totaled for comparison.

| | Safety | Invasive | Patient Comfort | Operational Training | Example Image Training | Implementation * | Cost to Implement | Additional Image Data | Higher Contrast | Total |
|--|-----------|-----------|-----------------|----------------------|------------------------|------------------|-------------------|-----------------------|-----------------|-------------|
| Current Endoscopy | 4.3 ± 0.7 | 3.0 ± 1.6 | 4.0 ± 1.2 | 4.2 ± 0.7 | 3.7 ± 0.7 | 3.3 ± 1.4 | 2.8 ± 1.5 | 3.5 ± 1.4 | 3.0 ± 1.3 | 17.8 |
| Virtual Endoscopy | 4.7 ± 0.5 | 2.5 ± 1.5 | 4.5 ± 0.5 | 4.0 ± 0.8 | 4.2 ± 0.7 | 3.5 ± 0.8 | 3.5 ± 1.4 | 3.3 ± 1.1 | 3.0 ± 1.5 | 17.8 |
| Capsule Endoscopy | 4.2 ± 0.7 | 2.8 ± 1.2 | 4.0 ± 0.6 | 3.8 ± 0.7 | 4.2 ± 0.7 | 3.2 ± 1.3 | 3.5 ± 0.8 | 3.3 ± 1.1 | 2.8 ± 1.3 | 16.8 |
| Infrared Imaging Endoscopy | 3.7 ± 0.9 | 3.3 ± 1.2 | 4.0 ± 0.8 | 4.2 ± 0.4 | 4.2 ± 0.7 | 4.0 ± 0.8 | 3.8 ± 0.7 | 3.8 ± 0.7 | 3.2 ± 1.2 | 15.2 |
| Autofluorescence Hyperspectral Endoscopy | 4.0 ± 0.8 | 3.3 ± 1.2 | 4.0 ± 0.8 | 4.3 ± 0.7 | 4.7 ± 0.5 | 4.5 ± 0.8 | 3.7 ± 1.5 | 4.2 ± 0.9 | 4.0 ± 1.4 | 15.7 |
| Hyperspectral Chromoendoscopy | 3.8 ± 0.7 | 3.3 ± 1.2 | 4.2 ± 0.9 | 4.5 ± 0.8 | 4.7 ± 0.5 | 4.3 ± 0.7 | 3.8 ± 1.5 | 4.5 ± 0.8 | 4.3 ± 1.1 | 16.2 |
| Neural Network Endoscopy | 4.2 ± 0.9 | 3.5 ± 1.4 | 4.3 ± 0.9 | 4.7 ± 0.5 | 4.2 ± 0.9 | 4.2 ± 1.1 | 3.7 ± 1.9 | 4.2 ± 1.2 | 4.2 ± 1.2 | 16.7 |

Scoring: 5 = highly, most likely or effectively, 1 = minimally, least likely or effectively, * 5 = challenging, 1 = easy.

Conclusion

The aim of this work was to provide a historical review of the endoscope system using MBSE architecture. To our knowledge, observing the endoscope throughout the many lifecycles of development (which we defined here as the “system lifetime”) is a first-of-its-kind review for both the endoscope community and the MBSE community. From the review, the trends and changes to the technology were traced to determine where future iterations of the system are trending. This work contained three main objectives. The first objective was to present key milestones of the endoscope through systems architecture. The review indicated the systems architecture at each milestone and provided system traceability to track the changes throughout the system’s lifetime. The second objective was to track the changes and trends in components and subsystems of endoscopy. The traceability of the first objective highlighted the key components for which trends in development could be quantified resulting in a visualization of improvements over the system lifetime and areas for further research. The third objective was to theorize future technologies for endoscopy. The results indicate that complex and/or computationally-focused image technologies are important areas for the development of future endoscope systems. The history of the endoscopic system has a fascinating timeline from Bozzini’s brilliant inception, to sword-swallower patients, to the integration of several improved illumination and camera technologies over the last 50 years. Endoscopy provides numerous ways the clinician can screen the internal tissues benefitting patient care. This field also revolutionized the way surgeries are conducted and how medical data are produced via imagery. The system architecture produced here

has been an invaluable perspective for tracking the changes and additions throughout the last 200 years, as well as highlighting areas with potential for further optimization.

The future of endoscopy will require new imaging techniques that provide increased information and contrast. Based on this review, we predict that imaging will become more complex, or the endoscope system will provide opportunities to combine complementary imaging techniques so as to produce data that provide increased contrast and accuracy of optical diagnoses. Additionally, we anticipate that there will be an increase in computational requirements to accommodate more advanced imaging techniques. One primary computing requirement will be increased in silico computing capabilities to analyze image data in real-time. It is also important to consider that implementing new technologies will come with trade-offs, including the need for higher computing power, more training, or more complex devices. However, the increase in data to provide increased contrast and detection accuracy will outweigh the aforementioned trade-offs. Whatever the future of endoscopy presents, these trade-offs will be worth it long-term to provide superior care for the patient, more knowledge of the human body, and properties/attributes of disease progression.

Standard systems engineering analysis excels when the voice of the customer is involved and the use cases and requirements are defined. However, the historical aspect of this work makes involving past customers and users impossible. The requirements and use cases presented here are a mixture of literature and decomposition from the current system. We strived to keep the architecture unbiased, but we know that with assumptions there comes some bias elements. This is also true for the speculation of future endoscopic systems. For the scope of this work, we are providing our perspective based on

knowledge of the current system and similar technologies. The hope is that this architecture created can be used as a foundation for others in the fields (both endoscopy or biomedical imaging and systems engineering) to glean new ideas and find additional trends to bolster the next generation system even more. Similar to sensational skyscrapers, the future endoscopic system will need a great set of blueprints (architecture) and inputs from people (customers) in several fields and clinical settings. The goal of endoscopy remains the same, to provide an image of the cavity explored (to benefit the patient's long-term health). Hopefully, exploring the past endoscopes will establish new endoscopes with higher quality, more in-depth images.

Author Contributions

Conceptualization, C.M.B.; software, C.M.B.; investigation, C.M.B.; data curation, C.M.B.; writing—original draft preparation, C.M.B.; writing—review and editing, C.M.B., R.C., T.C.R., and S.J.L.; visualization, C.M.B.; supervision, S.J.L. All authors have read and agreed to the published version of the manuscript.

Funding

The authors would like to acknowledge support from the NASA/Alabama Space Grant Consortium, NASA grant award NNH19ZHA001C, NSF grant award 1725937, NIH grant awards UL1TR001417, P01HL066299, R01HL137030, the University of Alabama at Birmingham Center for Clinical and Translational Science (CCTS), Murray Bander Faculty Development Award, and the Economic Development Partnership of Alabama.

Acknowledgements

This work was a collaboration between the College of Medicine and College of Engineering at the University of South Alabama. We would also like to acknowledge Jack Di Palma and the University of South Alabama Gastroenterology Division for helpful discussions of endoscope technologies and feedback for generating the Pugh matrix.

Conflicts of Interest

Leavesley and Rich disclose financial interest in a start-up company, SpectraCyte LLC, founded to commercialize spectral imaging technologies.

References

The reference section for this manuscript has been combined in the dissertation reference section.

CHAPTER IV: EXCITATION-SCANNING HYPERSPECTRAL VIDEO ENDOSCOPY: ENHANCING THE LIGHT AT THE END OF THE TUNNEL

This chapter details the LED-based endoscope platform benchtop testing for feasibility. This manuscript has been peer reviewed and published in Optica Publishing Group's Biomedical Optics Express journal.

C.M. Browning, J. Deal, S. Mayes, A. Arshad, T. C. Rich, and S. J. Leavesley, "Excitation-scanning hyperspectral video endoscopy: enhancing the light at the end of the tunnel," Biomed. Opt. Express 12, 247 (2021).

© 2020 Optical Society of America under the terms of the [OSA Open Access Publishing Agreement](#)

Abstract

Colorectal cancer is the 3rd leading cancer for incidence and mortality rates. Positive treatment outcomes have been associated with early detection; however, early stage lesions have limited contrast to surrounding mucosa. A potential technology to enhance early stage detection is hyperspectral imaging (HSI). While HSI technologies have been previously utilized to detect colorectal cancer *ex vivo* or post-operation, they have been difficult to employ in real-time endoscopy scenarios. Here, we describe an LED-based multifurcated light guide and spectral light source that can provide

illumination for spectral imaging at frame rates necessary for video-rate endoscopy. We also present an updated light source optical ray-tracing model that resulted in further optimization and provided a ~10X light transmission increase compared to the initial prototype. Future work will iterate simulation and benchtop testing of the hyperspectral endoscopic system to achieve the goal of video-rate spectral endoscopy.

Introduction

The suffix -scopy comes from the Greek word *-skopia* meaning “view, observe”¹⁵⁴. In modern English the suffix implies use of an instrument, referred to as a “-scope”, to examine aspects of the universe. To examine our world (or other worlds) we use a telescope/telescopy, to see the world invisible to the naked eye we use a microscope/microscopy and to see internal cavities of the human body we use endoscopes or bronchoscopes/endoscopy. Endoscopes visualize the upper and lower gastrointestinal (GI) tract for abnormalities such as Barrett’s esophagus, diverticulitis and colorectal cancer. Bronchoscopes are used to visualize the first three major branches of the bronchial tract in the lungs to detect and characterize fluid accumulation, asthma, COPD and lung cancer.

Lung and colorectal cancers are among the top three cancers in incidence and mortality rates in the United States^{5,6}. Interestingly these high risk cancers occur in organs that we have the ability to access and visualize. The gold standard screening technology is white light endoscopy (WLE) for the GI tract and white light bronchoscopy (WLB) for the bronchial tract. However, early stage lesions may often go undetected during an endoscopic screening^{8,28}. Prior studies of colorectal endoscopy effectiveness

have documented limitations that include: low contrast of early stage or small lesions compared to the surrounding mucosa and the limited ability to determine the metastatic or invasive potential of lesions^{155,156}. Hence, a key limitation in endoscopy is the ability to visualize and accurately classify types of lesions. Miss rates for colorectal lesions may involve an expertise bias factor, where novice gastroenterologists or medical students have shown higher miss rates than experts²². Pulmonology studies have demonstrated similar detection limitations when examining the upper airways^{32,150,157}. Newer modalities have been developed for enhanced visualization of endoscopically-accessible organs including: chromoendoscopy (CE), narrow-band imaging (NBI), autofluorescence imaging (AFI), radial endobronchial ultrasound (R-EBUS) and optical coherence tomography (OCT)^{20,21,23,29,157-159}. Unfortunately, newer macroscopic imaging techniques (CE, NBI and AFI) have shown minimal improvements for detection accuracy and exterior scans (R-BUS and OCT) of the peripheral bronchial tree are in the infancy stages of development. Hence, there is a need for improved endoscopic imaging technologies that can provide enhanced contrast between “normal” tissue and abnormalities and determine the composition of those abnormalities (estimation of composition, staging and metastatic potential).

One solution may be to incorporate hyperspectral imaging (HSI) into routine endoscopic screening procedures. Hyperspectral imaging captures a two-dimensional spatial image over a range of wavelengths creating a hyperspectral image cube. Each pixel is a spectrum that can be analyzed to estimate the abundance of respective components in that pixel. Hyperspectral imaging can be implemented over different wavelength ranges using different contrast modalities, including reflectance or

fluorescence. The broader utility of hyperspectral imaging has been demonstrated in remote sensing notably through agriculture and archaeology^{14,16,35,38}, food processing^{40,160}, historical documentation and art preservation^{42,41}. Within the medical field, HSI has been exemplified through image guided surgeries and cancer detection^{17,161–163}. Studies that have incorporated spectroscopic techniques, with a focus on HSI, into endoscopy thus far have integrated one of the following: a change in the light path, a separate probe (i.e. Raman) through the endoscope working channel or a hyperspectral camera^{164–166}. The latter two approaches are more prevalent in gastroenterology literature. Prior studies have compared the spectral characteristics of healthy and cancerous tissues *in vivo* using a hyperspectral endoscopic setup with narrowband filter wheels⁴⁵. The feasibility of an *in vivo* Raman probe was also investigated by introducing the probe through the working channel of an endoscope for the detection of gastric cancer⁴³. Additional studies have shown that reflectance spectral data in the visible¹⁶⁷ and infrared⁵³ ranges can be used to characterize healthy and cancerous gastric tissues. Finally, preliminary *ex vivo* studies have shown that colorectal tissues may be classified using spectral image data, as referenced to histopathology⁴⁷. However, there are four key aspects of prior studies that point to the limitations of current HSI and spectroscopic techniques in endoscopy and the need for further technology development: 1) prior studies have been performed almost exclusively *ex vivo* using resected tissues, 2) the majority of prior studies have utilized reflectance spectroscopic data, 3) single-point measurements, such as with Raman spectroscopy probes, have not been able to visualize large tissue areas as would be needed for real-time screening and 4) snapshot HSI approaches provide spectral information at the price of reduced resolution

and loss of signal. While many prior studies indicate an end-goal of developing real-time endoscopic imaging systems, the majority of prior work has been limited to *ex vivo* preparations, likely due to a combination of challenges including those associated with obtaining IRB and regulatory approval, difficulties associated with implementing an integrated real-time HSI endoscope system, and the limited signal strength available if the HSI approach is implemented at video-rate speeds^{47,53,167}. Correspondingly, most prior HSI studies have utilized only reflectance spectral data, as the signal strength is higher than fluorescence and much higher than Raman modalities^{45,47,53,167}. However, there is likely valuable information contained in fluorescence spectral data and an approach that could sample both reflectance and fluorescence modalities could provide enhanced visualization and diagnostic capabilities. Normal and abnormal tissues are expected to present distinct spectral differences due to changes such as reflectance vascular density or fluorescence metabolism markers^{29,168,169,146,170–172}. Hence, using a mixture of reflectance and fluorescence spectral signals could provide additional contrast needed to enhance visual differences between tissue types and improve visualization. A subsection of endoscopic spectroscopy studies involve single-point measurements including diffuse optical and Raman spectroscopy which can provide detailed molecular composition, but only of a single point in the tissue⁴³. The main limitation of these techniques is the need to sample the tissue on a point-by-point basis, which may lead to long procedure times. Lastly, many prior studies implementing HSI into endoscopy have used the snapshot technique to acquire a spectral image stack^{47,53,167}. However, this approach may be limited in that it requires a trade-off between reduced spatial and spectral resolution⁴⁹. Hence, challenges remain in developing a viable endoscopic HSI

platform, but regardless of the approach, a new HSI technology needs to provide a comparable field of view (FOV) to the gold standard WLE, *in vivo* capabilities and video-rate image data acquisition, preferably with the option to detect mixed modalities (reflectance and fluorescence).

We have previously reported on the use of excitation-scanning hyperspectral imaging to discriminate fluorescent markers (nuclei, green fluorescent proteins and tissue autofluorescence) in mice lung tissue models^{48,147,173–175}. Our previous microscope-based approaches allowed collection of the entire fluorescence emission above a cut-off wavelength for each excitation wavelength band providing improved photon statistics and therefore a higher signal-to-noise ratio, when compared to similarly configured emission-scanning approaches. Furthermore, fluorescence microscopy image acquisition speeds were able to be increased by a factor of ~10X for excitation-scanning approaches compared to emission-scanning. However, a limitation of these prior implementations is that they used an array of thin film tunable filters to provide spectral excitation and the mechanical tuning required 50-200 ms to switch between wavelengths. Hence, while prior microscope-based systems have shown great potential for fixed and/or single field of view images, they have not been capable of acquiring video-rate hyperspectral image data. To develop an excitation-scanning hyperspectral imaging system for endoscopic use, wavelength switch times need to be much shorter – on the order of ~100 μ s. Here, we present an imaging approach that utilizes wavelength-specific LEDs as the spectral excitation source. Similar approaches found in literature for LED-based HSI systems were designed for diffuse, macroscopic reflectance imaging which has minimal ability to couple to an illumination fiber of an endoscope^{176,177}. Here, we developed a novel

multifurcated solid light guide to combine optical output from many LEDs and couple the output into an endoscope illumination fiber. The electronic switching of LEDs is on the order of 100 ns. In this manuscript, we present the initial specifications for a proof-of-concept LED-based spectral light source for endoscopy, initial benchtop testing and computational simulations to optimize the light path. Results demonstrate that excitation-scanning hyperspectral imaging for video-rate endoscopy is possible. A resulting system from this work could provide spectral endoscopy screening for enhanced visualization of colorectal cancers.

Methods

Here, we present an iterative, systems-based methodology for developing the prototype spectral endoscope system that includes: 1) optical simulations of a proof-of-concept multi-branched solid light guide, 2) benchtop testing a LED-based spectral light source with the fabricated proof-of-concept solid light guide for endoscopic settings, and 3) revised optical simulations for further improving the solid light guide that lead to an optimized design for the spectral illumination assembly. The initial iteration of a multi-branched solid light guide is referred to as the alpha light guide design phase and the revised iteration of the light guide is referred to as the beta light guide design phase. Parametric optical simulations for the beta light guide are further divided into 3 tiers: Tier 1 – single lightpipe parameters, Tier 2 – combining lightpipe branches and Tier 3 – optimized multi-furcated solid light guide designs. For this manuscript a light guide refers to a combination of lightpipes. A key element of the system is an array of wavelength-specific LEDs to provide the spectral illumination to the endoscope. Herein,

we use the term λ LED to denote wavelength-specific LEDs and as a reminder that many narrowband (typically 20 nm FWHM) light sources are utilized for spectral illumination.

Proof of concept λ LED -based spectral light source.

Alpha light guide design – To assess the feasibility of a spectral endoscopic light source based upon multiple λ LED sources combined through a multifurcated solid light guide, we first developed computational models of solid light guides. We then manufactured a proof-of-concept alpha prototype solid light guide from the simulation results and performed bench testing for optical efficacy. We then constructed a spectral light source utilizing the alpha prototype solid light guide and coupled the spectral light source to an endoscope. All light path modeling was simulated using Monte Carlo-based optical ray tracing software (TracePro, Lambda Research Co.). To assess repeatability of the ray tracing, an initial simulation was performed 5 times with 1,000,000 rays traced. The output irradiance of the system was measured and found no variation between subsequent ray traces. This was deemed a statistically sufficient number of rays to accurately model the simulations for this study. To verify that 1,000,000 rays were accurate, we also performed simulations with 100,000 and 5,000,000 rays and found that the output irradiance varied by less than 0.05%. The materials and parameters selected for the light path components of the alpha design are summarized in Table 2.

Table 2. Key parameters used for ray trace simulations of the alpha phase multi-furcated light guide

| | | |
|---|---------------------------|-----------------|
| Light Source: Cree® LED C503B-BAS/BAN/GAS/GAN | Wavelength (nm) | 527 |
| | Luminous Intensity (cd) | 30 |
| | Radiated Power (mW) | 10 |
| | Full Viewing Angle (°) | 15 |
| | Rays Traced | 1,000,000 |
| Optics: Light Guide | Material/Refractive Index | Plexiglass/1.49 |
| | Distance from Source (mm) | 2 |
| Detector/Interrogation Plane/Irradiance Map | Diameter (mm) | 50 |
| | Distance from Guide (mm) | 50 |

The alpha light guide computational models simulated a LED light source (Cree® LED C503B-GAS, Cree Inc.) with a narrow (15° full angle) angular illumination distribution. Light was directed through a solid lightpipe or light guide using material properties with a refractive index of 1.49 (Plexiglass). The emitted flux from the output of the light guide was measured at the exiting face and with an interrogation plane perpendicular to the light guide output. Percent transmission through the light guide (e.g., optical efficiency) and the illumination distribution were calculated.

The alpha light guide computational models tested individual geometric parameters including lightpipe diameter, arc length of lightpipe curvature (as a function of radius and angle of the curvature), branching structures and spacing between distal branches of a light guide. The geometries for the alpha phase design were rendered using CAD (Autodesk Inventor, Autodesk Inc.) and imported to TracePro. A circular cross-section was used for all lightpipe and light guide geometries. Transmission throughput was calculated by dividing the output flux from the common end of the light guide by the input flux to the light guide branches from the λ LED. From these tests and data, a final alpha phase 16 branched solid light guide was designed in CAD (Autodesk Inventor,

Autodesk Inc.) then imported into TracePro for final optical simulations (see Figure 9). A ray trace was performed for each input branch to determine transmission throughput and loss per branch. This design was used to assess the initial feasibility of utilizing a multifurcated light guide for a λ LED -based spectral light source.

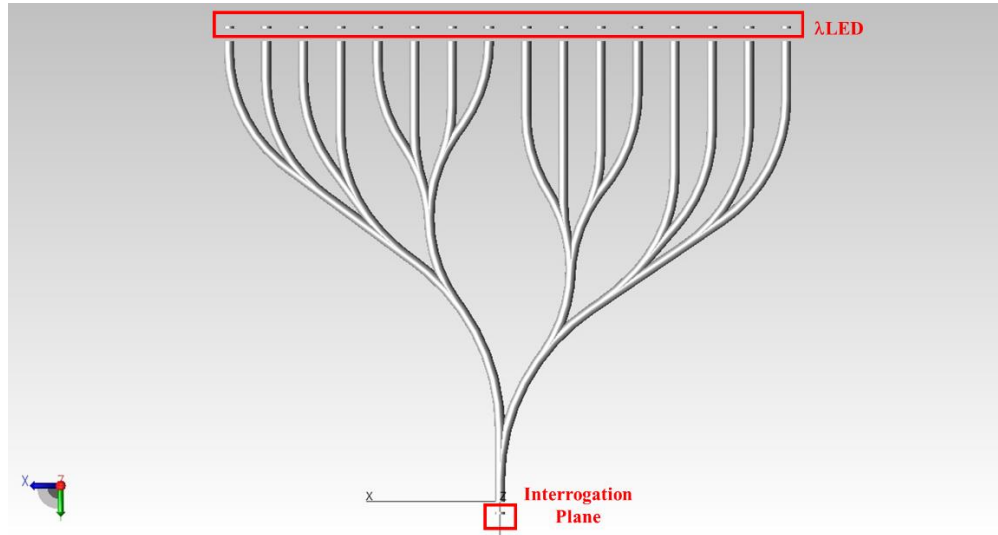


Figure 9. Rendering of the alpha phase multi-branched solid light guide in ray tracing software for simulated optical analysis. The small disks at the top of the rendering modeled the illumination from each LED. The small disk at the bottom of the model is the exit surface, interrogation plane.

Spectral endoscopic light source – The alpha light guide design was fabricated by injection molding of optical grade acrylic to combine an array of wavelength-specific LEDs (λ LEDs) to a common output. High-powered surface mount λ LEDs (SMBBXXX-XXXX-XXX, Marubeni Co.) were implemented with an average (full) viewing angle of 22° and power outputs ranging from 120 to 750 mW, depending on wavelength. A custom printed circuit board (PCB) was designed (Pad2Pad, Pad2Pad Inc.) to align λ LEDs with distal light guide branches. A coupler from a commercial endoscopic light source (Olympus CLK-4, Olympus Medical Systems Corp.) was integrated to align the

optical, proximal output of the light guide with the illumination input of a compatible fiber scope (Olympus CF-P20S). A second custom PCB employed current drivers (RCD-XX-X.XX, RECOM Power) to independently control intensity and cycling of each λ LED. Other electronic components included a 15V power converter and a relay switch to supply standard facility power to the current controller PCB. The electrical interface is further detailed using a system architecture internal block diagram (IBD) (Figure 10). Additional mechanical components included an internal fan for LED heat dissipation and an air pump for potential tissue/cavity inflation scenarios through the scope. The multifurcated solid light guide was fabricated to be approximately 9" length by 12" width, and was housed within the complete spectral light source rackmount (25" L x 19" W x 7" H). These system details can be seen in Figure 11.

The IBD presents the flow of power to illuminate the λ LEDs and the signals used to control the intensity and cycle of illumination. The perimeter in Figure 10 defines the black box boundaries of the electrical subsystem with inputs on the left and outputs on the right. The electrical and optical subsystems are prioritized to emphasize the novel features and techniques developed for the hyperspectral endoscope system. The completed spectral light source was coupled with a retired Olympus CF-P20S endoscope for proof-of-concept benchtop testing (Figure 11).

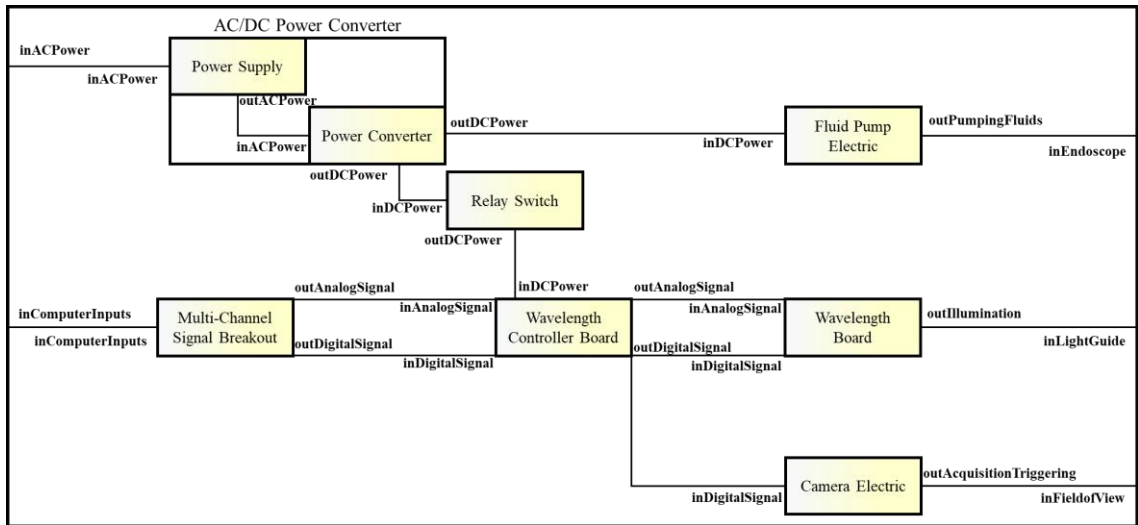


Figure 10. A systems architecture internal block diagram view of the electric interface of the hyperspectral endoscopic light source, specifically for the alpha design proof-of-concept light source.

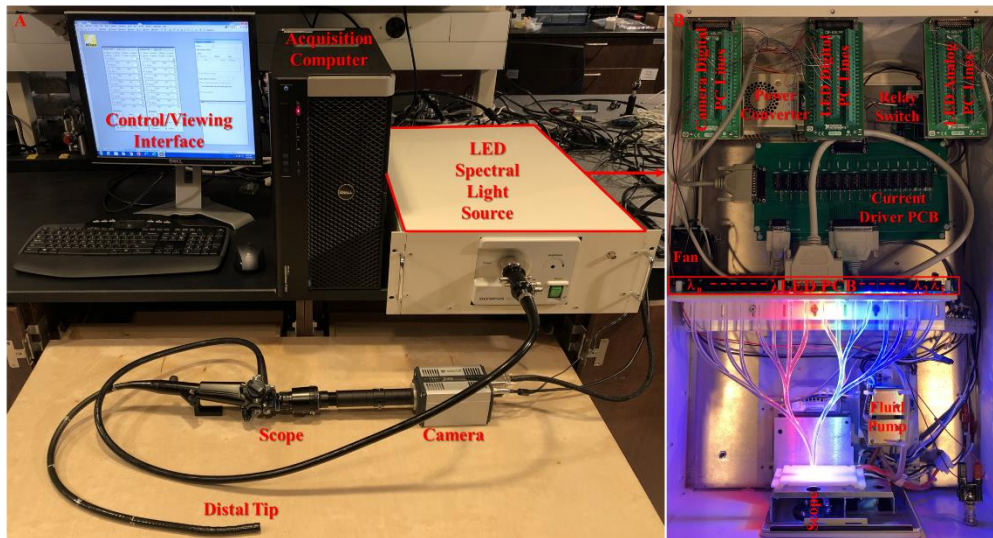


Figure 11. Complete proof-of-concept spectral endoscope system overview. (A) System photograph with labels for the major subsystems: computer, spectral light source, scope and camera. (B) Top view of the spectral light source with labels for the key electronic components previously described in Fig.2. The spectral light source optical pathway combines illumination from the λ LEDs into a single output using a novel multi-branched solid light guide. The output is then coupled to the illumination fiber of a standard endoscope.

Benchtop testing alpha hyperspectral endoscopic system consisted of determining optical power throughput and testing image quality in tissue models. The transmission

intensity was measured using a spectrometer (QE65000, Ocean Optics) and integrating sphere (4P-GPS-030-SF, Labsphere) calibrated to a NIST-traceable response using a standardized light source (LS-1-CAL, Ocean Optics). All measurements were acquired by averaging 10 scans of the spectrometer. Irradiance data was collected from: 1) the raw λ LED, 2) the output of the light guide coupled to the λ LED and 3) the output of the endoscope coupled to the light guide and λ LED. Measurements were acquired over a range of currents supplied to the λ LED, as regulated using an analog reference voltage signal supplied by a National Instruments PCI-6723 card to the current drivers (the Multi-Channel Signal Breakout of Figure 10). The current drivers supplied current to each λ LED with an output that was inversely proportional to the analog reference voltage supplied to the driver (reference voltage ranged from 5V to 0.5V in increments of 0.5V). The maximum power output from the light guide and from the endoscope were divided by the maximum raw λ LED power to calculate the % transmission through each stage of the system. The range of power measurements was used to provide a correlation between power output and analog reference voltage inputs to ensure a flat spectral output (i.e., even illumination intensity across all λ LEDs).

Preliminary tissue images were acquired using an external camera (Zyla 5.5, Andor) and relay lens assembly coupled at the endoscope eyepiece. Discarded swine tissues were obtained from the University of South Alabama Vivarium, following IACUC-approved procedures associated with medical student and surgical fellow training. Samples were rinsed thoroughly with phosphate buffered saline (PBS) and attached to a mechanical holder such that the proximal end of each tissue was clamped shut and the distal end was open to allow endoscope insertion. The endoscope was inserted and sample images and

video feed were acquired at several locations. A range of acquisition times and illumination intensities were compared to determine optimal settings.

Optimized ray trace modeling.

Benchtop testing and tissue imaging results from the alpha phase light source (results in Section 3.2) indicated feasibility of a multi-branched light guide for spectral illumination, however, further investigation for optimal geometric design of the light guide was needed. Therefore, a second iteration (beta phase) of computational ray trace models was developed to determine an optimal multi-branched light guide design. Optical material and geometric parameters were updated to better match the physical properties of the high-power λ LEDs in benchtop testing and from the knowledge of the alpha light guide simulations (Table 3).

Table 3. Key parameters used for ray trace simulations of the beta phase multifurcated light guide

| | | |
|---|---------------------------|------------------|
| Light Source: Marubeni LED SMB1N-525-02 | Wavelength (nm) | 525 |
| | Luminous Intensity (cd) | 270 |
| | Radiated Power (mW) | 230 |
| | Full Viewing Angle (°) | 22 |
| | Rays Traced | 100,000 |
| Optics: Light Guide | Material/Refractive Index | Acrylic/1.49 |
| | Distance from Source (mm) | 2 |
| Detector/Interrogation Plane/Irradiance Map | Surface Property | Perfect Absorber |
| | Diameter (mm) | 5 |
| | Distance from Guide (mm) | 2 |

The optical parameters of the high-power λ LEDs, acquired for the proof-of-concept light source, were imported from the manufacturer specifications sheet using the Surface Source Property Editor in TracePro for the ray tracing analysis. The model repeatability analysis mentioned above was conducted to determine the number of rays

required to yield repeatable model results in efficient time periods. Tracing 100,000 rays yielded sufficient repeatable results (repeatability fluctuation of $\leq 0.05\%$), while allowing for relatively rapid computational times when iterating through geometric parameter values. The light guide material was adjusted to match the fabricated alpha light guide. The size and placement of the interrogation plane was adjusted to more accurately predict the coupling efficiency with an endoscopic illumination fiber. Mechanical, non-optical components were not included in the ray trace simulation. In addition, the CLK-4 coupler was not included in the ray trace simulation, as it is part of the detection pathway and the ray trace simulation was performed to optimize the illumination optics. A parametric simulation process was used that varied one or more geometric variables independently (i.e., arc length or wavelength illuminated). A separate iteration of the model was performed for each value of each independent variable. The output of each iteration was saved in the form of an irradiance map of the interrogation plane and % transmission of the light guide. Irradiance maps were normalized to the emitted flux of the LED. This process was repeated for every value of the independent variable for every independent variable altered.

Performance requirements of the beta phase model were defined in order to achieve improved physical outcomes over the alpha phase prototype: 1) The endoscopic system as a whole should be capable of providing an optical output of 10 mW at each wavelength band. 2) The optical output of the multifurcated light guide should have a numerical aperture equal to or less than that of the endoscope/bronchoscope illumination fiber to enable efficient optical coupling. 3) The optical output should be stable and the output at each wavelength band should be equal in order to achieve flat spectral

illumination. Manufacturer properties for each λ LED were tabulated and compared in order to ensure that a flat spectral profile could be achieved for a specified optical illumination power (Table 4).

Table 4. Manufacturer-supplied properties of the high-powered surface mount LEDs used in the beta phase simulations and in the alpha phase prototype. Physical light sources were used in the prototype spectral light source (Figure 11) and digital light sources, by importing the optical properties to TracePro for simulation loops (first column). The tabulated data were used to determine the theoretical % transmission required at each wavelength of LED to achieve a specified power output. As an example, if the desired power output is specified as 10 mW, the 395 nm LED chip can achieve this power output even if the transmission of the spectral system is as low as 1%, while the 590 nm LED (a lower output chip than 395 nm chip) would require 8% transmission to achieve an optical power output of 10 mW.

| Macro List Identifier | Marubeni LEDs | Forward Current (mA) | Radiated Power @ Current Forward (mW) | Desired Power Output (mW) | | | | | | |
|-----------------------|---------------|----------------------|---------------------------------------|---------------------------|-----|-----|-----|-----|-----|-----|
| | | | | 10 | 20 | 30 | 40 | 50 | 60 | 70 |
| 1 | SMB1N-365V-02 | 500 | 500 | 2% | 4% | 6% | 8% | 10% | 12% | 14% |
| 2 | SMB1N-375V-02 | 500 | 560 | 2% | 4% | 5% | 7% | 9% | 11% | 13% |
| 3 | SMB1N-395V-02 | 500 | 750 | 1% | 3% | 4% | 5% | 7% | 8% | 9% |
| 4 | SMB1N-405V-02 | 500 | 710 | 1% | 3% | 4% | 6% | 7% | 8% | 10% |
| 5 | SMB1N-420H-02 | 350 | 420 | 2% | 5% | 7% | 10% | 12% | 14% | 17% |
| 6 | SMB1N-D450-02 | 350 | 480 | 2% | 4% | 6% | 8% | 10% | 13% | 15% |
| 7 | SMB1N-D470-02 | 350 | 470 | 2% | 4% | 6% | 9% | 11% | 13% | 15% |
| 8 | SMB1N-490H-02 | 350 | 240 | 4% | 8% | 13% | 17% | 21% | 25% | 29% |
| 9 | SMB1N-515V-02 | 350 | 250 | 4% | 8% | 12% | 16% | 20% | 24% | 28% |
| 10 | SMB1N-D520-02 | 350 | 250 | 4% | 8% | 12% | 16% | 20% | 24% | 28% |
| 11 | SMB1N-525V-02 | 350 | 230 | 4% | 9% | 13% | 17% | 22% | 26% | 30% |
| 12 | SMB1N-590-02 | 350 | 120 | 8% | 17% | 25% | 33% | 42% | 50% | 58% |
| 13 | SMB1N-620-02 | 350 | 190 | 5% | 11% | 16% | 21% | 26% | 32% | 37% |
| 14 | SMB1N-D630-02 | 350 | 330 | 3% | 6% | 9% | 12% | 15% | 18% | 21% |
| 15 | SMB1N-D660-02 | 350 | 250 | 4% | 8% | 12% | 16% | 20% | 24% | 28% |
| 16 | SMB1N-670D-02 | 350 | 290 | 3% | 7% | 10% | 14% | 17% | 21% | 24% |
| 17 | SMB1N-680-02 | 600 | 170 | 6% | 12% | 18% | 24% | 29% | 35% | 41% |
| 18 | SMB1N-750-02 | 800 | 290 | 3% | 7% | 10% | 14% | 17% | 21% | 24% |
| 19 | SMB1N-810D-02 | 800 | 560 | 2% | 4% | 5% | 7% | 9% | 11% | 13% |
| 20 | SMB1N-850D-02 | 1000 | 650 | 2% | 3% | 5% | 6% | 8% | 9% | 11% |
| 21 | SMB1N-940D-02 | 1000 | 630 | 2% | 3% | 5% | 6% | 8% | 10% | 11% |

The following two sections describe the systematic and parametric evaluation of the beta phase light guide. The first section (Tier 1 & 2) describes simulation of single (unbranched) and dual (converging two lightpipe branches together) lightpipe geometries. The second section (Tier 3) describes simulation of more complex multi-branched solid light guide models.

Lightpipe simulations (Tier 1 & 2) – Tier 1 beta phase models were similar in design to models of the alpha phase light guide, but with updated variables and material properties. Parametric sensitivity studies evaluated effects of lightpipe diameter, length and curvature. Tier 2 beta phase models studied the optical tendencies of two merging lightpipes and evaluated the effects of alternating the spacing between the distal ends of merged lightpipes.

Multifurcated light guide simulations (Tier 3) – Tier 3 of the ray trace modeling for the beta phase multi-branched solid light guide implemented key findings and optical geometry values from the Tier 1 (single lightpipe curvature) and Tier 2 (merging two lightpipes together) models to create new light guide geometries. The creation of new geometries focused on size of curve (radius and angle), how the branches merged and the final size of the completed model. Four multi-branched solid light guide geometries were rendered and evaluated. The independent variables for these models included the selection of the distal branch of the light guide that was coupled to the λ LED and the wavelength of the λ LED used. For all of the model geometries, branch one was denoted as the branch at the bottom-right of the viewing window, with branch numbers increasing for every branch above. A range of wavelength bands (LED model numbers and associated optical properties) were evaluated, from 365 nm to 940 nm (Table 4) to observe any changes in transmission between branches and to identify which wavelengths had improved transmission.

A symmetrical design (Figure 12.D) was evaluated that combined 16 branches with 4 merge points. The percent transmission was measured after each merge point (the addition of merge points/branches are shown in each row of Figure 12) and at the final

common exit of the light guide in order to assess the location(s) of the greatest loss in transmission. A related design was also evaluated that utilized 2 merge points (Figure 12.F). In addition, a “wave shaped” light guide was developed with either 8 or 16 branches, where all branches followed the same path and curved the same direction with arbitrary spacing between each branch (Figure 12.G-H). As opposed to the symmetrical designs, the “wave shaped” designs had only one main merge point. An additional “wave shaped” light guide (Figure 12.I) was also evaluated that utilized a 45° sweep angle instead of a 90° sweep angle.

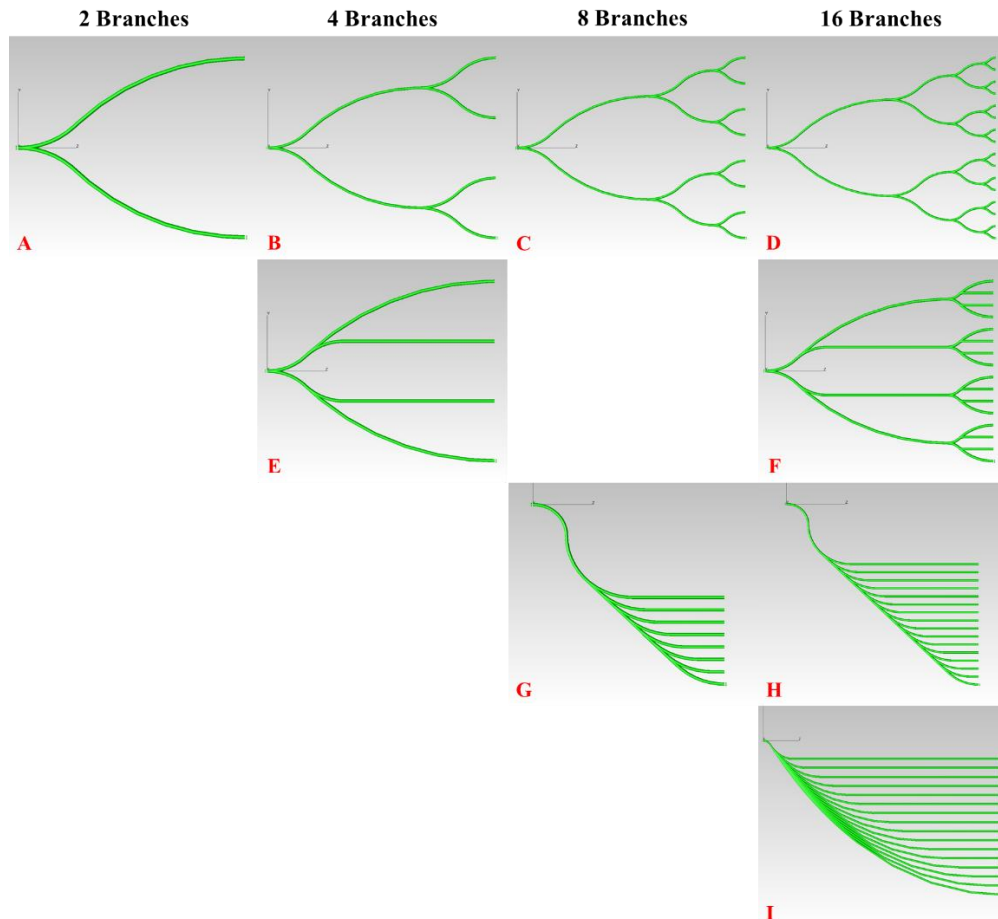


Figure 12. TracePro rendering of the models used in simulation to observe the transmission of light through a multi-branched solid light guide. The percent transmission of each light guide branch was monitored for the symmetrical model at (A) two branches, (B) four branches, (C) eight branches and (D) sixteen branches. A symmetrical model with a reduced number of merge points at (E) four branches and (F) sixteen branches was also evaluated. In addition, a non-symmetrical geometry that was labeled a “wave shaped” geometry was evaluated for (G) an eight-branch light guide with 90° sweeping angles, (H) a sixteen-branch light guide with 90° sweeping angles and (I) a sixteen-branch light guide with 45° sweeping angles.

Results and Discussion

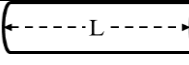
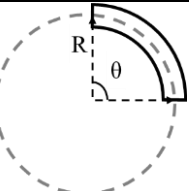
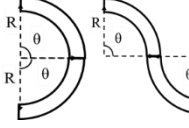
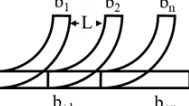
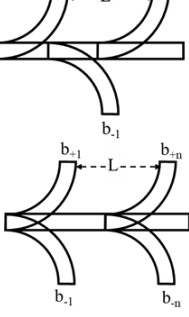
Spectral imaging holds great promise for translation into biomedical screening devices such as endoscopes. Narrow-band imaging and autofluorescence imaging have integrated aspects of spectral specificity into endoscopy but only with one or two bandwidths of illumination. The technology presented here allows many bandwidths of illumination providing a more complete spectral analysis. Resulting spectroscopic data

could provide an enhanced visualization of blood flow or metabolic changes in real time. However, studies thus far that have accomplished spectroscopic imaging in endoscopy via snapshot, Raman or filtering techniques cannot provide substantial spatial and spectral resolution or real-time operations. Our prior work with excitation-scanning hyperspectral imaging reduces the emission filtering to increase acquisition speeds (3 s per spectral image using emission-scanning to 300 ms per spectral image using excitation-scanning). This work presents further reduction of illumination filtering by introducing λ LEDs to achieve spectral imaging. To our knowledge, this is the first implementation of a multifurcated solid light guide for providing wavelength-band illumination for spectral imaging.

Alpha light guide models

Here, we describe a parametric modeling approach and subsequent prototyping efforts and proof-of-principle testing to evaluate the potential of a multi-channel light guide for use in spectral imaging applications. The single lightpipe parametric tests and merging lightpipes tests led to the proof-of-concept solid light guide design from Figure 9. Alpha phase ray trace simulations measured the output flux at the respective surfaces of a given light guide configuration divided by the total power output of the λ LED (10 mW) to determine the transmission efficiency. A summary of all alpha phase model results is given in Table 5.

Table 5. Summary of results from the alpha phase multi-branched solid light guide ray tracing modeling. Columns 2 and 3 indicate the independent variables that were iteratively tested over the range of values, respectively. Column 4 provides an illustration of each lightpipe model geometry. Column 5 summarizes the results of each parameter tested.

| Parameter | Independent Values | Ind. Value Ranges | Visualization | Results |
|------------------------|--------------------------|---|--|--|
| Lightpipe Diameter | Diameter (mm) | 1, 5, 10, 25, 50 |  | 92% with 10 mm diameter |
| Lightpipe Length | Length (mm) | 10, 50, 250, 500, 750, 1000 |  | ~60% independent of length |
| Lightpipe Curve | Angle (°) Radius (mm) | 30°-180° increments of 15° at 50 mm radius 10-50 increments of 10, 100, 150, 300, 500 at 60° angle |  | 55% max for all θ values above 100 mm radius |
| Lightpipe Double Curve | Angle (°) Radius (mm) | Same ranges holding the first curve constant at given values iterating on the second curve |  | The results are the same as the single curve above |
| Number of Lightpipes | Branches (b_n) | 1 Branch - 6 Branches |  | ~20% illumination reduction for each branch increase |
| Lightpipe Spacing | Length (mm) | <u>Parallel:</u> 10, 15, 20, 40 <u>Staggered:</u> 20 if Adjacent, 10 if Opposite. <u>Mirrored:</u> 20 |  | Spacing has NO effect on the transmission |

Optical transmission increased with increasing lightpipe diameter ranging from 3-95%. The alpha phase light guide was modeled with a diameter of 5 mm (73% for this diameter) to couple with the high power λ LEDs (with a lens diameter of 5 mm on the LED chip) while maintaining a smaller footprint for the light guide. Transmission through increasing lightpipe lengths resulted in a transmission range of 56-60%.

Lightpipe curvature (a function of the radius and angle of a circumscribed arc) testing resulted in a transmission increase with increasing arc radius to a maximum transmission of ~55% for arc radii ≥ 100 mm, for all angles tested. Bifurcated lightpipe geometries were also evaluated that consisted of a curved lightpipe (radius: 20 mm angle: 90°) merged with a straight lightpipe. Additional branches were added at equidistant spacing to study the effects of lightpipe furcation, with increasing branch numbers (branch 1 was designated as the branch closest to the common output and branch n as the farthest). Branch positions and spacing were evaluated iteratively. Increasing branches decreased the transmitted light at the output from 66% (for 1 branch) to 7% (for 6 branches). Additional multifurcated models were implemented to evaluate the effects of staggered and mirrored branch geometries, with similar results to the parallel branching model. Spacing between branches presented negligible changes in the transmitted light for all configurations.

The results of the alpha phase ray trace modeling provided a foundation to design an initial proof-of-principle multifurcated light guide. An initial design was developed that combined 16 branches to a common output. The alpha design light guide was constrained to 2 dimensions to simplify injection-mold fabrication. Spacing between the distal branches was set 20 mm apart to create a linear λ LED array and allow sufficient spacing between λ LEDs for heatsinks and cooling. The curvature of each branch was selected as a compromise between achieving optical transmission (as a result of previous ray tracing results) and overall size (footprint) of the light guide. Distal curves were specified with a radius of 70 mm and angle of 35° , while proximal curves were specified with a radius of 100 mm and angle of 37° . The larger proximal curves and the smaller

distal curves allowed reduced converging angles among branches. The resulting alpha light guide design was constructed in CAD (Autodesk Inventor, Autodesk Inc.) and imported into TracePro for analysis. Ray trace modeling of the final alpha light guide design resulted in optical transmission ranging from 11% transmission for selected middle branches to 49% transmission for outer branches. At the conclusion of the alpha phase modeling, a prototype alpha phase light guide was manufactured by Apollo Optical Systems, Inc. An injection mold was constructed and the light guide produced from optical grade acrylic according to the design specifications of the CAD drawing. The alpha phase light guide was then evaluated using bench testing and subsequently incorporated into a prototype spectral illuminator for coupling to a fiber-based endoscope, as described below.

Benchtop testing prototype

A proof-of-concept spectral light source was designed to evaluate the ability of the multifurcated light guide to combine optical output from an array of λ LEDs to a common output that could be coupled to the illumination fiber of a commercial endoscope. Benchtop testing included evaluation of the optical transmission of the multifurcated light guide, the transmission of the light guide + endoscope assembly and acquiring initial feasibility image data. Radiant flux and transmittance were measured for each λ LED of the system, as well as through the alpha phase multifurcated light guide, and through the light guide + endoscope. Irradiance measurement stability (repeatability) was verified at 3 λ LEDs by repeating measurements 5 times, with a complete system restart between each test. The coefficient of variation for each λ LED ranged from 0.0015

to 0.0041, indicating high repeatability. The λ LED-based spectral light source + endoscope was then used to acquire test images of swine colon. Test images included spectral reflectance and fluorescence (tissue autofluorescence) modalities (Figure 13).

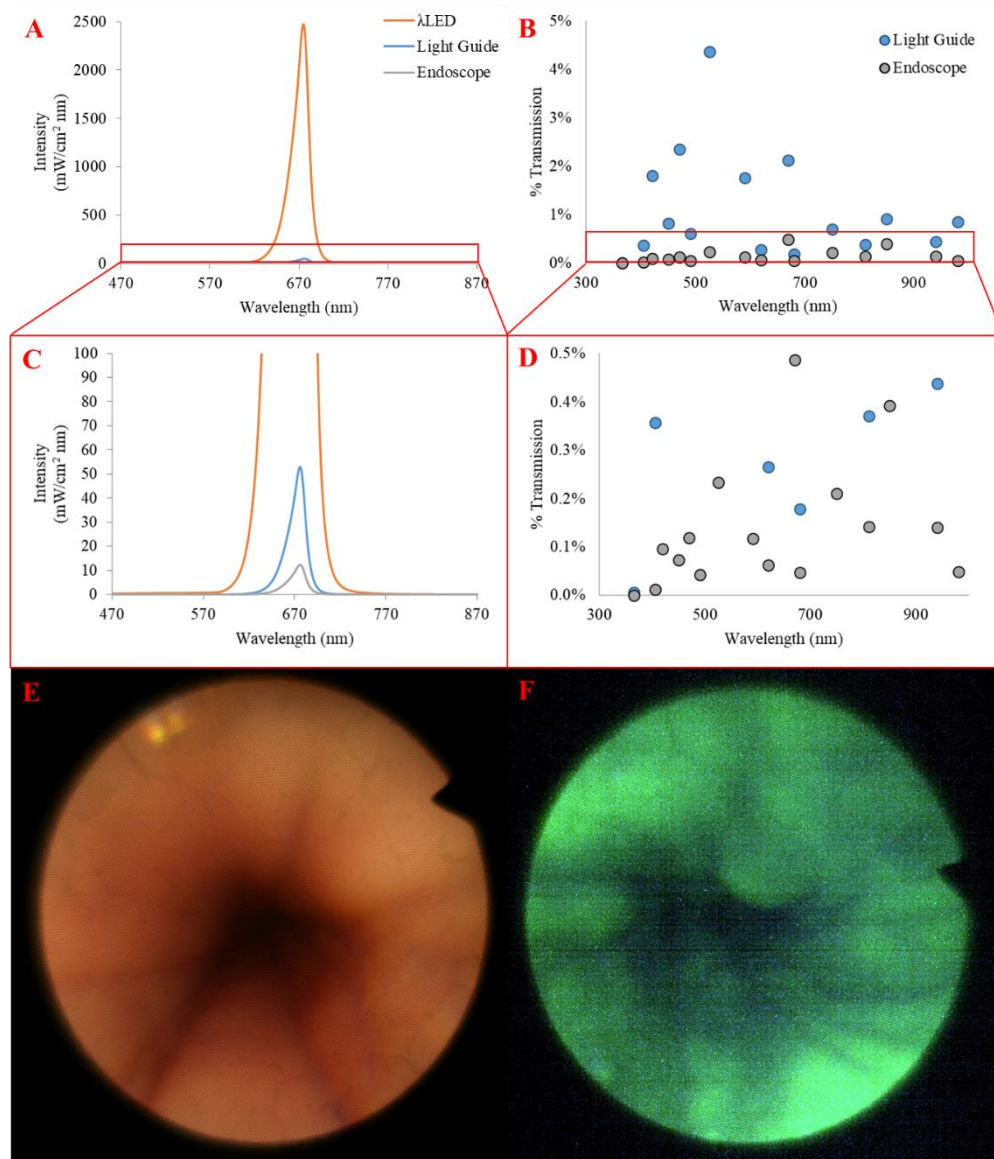


Figure 13. Results from benchtop testing the proof-of-concept light source for spectral LED (λ LED). (A) The spectroradiometric power of the 670 nm LED measured as the raw λ LED, as transmitted through the light guide and as transmitted through the light guide + endoscope assembly. (B) The illumination % transmission for each λ LED through the light guide as seen in Figure 11.B and through the light guide + endoscope. The subtrahend from these data would be the losses through the light guide and endoscope respectively. (C) Irradiance data from panel A rescaled to highlight the light guide and endoscope curves. (D) Transmission from panel B rescaled to highlight the lower transmission through the endoscope. The 365 nm LED did not transmit through the endoscope likely due to poor transmission through the illumination fiber. (E) An example false-colored reflectance spectral image stack and (F) a false-colored autofluorescence spectral image stack. Images false-colored according to wavelength using NIS Elements software (Nikon Elements).

Benchtop testing resulted in a relatively low optical transmission through the light guide (0.01% to 4.37% depending on branch). Coupling through the endoscope illumination fiber resulted in additional transmission loss of 2-4% (these losses are in line with expected transmission efficiencies through an endoscope illumination fiber). As an example, the raw output of the 670 nm λ LED achieved a peak spectroradiometric flux of ~ 2400 mW/cm² nm (Figure 13.A), while the power when transmitted through the light guide was ~ 60 mW/cm² nm and the power when transmitted through the light guide + endoscope was ~ 12 mW/cm² nm (Figure 13.C). The transmitted light was measured through the light guide for each λ LED in the set array and through the light guide + endoscope providing the output of the given λ LED-branch combinations for the current prototype assembly (Figure 13.B,D). The 365 nm LED did not transmit through this system. The assumption is that the filters and fiber material of the endoscope block any UV light from transmitting to the colorectum to minimize radiation damage. This longer UV wavelength LED was selected in the prototype's array to test a wide selection of λ LEDs for throughput and potential utility for fluorescence imaging by exciting known endogenous fluorescent tissue components (i.e. collagen, elastin or FAD)^{170-172,178}. Due to the injection-molded nature of the solid light guide (i.e., manufactured as a single optical component), it was not possible to experimentally measure optical loss or percent transmission changes that occurred as a result of light guide branching at the branch points. However, ray trace simulations indicate that branch points have a compounding effect of optical losses, with each branch point contributing a similar fractional transmission loss. Also, it should be noted that curvature of the endoscope itself could result in some small losses and to minimize this variable from the experiments the

endoscope was held straight for each test. In future work, light losses through the endoscope as a result of curvature will also be investigated^{179,180}.

Preliminary feasibility tests were also conducted using the spectral endoscope to image excised sections of swine colon. The power output of each λ LED was adjusted in order to achieve a uniform spectral illumination profile. In order to achieve a specified power output for each wavelength, some scenarios only illuminated a subset of λ LEDs available in order to provide the specified power to the endoscope tip. Therefore, the test images shown in Figure 13.E-F used a reduced number of wavelengths in order to achieve a flat spectral illumination profile. A reflectance spectral image stack was acquired (Figure 13.E) using λ LEDs from 450 nm to 940 nm (12 λ LEDs) at 0.3 mW illumination power and 100 ms integration time (1.2 s per image stack). If the full λ LED array were used it would take 1.6 s for a reflectance image stack at 100 ms per wavelength band. One aspect to note is the green and blue channels provided enhanced contrast of vascular structures, similar to NBI (better seen in Figure A1 & Figure A2). The fluorescence spectral image stack (Figure 13.F) used 3 λ LEDs (420 nm, 470 nm and 525 nm) at 0.3 mW, exciting fluorescence at wavelengths below the 560 nm emission filter cutoff. Spectral images were acquired at 10 seconds (30 s per image stack) to allow sufficient signal integration. This current setup could acquire a full fluorescence image stack in 160 s (2.67 min) if all 16 λ LEDs excited the FOV and the respective emission spectra was filtered to the detector. All images were false-colored by wavelength using NIS Elements software (Nikon Instruments). The power and acquisition times used for this initial feasibility test represent trade-offs between imaging speed and sensitivity as a result of the relatively low transmission of the alpha phase light guide and 0.3 mW of

illumination power. Images were acquired at the acquisition times stated above to provide the current optimal spatial resolution in an image (purely the qualitative best image acquired) and sample reflectance videos were captured with varied acquisition speeds to prioritize framerate with a distinguishable field of view (current optimum is 8 fps). It should be noted that we were not acquiring or detecting colorectal cancer in these samples, purely spectral imagery examples using an endoscope.

While the alpha phase prototype was sufficient to demonstrate proof-of-principle operation and allow acquisition of initial image datasets, the optical power available at the endoscope tip was low, resulting in poor signal-to-noise ratios (SNR) in the acquired images, especially when operating in fluorescence modality (Figure 13.F). Upon comparison between the optical transmission of the simulation (11% - 49%) and the physical prototype (0.01% - 4.37%), it became clear that a return to the computational ray trace software was required to both refine the accuracy of the model and to evaluate alternative design geometries in an effort to increase transmission efficiency. Within the TracePro environment, the light guide material was updated from plexiglass to optical acrylic. In addition, the λ LED was updated from the initial Cree 527 nm LED to a Marubeni 525 nm LED. Finally, the interrogation plane (detection surface) was resized to match the input fiber bundle of an endoscope (5 mm diameter instead of 50 mm) and moved closer to the output of the light guide (2 mm between instead of 50 mm). These changes resulted in transmission of 3.9% in simulation for the 525 nm LED, which better coincides with the measured 2.1% transmission from benchtop testing. The light loss with this proof-of-concept spectral light source is significant and does not currently allow for the real-time excitation-scanning hyperspectral imaging goal. However, with the resulting

transmission and the test images shown, it can be inferred that with adequate optical throughput we can achieve our excitation-scanning goals.

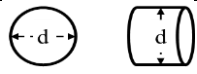
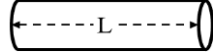
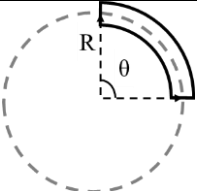
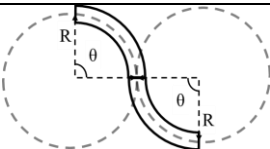
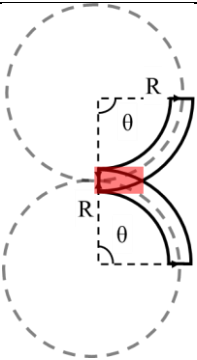
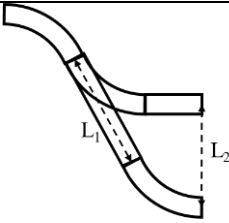
Beta light guide models

The benchtop testing of the alpha phase prototype was sufficient for demonstrating initial feasibility of the excitation-scanning approach in an endoscopic scenario, but did not provide sufficient illumination power necessary to achieve quality SNR fluorescence images (Figure 13.D). However, construction of the prototype system did provide an opportunity for model validation, revision of model parameters to better match real-world operation and revision of specifications for the desired end product. A beta light guide was next modeled using revised model parameters. Tier 1 & 2 ray tracing simulations reassessed the alpha phase modeling using these revised parameters and constraints. Results were consistent with the alpha phase models (Table 6).

For beta phase models, optical transmission increased with increasing lightpipe diameter, achieving a maximum of 86 % with diameters of 8 mm or larger. Optical transmission also increased for decreasing lightpipe length. However, even for long lightpipes (>100 mm) a minimum transmission of 72% was achieved. Curved lightpipes were defined as a function of the radius and angle of a circumscribed arc. All angle values tested ($15^{\circ} - 90^{\circ}$, in increments of 15°) resulted in an increase of transmission with increasing arc radius to a maximum transmission of ~50% for arc radii ≥ 100 mm. Double curved lightpipes exhibited no transmission differences from a single curved lightpipe. Bifurcated lightpipes (e.g., merging two single curved lightpipes) were defined by the arc angle and radius of the two branches. Of note, in the case of merging two curved lightpipes, the overlapping area of the lightpipes (at the intersection) is also a

function of the arc angle and radius of the lightpipes. Results from the bifurcated models indicated that the primary parameter regulating optical transmission was the arc radius, where a larger arc radius resulted in increased optical transmission, with a maximum of 35% achieved for an arc radius of ≥ 200 mm. The merger of a straight lightpipe with a curved lightpipe was also simulated. In this case, comparable lightpipe lengths were used for both branches (i.e., the length of the straight section was specified as equal to the arc length of the curved section). Results were similar to the results of merging two curved lightpipes. Hence, we can conclude that a similar transmission efficiency is achieved for the merger of two branches, regardless of whether two curved branches are merged or a curved branch and a straight branch are merged. Finally, lightpipe spacing was tested to see if it affected the internal reflection of light rays at the bifurcation points (i.e., reducing refraction and increasing transmission). For each distance between branches that was tested, one branch was illuminated while the output flux was measured at the common output and at the adjacent branch(es) to assess back illumination. Branch spacing had no effects on the transmission throughput (i.e., the transmission was approximately the same for each branch illuminated regardless of the distance between adjacent branches) and back illumination of adjacent branches was negligible.

Table 6. Individual geometric parameters simulated in TracePro for iterations of the beta phase multi-branched solid light guide. Columns 2 and 3 indicate the independent variables that were iteratively tested and the range of values tested. Column 4 provides an illustration of each lightpipe geometry. A summary statement of each test's results are provided in Column 5. Tier 1 (single branch lightpipe) models are shown in rows 2-5 and Tier 2 (dual/merged lightpipe) models are shown in rows 6 and 7.

| Parameter | Independent Values | Ind. Value Ranges | Visualization | Results |
|------------------------|--------------------------|---|--|--|
| Lightpipe Diameter | Diameter (mm) | 2-20 increments of 2, 20-100 increments of 20 |  | 86% with 8 mm diameter |
| Lightpipe Length | Length (mm) | 10-100 increments of 10, 100-1000 increments of 100 |  | 72% independent of length |
| Lightpipe Curve | Angle (°) Radius (mm) | 15°-90° increments of 15° 10-100 increments of 10, 100-500 increments of 100 at every angle |  | 50% max for all θ values above 100 mm radius |
| Lightpipe Double Curve | Angle (°) Radius (mm) | Same ranges holding the first curve constant at given values iterating on the second curve |  | The results are the same as the single curve above |
| Number of Lightpipes | Angle (°) Radius (mm) | 15°-90° increments of 15° 10-100 increments of 10, 100-500 increments of 100 at every angle |  | 35% max for all θ values above 200 mm radius |
| Lightpipe Spacing | Length (mm) | 20-40 increments of 5 |  | Spacing has NO effect on the transmission |

Using the revised parameter values to more accurately account for real-life optical properties resulted in lower optical transmission for most of the beta phase models, when compared to similar alpha phase models. Two key factors likely contributed to reduced

transmission: a change in viewing angle of the λ LED and a revised diameter and placement of the interrogation plane. First, the λ LED used for the alpha phase simulations (C503B-BAS/BAN/GAS/GAN, Cree) had an optical power output of 10 mW and a full viewing angle of 15°, while the λ LED used for the beta phase simulations (SMB1N-525V-02, Marubeni) had an optical power output of 230 mW and a full viewing angle of 22°. Hence, while the total power output of the beta phase λ LED was much higher, the optical output was also more diffuse, leading to decreased efficiency when propagating through the solid light guide. This was likely due to the inability to maintain total internal reflectance (TIR) within the light guide. Second, the alpha phase simulations measured radiant flux using an interrogation plane that was large (50 mm in diameter) and placed at a long distance from the exit of the light guide (50 mm) to ensure that the far-field illumination profile was measured. Transmission was calculated using the output flux from the light guide divided by the total input flux of the λ LED. By contrast, the beta phase simulations utilized a much smaller interrogation plane that matched the diameter of the endoscope illumination fiber (5 mm) and was placed at a distance similar to the illumination fiber placement when coupling the solid light guide to the endoscope (2 mm). This would alter the measurements as the former tests did not account for exiting the lightpipe/light guide and the change in refractive indices. Even though it is a 2 mm difference, the energy change could account for a change in transmission results in the beta tests. Hence, while the optical transmission values predicted by the beta phase models in Tiers 1 and 2 of testing were lower than corresponding alpha phase models, they are much closer to the actual values encountered when constructing the physical prototype.

Tier 3 testing produced 4 versions of a multi-furcated solid light guide: two symmetrical designs and two wave-shaped designs (Figure 12). The symmetrical models utilized design aspects of the alpha prototype solid light guide and would require minimal redesign of the overall spectral light source. However, the simulation results from Symmetrical Design 1 indicated that multiple merge points in the light guide reduced the transmission (Figure 12.D). Symmetrical Design 2 minimized the number of merge points to mitigate light losses (Figure 12.F). Finally, a wave-shaped light guide was designed to create one merging point and manipulate the light in the same direction for every branch. The wave-shape was created in two configurations: Wave Design 1 with spacing between branches created by adding straight lengths of lightpipe between curves (Figure 12.H) and Wave Design 2 with increasing arc radius for each branch (Figure 12.I). For all Tier 3 beta phase simulations, the optical power was measured at each branch point in order to assess the source of optical transmission losses throughout the light guide.

Results from Symmetrical Design 1 (Figure 12.A-D), with 2, 4, 8 or 16 branches, demonstrate that doubling the number of merge points reduces the transmission by ~50% (Figure 14.A). Only the 2 and 4 branch models met the optical performance requirements of $\geq 10\%$ transmission. However, this 4-branch model would provide an insufficient number of wavelengths to acquire a spectral image stack. To investigate the effects of reducing the number of merge points while maintaining the number of branches, Symmetrical Design 2 was developed (Figure 12.E-F), which featured either 4 or 16 branches, but with merge points located in close proximity and with some of the branches passing straight into the merge point instead of along an arc. However, generating one larger merge point instead of 2 separate merge points provided reduced transmission for

many of the branches (Figure 14.B). The reduced performance is likely due to the complex geometry formed when multiple branches merge in close proximity and likely to the presence of straight branches, leading to ray-substrate angles outside of the critical angle. To further investigate the utility of using an arc geometry and maintaining tangent criteria at merge points, an additional set of wave-shaped light guides were developed (Figure 12.G-I). Wave Design 1 was created to maintain the same direction of curvature for either 8 (Figure 12.G) or 16 (Figure 12.H) branches. Model results (Figure 14.C) indicated an increase in transmission, but also a wide variability in transmission from branch to branch (between 0-30% for the 16-branch version). To further improve transmission, Wave Design 2 was created using parabolic geometry for the curved branches (Figure 12.I). Results (Figure 14.D) demonstrated a range of optical transmission between 4-20%, depending on the branch. However, by coupling high power output λ LEDs to low transmission branches and low power output λ LEDs to high transmission branches, it is possible to meet the specified power of 10 mW per branch.

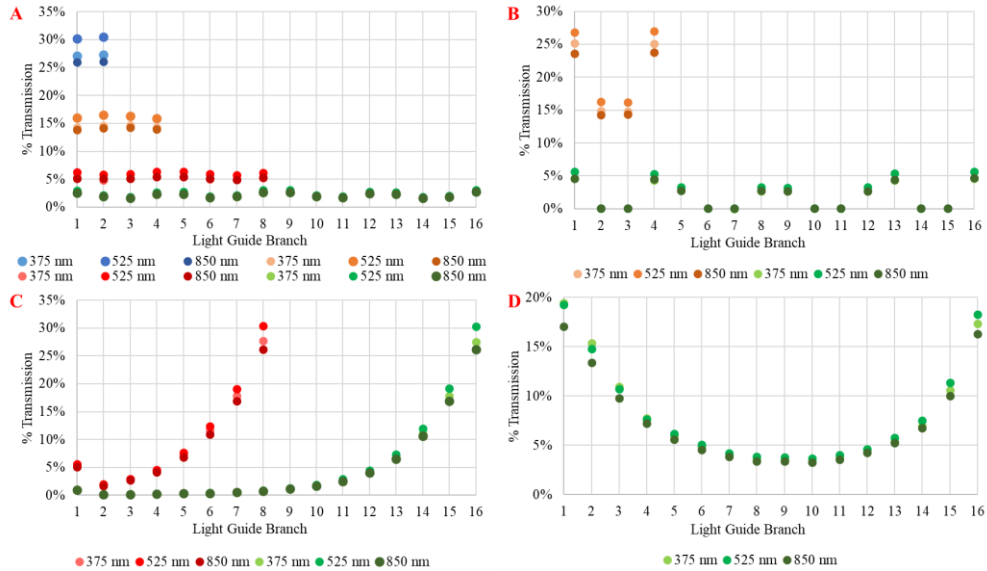


Figure 14. Results of the ray tracing simulations for the beta light guide models showing optical transmission as a function of % transmission vs. branch illuminated. (A) Results of the Symmetrical Design 1 (Figure 12.A-D) transmitting LED light per branch for a 2 (blue), 4 (orange), 8 (red) and 16 (green) branch model over the range of LEDs. A UV, visible and IR LED was graphed to show any throughput changes as a result of wavelengths. (B) Results of Symmetrical Design 2 transmitting (Figure 12.E-F) LED light per branch for a 4 and 16 branch model over the range of LEDs. (C) Results of the Wave Design 1 (Figure 12.G-H) transmitting LED light per branch for an 8 and 16 branch model over the range of LEDs. (D) Results of Wave Design 2 (Figure 12.I) transmitting LED light per branch for a 16-branch model over the range of LEDs.

Comparison of ray trace to requirements – The overall goal of this work was to

develop a novel geometry of multifurcated optical light guide that could meet the requirements of 10 mW of power per branch, create a flat spectral response and produce an illumination beam with similar numerical aperture to the endoscope fiber bundle.

While initial feasibility of the approach was demonstrated using the alpha phase modeling and prototyping efforts, benchtop testing revealed that further work was needed to meet the illumination power requirements in order to achieve quality SNR endoscopic image data at video-rate acquisition. The beta phase modeling efforts were then performed, with results indicating that a 16-branch geometry, Wave Design 2 (Figure 12.I) could provide between 4-20% optical transmission (Figure 14.D), depending on

branch. To demonstrate the theoretical feasibility of this revised geometry for achieving spectral illumination, a λ LED and light guide combination was modeled that coupled high power output λ LEDs (see Table 4 and Figure 15.A for λ LED power and transmission requirements) to low transmission branches of Wave Design 2 and low power output λ LEDs to high transmission branches of Wave Design 2, simulating the spectral output to the endoscope (Figure 15).

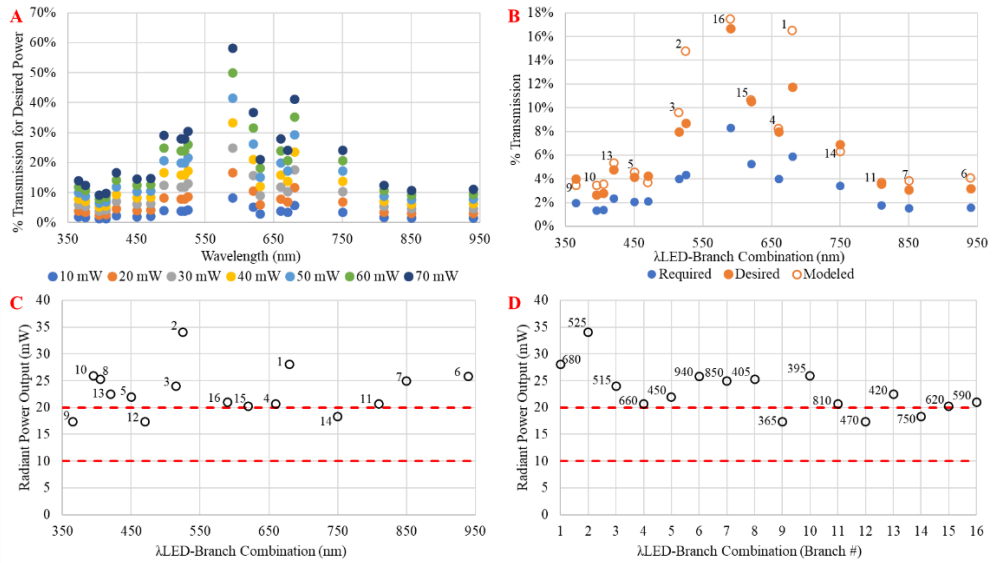


Figure 15. Comparison of the required outputs of each λ LED to the theoretical output of the simulation model Wave Design 2 in Figure 12.I. (A) The % transmission per λ LED needed to achieve a set power output from Table 4. (B) The data for wavelength transmission of 10 mW (Required – shown as solid blue circles) and 20 mW (Desired – solid orange circles) from panel A compared to the transmission of the λ LED-branch combination determined using the results of the Wave Design 2 light guide seen in Figure 12.I (Modeled – open orange circles). Branch #'s which each LED should be coupled with are labeled above each open, orange data point. A reduced number of wavelengths (from 21 available and reduced to 16 positions of the multifurcated light guide) was selected to allow a range of comparable excitation wavelengths observed in literature. (C) Conversion of panel B to expected radiant power output through the Wave Design 2 in Figure 12.I with branches labeled above each wavelength (x-axis) data point. The 10 mW required and 20 mW desired levels are denoted with dashed red lines. (D) The data from panel D reorganized in the linear branch order (x-axis) of the multifurcated light guide while the labels represent the wavelength of each branch. Dashed red lines remain for the 10 mW and 20 mW thresholds.

Results from specific λ LED-branch combinations of the optical raytrace model simulation indicate that it is possible to achieve the required 10 mW (and higher to the desired 20 mW) of power per λ LED based on the transmission efficiency (Figure 15.B) and the conversion to expected power outputs (Figure 15.C-D). The comparison shows the model has 3 λ LED-branch combinations that are less than the desired 20 mW optical power output. As seen in

Table 7 the λ LED array would not be in increasing wavelength order, but this is inconsequential as the λ LEDs can be illuminated in any order specified through the use of the corresponding TTL control signals.

The proof-of-concept λ LED-based spectral endoscopic system (Figure 11), which produced an irradiance output maximum of 2.6 mW of power (of the 670 nm λ LED seen in Figure 13.B,D), acquired a reflectance image stack (Figure 13.E) in 1.2 s and a fluorescence image stack (Figure 13.F) in 30 s. The simulation data for an optimized solution of the multifurcated solid light guide illustrates the Wave Design 2 (seen in Figure 12.I) with the right λ LED-branch coupling could potentially provide an average of 20 mW irradiance power to the endoscope. Assuming loss through the endoscope to an extreme of 15 mW irradiance at the output of the endoscope still meets the required output of 10 mW and would have at least 5X more illumination than the current physical prototype. This irradiance increase infers that the acquisition time for an image stack (reflectance, fluorescence or a mixture) should decrease to speeds for video-rate hyperspectral endoscopy.

Table 7. Tabulated data from Figure 15 comparing the required (Column 2) and desired (Column 3) transmission of each λ LED (from Table 4) to the simulated (Column 4) transmission results (also plotted in Figure 14.D). The corresponding radiant power potential (mW) for each λ LED (Column 5) and the amount of power over or under (\pm) the 10 mW required and 20 mW desired thresholds were also assessed (Column 6). λ LED and corresponding multifurcated light guide branch number combinations can be seen by comparing Columns 1 and 7.

| LED (nm) | Required (10mW) Transmission | Desired (20mW) Transmission | Modeled Transmission | Radiant Power Output (mW) | (\pm to 10mW/ \pm to 20mW) | Corresponding Branch |
|----------|------------------------------|-----------------------------|----------------------|---------------------------|------------------------------------|----------------------|
| 365 | 2% | 4% | 3.5% | 17.3 | (+7.3/-2.7) | 9 |
| 395 | 1% | 3% | 3.5% | 25.9 | (+15.9/+5.9) | 10 |
| 405 | 1% | 3% | 3.6% | 25.3 | (+15.3/+5.3) | 8 |
| 420 | 2% | 5% | 5.4% | 22.5 | (+12.5/+2.5) | 13 |
| 450 | 2% | 4% | 4.6% | 21.9 | (+11.9/+1.9) | 5 |
| 470 | 2% | 4% | 3.7% | 17.3 | (+7.3/-2.7) | 12 |
| 515 | 4% | 8% | 9.6% | 24.0 | (+14.0/+4.0) | 3 |
| 525 | 4% | 9% | 14.8% | 34.0 | (+24.0/+14.0) | 2 |
| 590 | 8% | 17% | 17.5% | 21.0 | (+11.0/+1.0) | 16 |
| 620 | 5% | 11% | 10.7% | 20.2 | (+10.2/+0.2) | 15 |
| 660 | 4% | 8% | 8.3% | 20.6 | (+10.6/+0.6) | 4 |
| 680 | 6% | 12% | 16.5% | 28.0 | (+18.0/+8.0) | 1 |
| 750 | 3% | 7% | 6.3% | 18.3 | (+8.3/-1.7) | 14 |
| 810 | 2% | 4% | 3.7% | 20.6 | (+10.6/+0.6) | 11 |
| 850 | 2% | 3% | 3.8% | 25.0 | (+15.0/+5.0) | 7 |
| 940 | 2% | 3% | 4.1% | 25.8 | (+15.8/+5.8) | 6 |

Future work

Multifurcated solid light guides, coupled to discrete wavelength LEDs (λ LEDs) represent a novel approach for providing spectral illumination with high switching speeds. In this work, we have shown the feasibility of using this novel approach through alpha model simulations and prototyping, followed by verification through benchtop testing. Furthermore, the results of physical testing provided insight for optimization and the subsequent beta model simulations. Future work will focus on prototype development of the final optimized light guide geometry (Figure 12.I), benchtop testing and endoscope integration. Additional system variations will also be investigated, such as the use of coupling lenses for λ LED collimation prior to light guide coupling, manipulation of the

light guide entrance geometry for improved TIR and techniques for light guide-endoscope coupling to match numerical aperture requirements. Endoscope testing will focus on feasibility demonstration in excised tissues and *in vivo* animal models with a long-term goal to transition the technology to a clinical platform for clinical pilot testing. If successful, this technology may represent the next step in developing endoscope systems with enhanced contrast for clinical screening.

Funding

The authors would like to acknowledge support from the NASA/Alabama Space Grant Consortium, NASA Grant award #NNX15AJ18H, NSF grant award 1725937, NIH grant awards UL1 TR001417, P01 HL066299, the Abraham Mitchell Cancer Research Fund, the University of Alabama at Birmingham Center for Clinical and Translational Science (CCTS), and the Economic Development Partnership of Alabama.

Acknowledgements

Optical design support was provided by Lambda Research Corp., TracePro Expert non-profit thesis version. Optical design support and fabrication was provided by Apollo Optical Systems, Inc.

Disclosures

The corresponding author, Dr. Leavesley, is named as an inventor on a patent (US patent no. 10,393,964 B2) issued to the University of South Alabama for the novel design of the multibranch optical light guide (P). Drs. Leavesley and Rich disclose financial interest in a start-up company, SpectraCyte LLC, founded to commercialize spectral imaging technologies (I).

References

The reference section for this manuscript has been combined in the dissertation reference section.

CHAPTER V: MICROSCOPY IS BETTER IN COLOR: DEVELOPMENT OF A STREAMLINED SPECTRAL LIGHT PATH FOR REAL-TIME MULTIPLEX FLUORESCENCE MICROSCOPY

This chapter shows feasibility testing of another LED-based spectral illuminator on a microscope platform. This manuscript has been peer reviewed and published in Optica Publishing Group's Biomedical Optics Express journal.

Browning, C.M., Mayes, S., Mayes, S.A., Rich, T.C., and Leavesley, S.J.,
"Microscopy is better in color: development of a streamlined spectral light path for real-time multiplex fluorescence microscopy," Biomedical Optics Express 13(7), 3751 (2022).

© 2021 Optical Society of America under the terms of the [OSA Open Access Publishing Agreement](#)

Abstract

Spectroscopic image data has provided molecular discrimination for numerous fields including: remote sensing, food safety and biomedical imaging. Despite the various technologies for acquiring spectral data, there remains a trade-off when acquiring data. Typically, spectral imaging either requires long acquisition times to collect an image stack with high spectral specificity or acquisition times are shortened at the expense of fewer spectral bands or reduced spatial sampling. Hence, new spectral imaging

microscope platforms are needed to help mitigate these limitations. Fluorescence excitation-scanning spectral imaging is one such new technology, which allows more of the emitted signal to be detected than comparable emission-scanning spectral imaging systems. Here, we have developed a new optical geometry that provides spectral illumination for use in excitation-scanning spectral imaging microscope systems. This was accomplished using a wavelength-specific LED array to acquire spectral image data. Feasibility of the LED-based spectral illuminator was evaluated through simulation and benchtop testing and assessment of imaging performance when integrated with a widefield fluorescence microscope. Ray tracing simulations (TracePro) were used to determine optimal optical component selection and geometry. Spectral imaging feasibility was evaluated using a series of 6-label fluorescent slides. The LED-based system response was compared to a previously tested thin-film tunable filter (TFTF)-based system. Spectral unmixing successfully discriminated all fluorescent components in spectral image data acquired from both the LED and TFTF systems. Therefore, the LED-based spectral illuminator provided spectral image data sets with comparable information content so as to allow identification of each fluorescent component. These results provide proof-of-principle demonstration of the ability to combine output from many discrete wavelength LED sources using a double-mirror (Cassegrain style) optical configuration that can be further modified to allow for high speed, video-rate spectral image acquisition. Real-time spectral fluorescence microscopy would allow monitoring of rapid cell signaling processes (i.e., Ca^{2+} and other second messenger signaling) and has potential to be translated to clinical imaging platforms.

Introduction

Spectral imaging technologies have provided target detection and molecular analysis capabilities for a wide range of fields, including remote sensing^{13,181,182}, agriculture¹⁸³, food safety^{15,40,184,185}, historical document preservation^{41,42}, biological research^{186,187}, and clinical imaging^{17,188–190}. In the field of fluorescence microscopy, spectral imaging approaches have provided molecular detection capabilities that allow more accurate quantification of stains and fluorescent proteins^{191–195}, separation of competing signals^{196,197}, and characterization and analysis of cell and tissue autofluorescence^{187,198–200}. Spectral imaging capabilities have been incorporated into several commercial confocal microscope systems, as well as widefield fluorescence microscope modules.

Specific technologies used to enable spectral imaging include filter wheels, tunable filters, dispersive optics, Fourier transform optics, and others that have been summarized elsewhere^{201,186,202,163,44}. Spectral imaging technologies can be divided into two general groups: spectrally and spatially dynamic. Spectrally dynamic optics include tunable filters and filter wheels that mechanically rotate or switch filters to achieve spectral filtering. For example, filter wheel-based hyperspectral imaging systems have been previously utilized for widefield fluorescence microscopy applications, albeit with limited temporal sampling rates^{203,204}, while we and others have previously demonstrated the utility of mechanically rotated thin-film tunable filters (TTFs) for widefield fluorescence microscopy, again with limited temporal sampling capabilities^{174,205}. Spatially dynamic optics include dispersive optics, acousto-optical tunable filters (AOTF), liquid crystal tunable filters (LCTF)²⁰⁶ and interferometry-Fourier transform

optics²⁰⁷. Commercial hyperspectral confocal microscope systems have been designed with spectral detectors that filter fluorescence emission using a grating and PMT array^{208,209}, while prism-based systems have been utilized for hyperspectral widefield microscope systems^{210,211}. Alternatively, self-contained spectral cameras that utilize dispersive optics (such as from SPECIM and others) have also been used to acquire spectroscopic data, such as for laparoscopic applications⁴⁷. Recent studies have demonstrated that HSI systems can be developed using both AOTFs²¹² and LCTFs²¹³ and can achieve relatively fast image capture speeds, albeit with limitations due to polarization and other tuning and beam steering requirements. LCTF-based systems have also been evaluated for clinical endoscopy applications using reflected light²¹⁴. Spectral imaging microscope systems have also been implemented using supercontinuum lasers to provide spectral illumination. Broadband supercontinuum laser sources require additional optics, such as AOTFs or gratings, in order to provide spectral discrimination. Poudel et al (2018) provides an excellent review on the various supercontinuum configurations evaluated to date²¹⁵. LED sources have also been utilized, both as high-power broadband, white light sources to replace arc lamps^{216,217} and as multi-channel illumination sources, where four LED channels may be rapidly switched for multispectral fluorescence microscopy²¹⁸.

Interestingly, despite the many and diverse technologies used to acquire fluorescence microscope spectral image data, most approaches share common trade-offs^{219,220}. Filter-based optics (such as filter wheels) for spectral imaging are typically mechanically limited and difficult to utilize for high-speed acquisition. To date, some of the fastest filter wheel modules can change between adjacent filter positions in

approximately 20 ms, for a filter wheel with 6 positions²²¹. It is possible that a spectral microscope system could be designed utilizing multiple filter wheel modules that are stacked, if each module contains a blank position that allows for selection of filters from adjacent modules. However, at best, spectral acquisition rates would still be limited by filter switch times and such a system would become complex if many wavelength bands were required, as multiple filter wheel modules would need to be stacked in serial. In addition, this approach could produce potential vibration artifact from the multiple moving components, and the system lifecycle that would be tied to mechanical wear. Fixed filters have been alternatively utilized in snapshot spectral imaging systems that can provide rapid acquisition speeds, but these typically require a compromise between the number of wavelength bands acquired (spectral sampling) and spatial sampling [38,39]. Dispersion-based systems may be able to achieve high-speed spectral imaging, but typically have a reduced photon budget due to the additional optics and slits employed, as well as fluorescence emission distributed onto many detector elements^{201,215}. Current LED-based systems are limited by the number of LED channels available or mechanical movement required to cycle through multiple banks LEDs²¹⁸. However, the trend in cellular signaling experiments is continuing to move towards complex, multi-function intracellular and intercellular dynamics for live cell imaging (i.e., the multiple utilities of Ca²⁺ signaling)²²². Hence, there is a need for spectral imaging technologies that enable both high speed and high sensitivity in order to discriminate multiple components. Further driving this need is that many biomedical hyperspectral imaging studies are increasingly moving towards multi-label (5+) quantitative discrimination in performing spectroscopic analysis, promoting the need for

increased spectral scan range with fast acquisition times^{223,224,147,225}. These needs can be fulfilled when imaging bright specimens or specimens that are photostable and not rapidly changing. However, for rapid cell signaling experiments, especially those involving fluorescent protein-based labels, the specimen is often both dynamically changing and photosensitive. Hence, it is important to capture emitted photons as efficiently as possible, with both high sensitivity and speed.

We have previously demonstrated that scanning of the fluorescence excitation spectrum (excitation-scanning) may offer an alternative approach for spectral imaging fluorescence microscopy, while providing greatly increased (>10X) signal strength when compared to emission scanning when using identical illumination intensity^{174,226}. Initial feasibility of this approach was demonstrated in a side-by-side comparison that utilized an array of thin-film tunable filters (TFTFs). While this implementation demonstrated feasibility for excitation-scanning spectral imaging, delays associated with mechanical rotation of TFTFs resulted in delays of 100-250 ms when switching between wavelength bands, resulting in acquisition times that were insufficient for rapid time-lapse cell signaling assays.

Here, we present initial results from an alternative technology for implementing excitation-scanning spectral imaging using an array of wavelength-dependent light emitting diodes (LEDs) that allow rapid wavelength switching. A novel hyperspectral optical geometry was developed that uses a pair of reflecting mirrors, similar to a Cassegrain telescope design, to combine optical output from the LEDs into a single liquid light guide for coupling into a fluorescence microscope. Bench-testing and imaging

results indicate that this approach may be suitable for a range of experimental assays that can be performed on a widefield microscope base.

Methods

Optical ray trace modeling was used to simulate the theoretical performance of the LED-based spectral illuminator and to optimize the optical and geometric configuration. Prototyping and benchtop testing were then performed, based on the optimal design indicated by ray trace simulations. Finally, the spectral illuminator was integrated with a widefield fluorescence microscope and image performance was compared to our prior excitation-scanning spectral microscope system^{174,205}.

Ray trace simulations

Optical ray trace simulations were conducted using TracePro software (Lambda Research Corp.). A range of simulations were performed to select optical components and specify geometry in order to optimize transmission through the spectral illuminator²²⁷. An overall optical geometry was implemented that utilized two mirrors to direct light from all LEDs to a common entrance aperture of a liquid light guide. The design was similar to a Cassegrain telescope, but utilizing a concave mirror and a flat mirror (Figure 16). To allow for many wavelengths of illumination, LEDs were arranged in a concentric pattern around the flat mirror and focused using a lens.

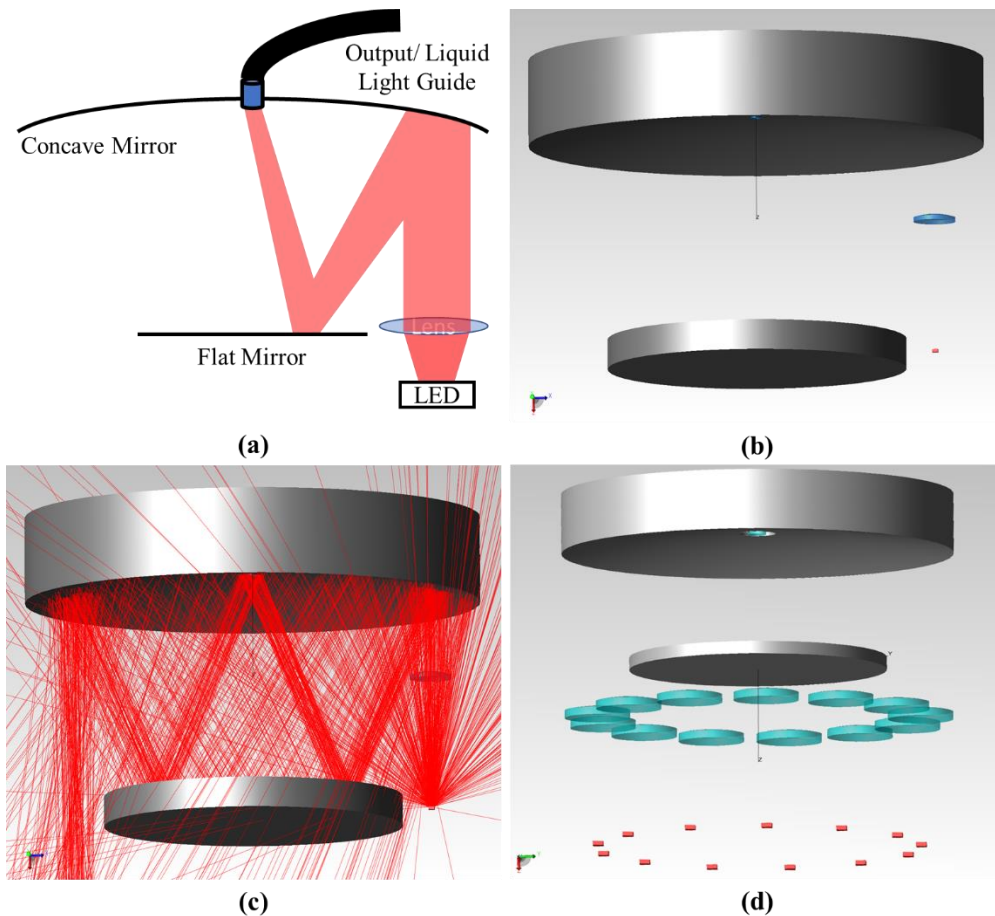


Figure 16. Conceptual illustration for the spectral illuminator to combine optical output from multiple wavelength-specific LEDs located in a ring and reflected to a common location. (a) The drawing here only presents one LED for clear optical pathways. Renderings of the spectral illuminator optical components as simulated in TracePro optical ray trace software for (b) identical layout as the concept drawing and representative depiction of the optical components (mirrors-silver, lenses-blue and LED-red) used in simulations. (c) Displays an example of the ray trace results for a single LED and lens location (0.5% of rays shown for visualization purposes). (d) A rendering of all optical components able to fit this version of the simulated spectral illuminator.

Monte Carlo-based ray tracing was performed using 100,000 rays per simulation. This number was determined to be sufficient to achieve a repeatable result when multiple ray traces were conducted of the same model. LED illuminators were simulated by importing optical specifications from manufacturer data sheets (SMB1N series, Marubeni Co.). The radiance and spectral profile were extracted for each LED model and uploaded

to the TracePro Surface Source Properties library. Lens and mirror models were imported from manufacturer-supplied Zemax files (Edmund Optics). A range of lens focal lengths (FL) and mirror diameters (D) were evaluated (Table 8) that included three different diameter mirrors and a single lens.

Table 8. Optical components used for ray trace simulations. Simulations were performed using three different diameter mirrors (columns 2-4), where the focal length (FL) and diameter (D) of each mirror is indicated in the column header. For each mirror, a range of focal length lenses were evaluated using either a single lens or dual lens optical path. All lenses were evaluated at a 15 mm diameter, with the exception of the 12 mm focal length lens, which was evaluated at a 12 mm diameter.

| Mirror | Concave FL/D, Flat D | 76.2 mm/76.2 mm, 50 mm | 114.3 mm/114.3 mm, 75 mm | 152.4/152.4 mm, 100 mm |
|--------|-------------------------|---|-----------------------------------|-----------------------------------|
| Lens | FL | 12 mm 30 mm 45 mm 60 mm 75 mm 100 mm | 45 mm 60 mm 75 mm 100 mm | 45 mm 60 mm 75 mm 100 mm |

All simulations were implemented using custom macro scripts within TracePro to allow evaluation of a range of geometric locations and orientations for each component. In summary, the macro first defined the properties, location, and orientation of the two mirrors, next created a 5 mm detector at the center of the concave mirror to simulate the liquid light guide (LLG) entrance aperture, then defined LED source properties (525 nm), location, and orientation, and finally defined lens properties, orientation and location. A parametric sensitivity study was performed by changing the location of lenses and LEDs in the vertical and horizontal axes while performing a ray trace simulation for each location and measuring simulated optical power (irradiance) upon the LLG entrance

aperture (Figure 16.b,c). Lens positions were varied in 1 mm increments, while LED positions were varied in 10 mm increments, as defined in a nested loop macro (example simulation loops of the model are illustrated in Visualization 1). These data were used to determine optical component selection and placement in order to provide optimal output of the spectral illuminator.

Prototype fabrication

A prototype spectral illuminator was constructed using the optimal components and geometric spacing identified through optical ray trace modeling. The prototype consisted of 13 wavelength-specific LEDs (SMB1N Series, Roithner Lasertechnik GmbH, specifications in

Table A1 of Appendix B: Supplemental Document), 44.5 mm FL x 12.7 mm diameter plano-convex lenses (49-860, Edmund Optics), and a 75 mm diameter mirror (CM750-075-F01, Thorlabs) customized to include a 7 mm center through hole. Optical components were mounted in a series of custom cage plates fabricated by Thorlabs. In addition, XY linear translation mounts were used to allow fine tuning of LEDs, focusing lenses, concave mirror, and flat mirror to test alignment sensitivity.

Custom printed circuit boards (PCB) were designed using Pad2Pad software (Pad2Pad Inc.) for surface mount LEDs (LED board) and for routing signals from the computer interface boards to a series of LED current drivers (current driver board). Digital and analog controls were provided through NI 6363 and NI 6723 cards (National Instruments, Inc.), respectively. Digital signals were used to switch current drivers (RCD-24-1.20, RECOM) on and off rapidly, while analog signals were used as a reference voltage to regulate the current output of each LED driver, and hence LED power output.

Benchtop characterization

Benchtop testing consisted of determining optical power transmission and optimal spacing of components. Spectral irradiance was measured using a fiber-coupled spectrometer (QE65000, Ocean Optics) and integrating sphere (4P-GPS-030-SF, Labsphere) calibrated to a NIST-traceable light source (LS-1-CAL, Ocean Optics). All measurements were acquired by averaging 10 scans (resulting standard deviation of measurements is ± 0.002 mW). Irradiance was used to align the optical components and allow comparison with simulation data. To determine the optimal position for components, four LEDs were utilized that represented four extreme locations on the circular LED array (e.g., N, S, E, and W). An additional LED was added to ensure sampling of wavelengths throughout the target spectral range (365 nm, 395 nm, 430 nm, 450 nm and 525 nm). These five LEDs were illuminated simultaneously and the total power output was measured at the distal end (output) of the LLG (O777655⁸ series 300, Lumatec GmbH), while optical component positions were adjusted. The final position for each component was determined so as to achieve a maximal total power output while also ensuring that each wavelength-specific LED contributed approximately equal to the spectral power distribution. Upon selecting optimal component locations, the LLG was connected to a TE-2000 inverted fluorescence microscope (Nikon Instruments, Inc., Table 9) and the irradiance was assessed at the microscope stage. The optical power output, as a function of current driver setting, was characterized for each LED, thus allowing a power output look-up table to be constructed for each excitation wavelength. In addition, to allow a comparison of ray trace simulation results, a new set of simulation models were formed to replicate the prototype positioning and wavelength illumination.

The revised ray trace simulations were performed at each optical component spacing as was evaluated for the prototype, mentioned above. Irradiance was measured at the interrogation surface of the model (i.e., the simulated entrance to the liquid light guide). Irradiance measurements of the prototype (prior to coupling with the fluorescence microscope) were compared to simulated irradiance of ray trace model for validation. In summary, the prototype optical irradiance was measured at the distal end of a coupled LLG and the simulation was measured at an interrogation plane that represented the entrance or proximal end of a LLG but did not account for acceptance angle effects of the LLG or transmission losses through the LLG.

Spectral imaging feasibility tests

To assess the feasibility of LED-based excitation-scanning spectral imaging, the prototype system was compared to our previously-reported excitation-scanning spectral imaging system that utilizes an array of thin-film tunable filters, or TFTFs (VersaChrome, Semrock) mounted in a custom mechanical tuning device (VF-5, Sutter Instrument Co.)^{174,205}. Both systems were implemented in succession using the same TE-2000 inverted microscope base (Figure 17), equipped identically for each trial (Table 9). Image acquisition speed for each system was selected so as to fill as much of the dynamic range of the detector as possible at weak (low illumination power) spectral bands while avoiding oversaturation of strong (high illumination power) spectral bands.

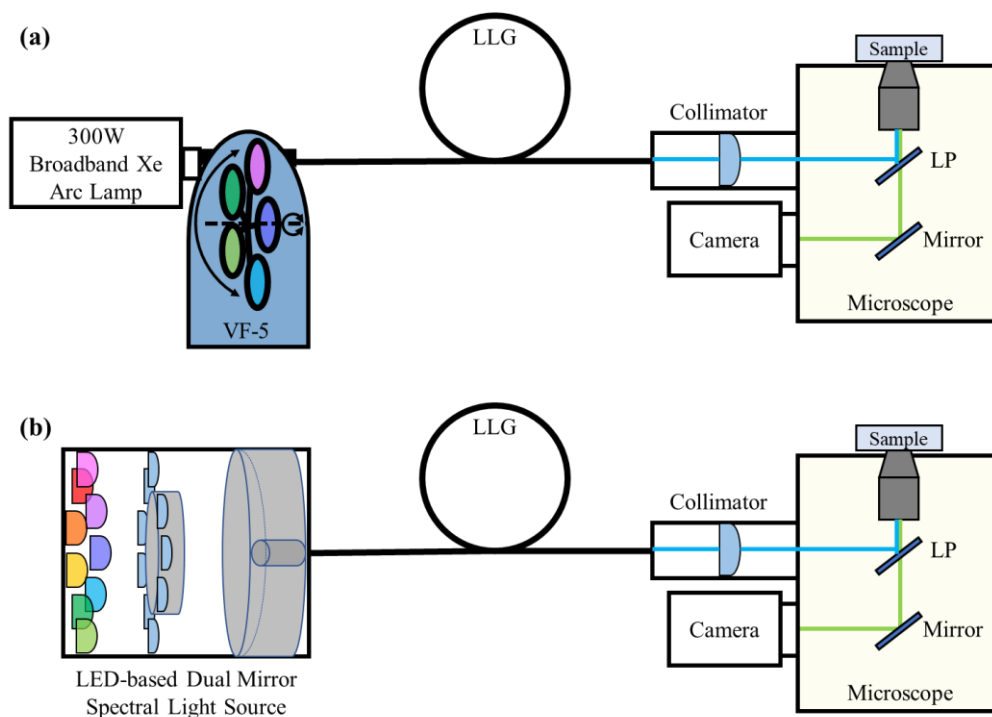


Figure 17. Light path schematics for the two spectral illumination pathways used in hyperspectral image acquisition: (a) TFTF-based illumination using mechanical tuning (both rotationally about the axis and perpendicular to the axis) implemented in a Sutter, VF-5 tuning system and (b) LED-based illumination using electronic switching of the custom wavelength-specific LED array. Both illumination sources were transmitted via liquid light guide (LLG) to a collimator on the back side of the widefield fluorescence microscope. The collimated beam was reflected off the dichroic long-pass (LP) filter to the sample. Fluorescence emission above the cutoff wavelength was transmitted through the dichroic LP filter and reflected to the camera detector for acquisition.

Table 9. Two microscope platform configurations including the components and parameters used for imaging.

| | TFTF-based System | LED-based System |
|--|---|--|
| Light Source | Xe Arc Lamp | SMB1N LEDs |
| Excitation | Filters: 360-545 nm, 5 nm intervals | LEDs: 365, 375, 385, 395, 405, 415, 420, 430, 450, 470, 490, 515, 525 nm |
| Dichroic | 555 nm LP | 555 nm LP |
| Emission | - | - |
| Objective Magnification Numerical Aperture | Nikon 60X WI Plan Apo 1.2 NA | Nikon 60X WI Plan Apo 1.2 NA |
| Detector Acquisition Speed Bit Depth Binning | Photometrics Prime 95B 50 ms 12-bit 2x2 | Photometrics Prime 95B 500 ms 12-bit 2x2 |

Test samples were prepared by Abberior, GmbH, and consisted of African green monkey kidney epithelial cells that were labeled using a custom 6-label scheme (Table 10), as well as corresponding single-label and unlabeled slides to serve as controls for building a spectral library. Cells were fixed and stained according to Wurm, et al.²²⁸ and were embedded in Abberior Mount Solid Antifade.

Table 10. Cellular components labeled and the corresponding fluorescent label for six-labeled slides used for spectral imaging feasibility testing.

| Cellular Component | Fluorescent Label |
|-----------------------------|--|
| Nuclear Pore Protein (NPP) | Abberior STAR 440SXP goat anti-mouse IgG |
| F-Actin | Abberior STAR GREEN phalloidin |
| Mitochondria | Abberior STAR 520SXP goat anti-rabbit IgG |
| double stranded DNA (dsDNA) | Abberior LIVE 560 DNA |
| Vimentin | Abberior STAR ORANGE goat anti-chicken IgY |
| Golgi Apparatus | Abberior STAR RED goat anti-guinea pig IgG |

Image data were acquired in the following order: 1) single-label control slides were imaged using the TFTF system, 2) the six-label slide was imaged and the XY microscope stage coordinates recorded, 3) the identical field of view, with identical XY coordinates, was imaged using the prototype LED-based system, and 4) single-label control slides were imaged using the LED-based system. Spectral images were acquired sequentially from shortest to longest wavelength in each system with only one wavelength illuminated at a time. This was achieved in the TFTF system by rotating and switching TFTF filters, while in the LED system by sequentially switching LED wavelengths on or off. This approach ensured that a side-by-side comparison of both systems was possible using the same field of view and identical microscope and camera settings with the exception of image acquisition times.

Results

Results from this study are organized in four subsections – optical ray trace simulations to assess early feasibility and to optimize component selection and geometry *in silico*, prototype development, benchtop irradiance testing to compare and validate physical and theoretical system performance, and feasibility image testing to assess potential for use in an integrated epifluorescence microscope system.

Ray trace simulations

Optical ray trace simulations were performed to evaluate the theoretical feasibility of the optical configuration prior to prototyping. Simulations consisted of modeling the components in the light path of the spectral illuminator, including the LED, lens, concave mirror, flat mirror and interrogation plane at the center of the concave mirror (representing the input aperture of the LLG). These tests were used to determine optimal lens and concave mirror parameters and location. Typical results consisted of irradiance output for the simulated single lens options at every position tested (example of how the data trends with the positioning of the LED and lens are shown in Visualization 1). The maximum optical transmission was achieved for each lens when the LED-lens spacing was equal to the lens FL. A sample-set of the data and summary graphs to present a synopsis of the entire one lens configuration simulation dataset is provided as Figure A3 in Appendix B: Supplemental Document .

Transmission was measured as the integrated irradiance captured at the simulated LLG entrance aperture divided by the irradiance produced by the simulated LED. The values shown below (Table 11) summarize the model results by reporting the average maximum output for each lens configuration when a similar maximum value was

achieved regardless of lens-LED spacing (this trend is depicted in the right column of Figure A3).

Table 11. Transmission maximums for each lens configuration using the three different diameter mirrors. The optimal combinations are highlighted by the boldened percent transmission

| Mirror | Concave FL/D, Flat D | 76.2 mm/76.2 mm, 50 mm | 114.3 mm/114.3 mm, 75 mm | 152.4/152.4 mm, 100 mm |
|---------|-------------------------|---------------------------|-----------------------------|---------------------------|
| Lens FL | 12 mm | 2.50% | | |
| | 30 mm | 8.03% | | |
| | 45 mm | 11.39% | | |
| | 60 mm | 6.74% | 5.89% | 3.72% |
| | 75 mm | 5.55% | 6.53% | 3.64% |
| | 100 mm | 3.08% | 5.92% | 3.21% |
| | | | 3.73% | 1.93% |

Simulation results indicated an inverse relationship between concave mirror FL and efficiency (optical transmission) where a 76.2 mm FL mirror averaged 11% transmission, a 114.3 mm FL mirror, 6.5% transmission and a 152.4 mm FL mirror averaged ~4% transmission. However, it should be noted that simulated optical transmission was calculated solely on optical power incident on the interrogation plane, which was used to simulate the entrance aperture of the LLG, regardless of incident light angle. Hence, simulation results did not account for angle-dependent losses that could be encountered during optical coupling with the LLG. Among the six focal length lenses evaluated, the 45 mm lens provided the highest optical efficiency, with 11% optical transmission for the 76.2 mm FL mirror.

Upon reviewing all model simulation results, a lens configuration using the 76.2 mm focal length mirror and 45 mm focal length lens was selected for prototyping. This configuration was simulated to achieve 11% optical transmission to the entrance aperture

of the LLG, which corresponds to approximately 100 mW of available optical power, depending on wavelength, that can be coupled into the LLG.

Prototype fabrication

A 3” cage system was utilized to encapsulate and align all optical components. Custom cage plates were machined to house the two mirrors, the lens array, and the LED array (Figure 18.a,b). Due to limitations in packing density of lenses in the lens array, the prototype was designed to house 13 lenses, and hence 13 LEDs with corresponding peak wavelengths. A custom PCB was utilized to align surface mount LEDs with respective lenses. The lenses and LEDs were placed radially equidistant in a circular pattern of diameter of 63.5 mm. A second custom PCB was printed to connect individual analog and digital lines from the computer interface board to a respective current driver for each LED. Hence, separate analog power output and digital on/off control was provided for each LED. TTL triggering was utilized to synchronize LED wavelength switching with the camera acquisition. LED intensities (mW) were measured at reference voltage intervals of 0.5V from 4V to ~2V (within 95% of the maximum forward current allowed) using the spectrometer detailed above. The voltage drop across the 1 Ω resistor was used to calculate the current supplied to the LED. The relationship between the reference voltage supplied, the current driver output, and the corresponding LED radiant flux was linear (see Figure A4 of Appendix B: Supplemental Document). Cage plates were mounted on XY translational stages for precise alignment measurements when validating the optics positioning (Figure 18.c).

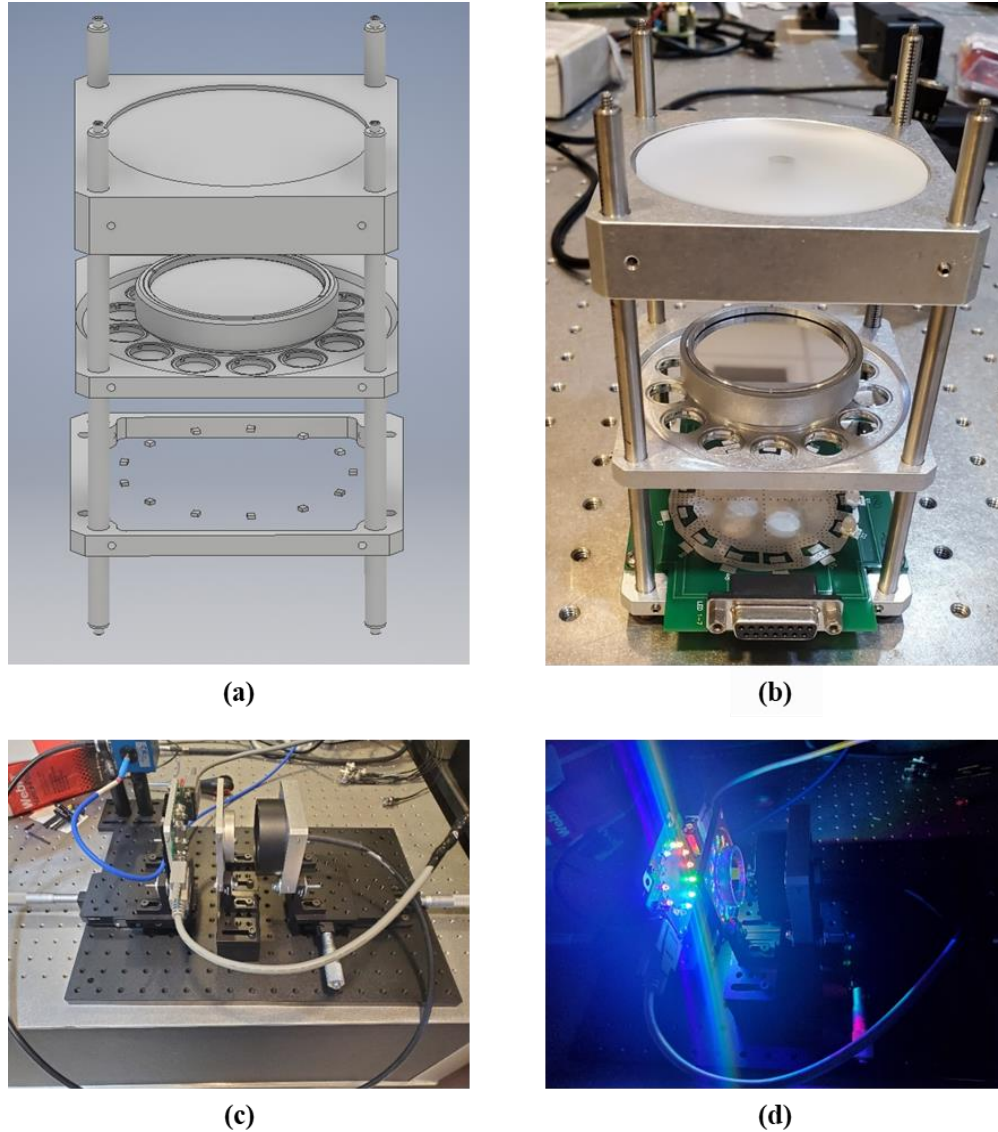


Figure 18. Fabrication of the dual mirror spectral illuminator prototype. (a) A CAD rendering of the custom cage plates, (b) assembly of the custom cage with LED circuitry and optical components. (c) Custom cage plates mounted to linear translation stages to assess alignment sensitivity during benchtop irradiance testing. (d) Example photograph of the spectral LED array with all wavelengths illuminated for demonstration purposes.

Benchtop characterization

The alignment process consisted of two steps: 1) alignment to produce the highest radiant power output for a selected wavelength LED as measured at the output of the LLG, and 2) alignment to compromise between the power output of all wavelengths so as

to produce a spectrally balanced illuminator (i.e., similar optical power output across all wavelength bands). In some cases, a trade-off was required between achieving maximal power of a single LED and achieving balanced spectral power output. Once positioned, results were compared to an updated ray trace model for validation. (Figure 19)

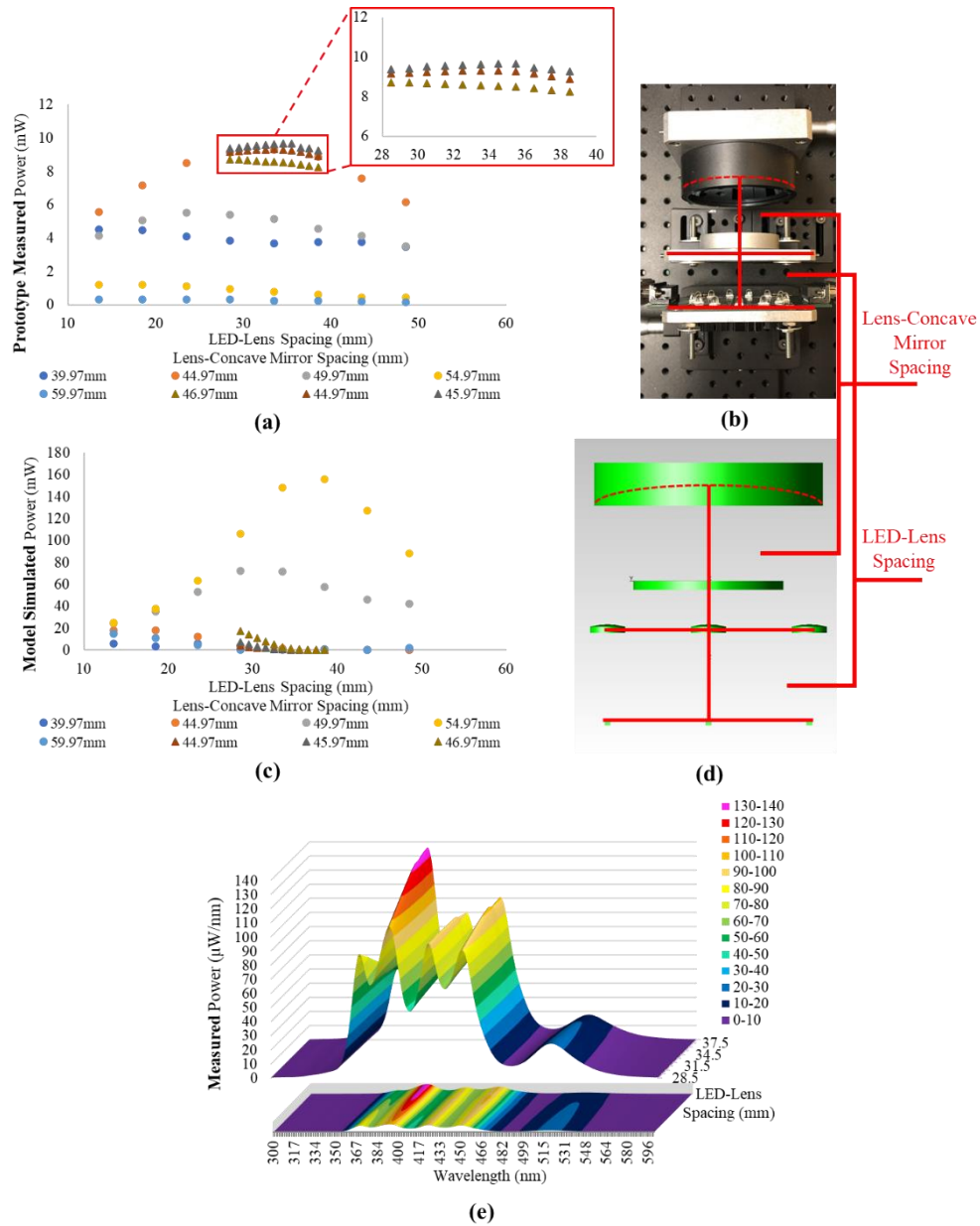


Figure 19. Prototype sensitivity response to optical component position and comparison to ray trace simulations. Independent variables were the concave mirror-lens spacing (represented by different colored data series in the graphs) and LED-lens spacing (represented by each data point in a series). (a) Irradiance measurements of the prototype LED-based illuminator using a spectrometer for integrated optical power. (b) Prototype alignment was adjusted via XY translational stages (see also Figure 18.c). Positions were altered in 5 mm increments (circular data markers). A subset of data was sampled with a 1 mm increment (triangular data markers) so as to accurately identify the optimal position for components (expanded in red of panel (a)). (c) Simulated irradiance measurements of modeled illuminator using ray trace analysis of the same optical components as the prototype (panel (a)) for comparison. (d) Model positions were adjusted *in silico* to match the positions of prototype measurements. The flat mirror and lens spacing were held constant to replicate the stationary position of the prototype mirror and lens plate. (e) The spectral output of the prototype illuminator with 5 wavelengths illuminated simultaneously was used to visualize the dependence of spectral power output on position.

Results from the experimental sensitivity study of the prototype found that a 44.97 mm spacing between concave mirror and lens (focal length of the lenses) and a 33.5 mm spacing between LED and lens were optimal (Figure 19.a). Smaller step sizes revealed that a minor change to a 45.97 mm spacing between concave mirror and lens provided a nominal improvement in overall power output (highlighted expanded view of Figure 19.a). The total power output remained constant across the range of LED-lens spacings evaluated with fine tuning (linearity of the data in the expanded section of Figure 19.a). Therefore, the optical component positions were determined by LED power distribution instead of integrated total power output (Figure 19.e). A 3D plot was used to visualize the spectral power output of the system as a function of LED-lens spacing (Figure 19.e). This information was used to determine the dependence of LED spectral power distribution upon LED-lens spacing and to select a LED-lens spacing that provided consistent power output across all LED wavelengths. The depth axis boundaries of the 3D graph (Figure 19.e) are the same boundaries as the x-axis of the expanded graph in Figure 19.a. While the 37.5 mm LED-lens spacing (the maximum z-axis value of Figure 19.e) produced a single peak wavelength with the highest power output, the 28.5 mm LED-lens spacing produced an even distribution of power across all wavelength bands (the minimum z-axis value of Figure 19.e). This can also be visualized in the compressed view of the 3D plot (the bottom of panel (e)). Hence, a LED-lens spacing of 28.5 mm was selected as a compromise between peak illumination power output and even spectral power distribution.

The optical power output measured in the prototype experimental sensitivity study was compared to simulation results (Figure 19.a,c) and indicated similar overall

trends in the power output of the system as a function of optical component position. Simulation results provided improved optical transmission when compared to the experimental prototype, likely due to the following reasons: 1) the simulation utilized a 5 mm diameter interrogation plane to measure power output whereas the free aperture of the LLG was only 3.5 mm diameter; 2) the simulation measured total power incident upon the interrogation plane whereas the experimental prototype measured power output after coupling through the LLG; 3) the experimental simulation measured power available at the interrogation plane regardless of angular dispersion whereas the LLG utilized in the prototype has a specified full angular acceptance of 72° . The differences in optimal spacing between the lens and concave mirror that were observed between the simulation (54 mm) and experimental prototype (44 mm) are likely accounted for by the nonidealities of the experimental prototype and the limitations of the simulation described above. While absolute power output values differed between experimental and simulation sensitivity studies, the overall trend of radiant power vs. optical component spacing was similar and allowed an optimal spacing to be identified.

Next, the spectral illuminator was implemented with a TE-2000 inverted epifluorescence microscope system and irradiance measurements were made at the microscope stage to assess the total system excitation power output. Within the spectral microscope system, there were multiple optical elements that contributed to optical transmission losses: lenses and mirrors of the dual mirror array illuminator, coupling losses at the entrance to the LLG, transmission losses through the LLG, the LLG microscope collimator, the dichroic mirror, and the lenses and apertures of the microscope objective. Hence, irradiance data acquired at the microscope stage represent

the composite effects of all of these optical elements. Irradiance data were acquired to assess the maximum output of each LED at the stage as well as the power output vs. current supplied by the current drivers, which created a power output vs. reference voltage calibration for each LED. The maximum output ranged from 0.017 – 0.063 mW depending on LED (the TFTF setup ranged from 0.021 – 0.149 mW depending on the band-pass). To illuminate all 13 wavelengths at equal power output (i.e., flat spectral illumination), the highest power output available was 0.017 mW at the microscope stage. This power output was much less than predicted by the ray trace simulations or than indicated by benchtop testing of the spectral illuminator alone, and these additional transmission losses were attributed to effects of the LLG collimator and aperture stops within the microscope objective. Hence, for initial image feasibility testing (below), LEDs were operated at maximum power output to achieve sufficient signal strength within each spectral band, and post-acquisition spectral correction was performed to return the spectral image data to a flat spectral response.

Spectral imaging feasibility tests

Feasibility of the mirror-based spectral LED illuminator for performing excitation-scanning spectral imaging microscopy was evaluated through a side-by-side comparison with a previously-developed spectral illuminator based upon a 300 W Xe arc lamp and TFTF array mounted in a tilting filter wheel to allow for mechanical filter tuning. Both spectral illuminator systems were integrated with an inverted epifluorescence microscope platform and identical samples, from identical fields of view, were imaged on both systems using the same objective and camera. Raw spectral image data were visualized by summing all wavelength bands to view total fluorescence and

through selection of three wavelength bands to view a RGB composite image. A spectral library was then formed by sampling spectra from single-labeled specimens and the library was then used with non-negatively constrained linear unmixing to visualize signals from each of the six labels, as well as autofluorescence. A false-colored merged composite image was then created from unmixed abundance images, and the root-mean-square (RMS) error associated with linear unmixing was also calculated. To assess potential effects of sequential wavelength acquisition on photobleaching, a sample FOV was repeatedly imaged and the spectral bands summed to calculate the total fluorescence intensity. A region of interest (ROI) was then selected and the average summed fluorescence signal extracted for each sequential spectral image set (Figure A5 in Appendix B: Supplemental Document). Results indicate that a signal loss of $\leq 2\%$ of summed fluorescence was present between sequential images for the TFTF system and $\sim 0\%$ signal loss for the LED system (photobleaching loss was below the measurement capability of this approach). Hence, it is likely that the order of wavelength acquisition bands had negligible impact on the fluorescence signatures of the spectral images acquired using the settings described in this study.

A spectral library was constructed by imaging single label control samples for each fluorescent label and extracting the spectral signature of each label (Figure A6 in Appendix B: Supplemental Document). In addition, an unstained slide was imaged to measure the autofluorescence (AF) signature. Imaging was conducted using the thin film tunable filter (TFTF)-based spectral light source and a LED-based spectral light source. Identical objectives, microscope configurations, and imaging parameters were used for the mixed label slide and single label slides. A background region of interest (ROI) was

selected within each spectral image and the background spectrum extracted. The background spectrum and a correction factor (determined for each respective spectral light source) were used to subtract the background and correct each wavelength band to a flat spectral response^{174,205}. A region of high signal strength was selected in the corrected images for each single label sample and autofluorescence, and the representative spectra were extracted. Spectral specificity was validated by linear unmixing of single label spectral images using a spectral library that consisted of the target fluorescent label and autofluorescence for both the TFTF-based system (Figure A7 in Appendix B: Supplemental Document) and the LED-based system (Figure A8 in Appendix B: Supplemental Document). The spectral library containing signatures from all fluorescent labels and autofluorescence was used to unmix spectral image data from the multi-label slides as described in the body of the manuscript. A comparison of the spectral signatures as measured by the two spectral microscope configurations is presented in Figure A9 in Appendix B: Supplemental Document . The spectra were also compared to spectra listed on the manufacture website (Figure A10 in Appendix B: Supplemental Document).

Results from excitation-scanning spectral imaging with the previously developed TFTF system demonstrated that distinct spectral signatures were able to be extracted from single-labeled specimens (Figure A7 of Appendix B: Supplemental Document) and that analysis with linear unmixing allowed clear identification of signals from most labels – autofluorescence, mitochondria, dsDNA, vimentin, and Golgi labels were all easily identifiable (Figure 20.f,i-l). The f-actin label was also identifiable, although appearing with uneven distribution across the field of view (Figure 20.h), while the nuclear pore protein (NPP) had insufficient signal strength to be definitively identified as being

localized to nuclear pore structures (Figure 20.g). It is likely that the NPP signal was inherently low due to the size of the nuclear pore structures and, hence, could not be easily discriminated. Scaling the NPP intensity for improved visualization was found to only magnify the contribution of noise in both individual and merged images. The overlaid unmixed image (Figure 20.c) allowed co-visualization of unmixed components. The Golgi label displayed a relatively strong signal, causing false-colored nuclei to appear purple in the overlaid image, due to merging with the dsDNA signal. However, the excitation spectrum identified from the single-label Golgi sample was weak, and likely mixed with cellular autofluorescence, which was also localized near the nuclei. Hence, it is possible that the Golgi signal resulting from linear unmixing may have been a mixture of autofluorescence and Golgi contributions and did not fully represent Golgi labeling in the cells.

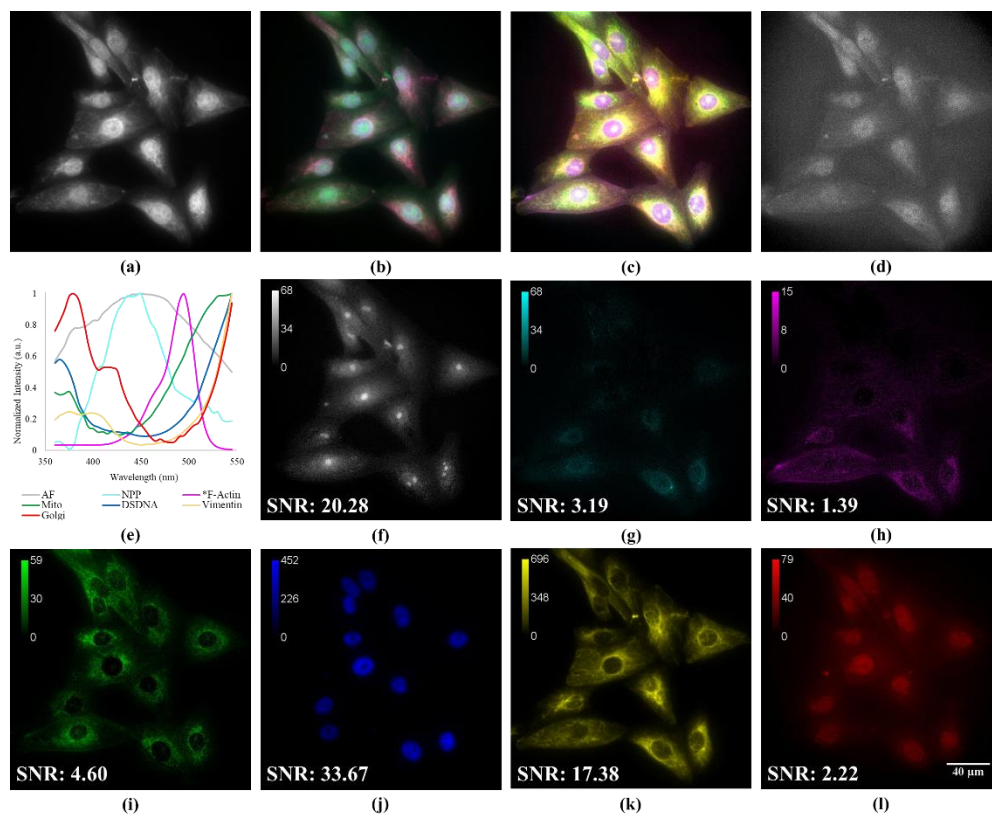


Figure 20. Spectral image data acquired from a 6-label slide using a TFTF-based system for excitation-scanning spectral imaging microscopy. Spectral image data were visualized as (a) a summed intensity and (b) a RGB false-colored image. Unmixed image data were also (c) false-colored and merged for visualization, along with (d) RMS error associated with the unmixing process. To perform unmixing, (e) a spectral library was constructed from single-label control specimens and used to estimate the relative abundance of each fluorescent label in the mixed sample: (f) autofluorescence, (g) NPP, (h) f-actin, (i) mitochondria, (j) dsDNA, (k) vimentin and (l) Golgi.

It should be noted for spectral image data acquired on both the TFTF system and the LED system, that it was not possible to find a region of interest (ROI) with strong f-actin that did not also have significant contributions from cellular autofluorescence, due to the highly autofluorescent nature of African Green Monkey kidney epithelial cells. Hence, the spectrum of the f-actin label, Star Green, was extracted from data provided by the manufacturer for the 38 wavelength bands used in the TFTF system and for the 13 wavelength bands used in the LED system. The localization of labeling in the unmixed

data indicates that signals from f-actin do appear to be localized within actin filament structures, although there was non-uniform distribution of the unmixed f-actin signal, as described above.

Upon completion of imaging with the TFTF system, the same FOV was imaged using the LED array system for a side-by-side comparison (Figure 22). Linear unmixing of spectral image data acquired with the LED-based system allowed clear identification of autofluorescence, dsDNA and vimentin (Figure 21.f,j,k) and partial identification of NPP, f-actin, mitochondria and Golgi (Figure 21.g,h,i,l). While the mitochondria and f-actin signals had degraded signal as compared to data from the TFTF-based system, unmixing still allowed identification of signal that was localized to the correct subcellular locations. Interestingly, the Golgi signal appeared better localized to perinuclear locations for the LED-based system than for the TFTF-based system. In comparing system response, it should be noted that the prototype LED-based system was configured with 13 wavelength bands, as compared to the 38 bands used for the TFTF-based system (wavelengths indicated in Table 9). In addition, radiant output power measurements of the LED system were acquired at the microscope stage, prior to imaging, indicating an average of ~40% less power than that of the TFTF-based system.

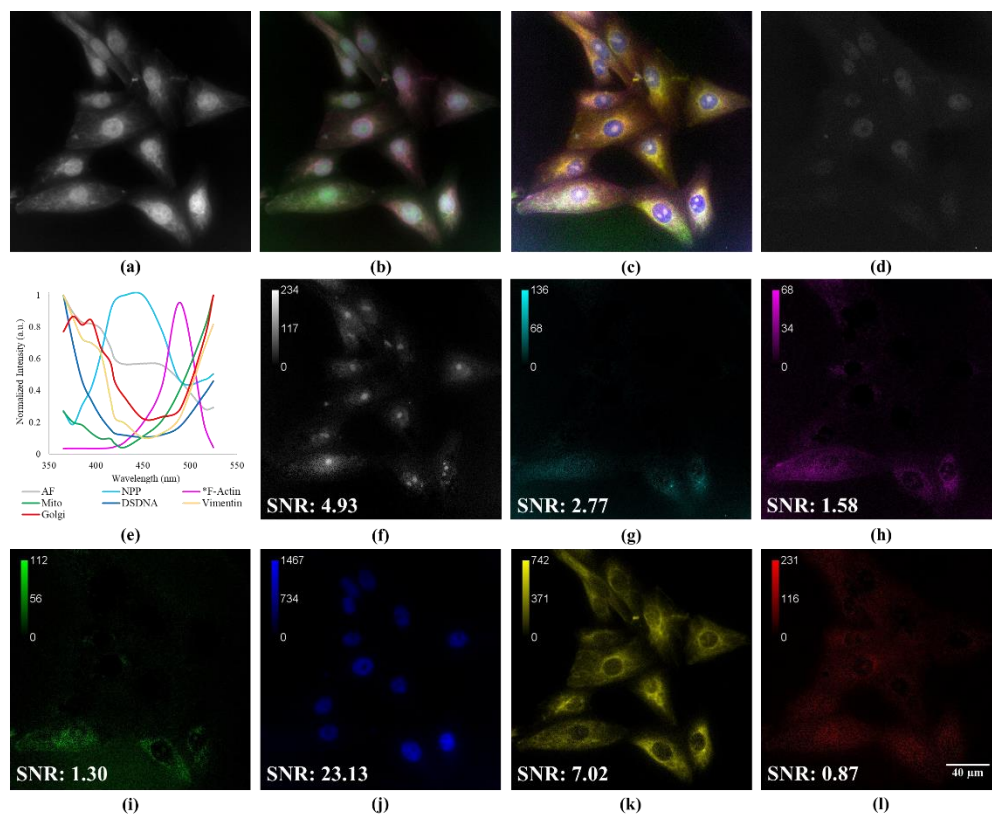


Figure 21. Spectral image data acquired from a 6-label slide using the prototype LED-based system for excitation-scanning spectral imaging microscopy. Spectral image data were visualized as (a) a summed intensity and (b) a RGB false-colored image. Unmixed image data were also (c) false-colored and merged for visualization, along with (d) RMS error associated with the unmixing process. To perform unmixing, (e) a spectral library was constructed from single-label control specimens and used to estimate the relative abundance of each fluorescent label in the mixed sample: (f) autofluorescence, (g) NPP, (h) f-actin, (i) mitochondria, (j) dsDNA, (k) vimentin and (l) Golgi.

To further compare system performance of the TFTF-based system and the LED-based system, the number of wavelength bands utilized by the TFTF-based system was down-sampled so as to match the number and wavelength location of bands provided by the LED-based system. The down-sampled spectral image data were unmixed and analyzed using the same process as described above for the full spectral image data set, and resulting unmixed images were false-colored and merged for visual comparison (Figure 22). In general, there was a strong agreement in signals identified between the

three data sets – the TFTF-based system with all wavelength bands (Figure 22.a), the TFTF-based system with reduced number of wavelength bands (Figure 22.b) and the LED-based system (Figure 22.c). The signal-to-noise ratio (SNR) ranges for the TFTF-based system with reduced number of wavelength bands and the LED-based system were equitable. The SNR of the TFTF-based system with the full wavelength range was higher and can be attributed to the higher irradiance output and the higher number of wavelengths scanned. Two noticeable differences between the TFTF-based system and the LED-based system were the level of noise (the LED-based system generated images with reduced SNR compared to that of the TFTF-based system) and that nuclei appear more blue in false-colored images from the LED-based system due to the absence of Golgi signal in the nuclei (more accurate identification of Golgi to perinuclear locations). The differences in SNR between the TFTF and LED systems are likely attributed to the following (in order of impact): 1) differences in illumination power and subsequent photon budget available at the detector, 2) the number of spectral bands scanned and 3) potentially minor differences in the bandwidth of the spectral bands between the two systems, which when combined with the excitation spectral properties of each fluorescent label may result in subtle variations in detection sensitivity for each label. Illumination power likely directly correlates with SNR, as a 40% decrease in average illumination is very comparable to the 40% average decrease in SNR, as measured across the different spectrally-unmixed channels. However, the LED-based system acquired spectral images that contained fewer (66% decreased) spectral bands than the TFTF-based system, and it is likely that the reduced number of spectral bands also affected the SNR of unmixed images. In fact, when the spectral image data from the TFTF-based system was

subsampled to contain the same number of spectral bands and identical band location as the LED-based system, the unmixed images from both systems displayed a similar range in SNR values. Hence, it is likely that both decreased illumination power primarily affected the SNR of resultant unmixed images, while decreased spectral sampling had a secondary and compounding effect. Further data are supplied in Appendix B: Supplemental Document for building and verifying the spectral library, including: Abberior stain spectral data (Figure A6), analysis and verification of single-labeled control samples for both systems (Figure A7 and Figure A8) and comparison of fluorescent label spectra for each component between the two spectral light sources used for imaging (Figure A9 and Figure A10).

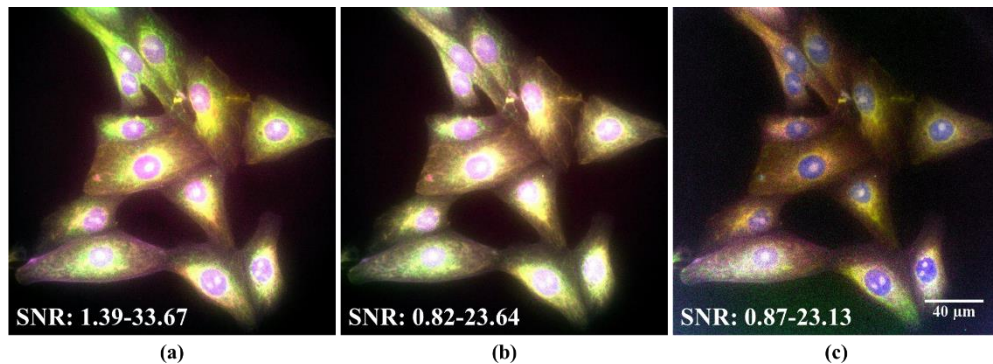


Figure 22. A side-by-side comparison excitation-scanning spectral image data acquired from the same field of view using: (a) a TTF-based system when imaging with 38 wavelength bands, (b) a TTF-based system when imaging with 13 wavelength bands (c) and the prototype LED-based system when imaging with 13 wavelength bands.

Discussion

Spectral imaging approaches have shown great utility in fluorescence microscopy, but often come at the price of increased acquisition time and/or decreased signal strength. In this manuscript, we have presented simulation, prototyping, benchtop testing, and

feasibility imaging results for a prototype spectral illuminator that allows excitation-scanning spectral imaging to be performed on an epifluorescence microscope platform with rapid wavelength switch times. The novel spectral illuminator is based on an optical geometry that uses two mirrors to combine light from an array of wavelength-dependent LEDs in a manner similar to Cassegrain style telescopes. The prototype LED-based system was compared to a preexisting TFTF-based system, and results indicate that both systems provided the ability to discriminate multiple fluorescent label signatures in a highly-labeled sample, although the TFTF-based system provided higher illumination power at the sample stage and correspondingly higher signal-to-noise characteristics in unmixed images. The LED-based system did provide a streamlined optical design that acquired a spectral image stack at comparable acquisition rates of standard spectral imaging systems due to the electronic switching of band-passes instead of mechanical tuning. Both systems acquired spectral image data in a similar manner, through sequential illumination of excitation wavelength band while acquiring an image at each band. The TFTF system used an array of filters in a tiltable filter wheel, where each filter could be selected through rotation and then the angle of the filter relative to the incident light could be adjusted by tilting the wheel. The LED system used sequential electronic triggering of each LED, where a typical LED rise or fall time is on the order of $0.01 \mu\text{s}$. The long-term goal of this work is to enable high-speed acquisition of spectral fluorescence microscopy images with an acquisition speed of 5-10 ms per wavelength band. Hence, the LED rise and fall time of $\sim 0.01 \mu\text{s}$ adds a negligible delay for high-speed spectral imaging. By contrast, the TFTF system requires between 50-200 ms to switch between wavelength bands, depending up on whether the wavelength band switch

requires adjustment of the tilt of the filter wheel or rotation to an adjacent filter in the wheel. To ensure sufficient time for all wavelength switches, a 200 ms wait time was required after issuing each wavelength switch command before acquiring the corresponding wavelength band images. Hence, mechanical movement of the TFTF system becomes prohibitively rate limiting when using acquisition times of ~10 ms per wavelength band.

Unmixed spectral image data acquired using both the TFTF system and LED system were comparable, albeit when operating the LED system at a reduced acquisition speed. When comparing the TFTF spectral image acquired with identical wavelength bands as the LED spectral image, unmixed images from both systems presented comparable SNR (Fig 7.b,c). Acquisition speed of the LED system was slower (Table 9) to compensate for an average of 40% reduction in illumination power. Factors that contribute to the illumination power losses in the LED system include the incident angle of each LED light path upon the incident face of the LLG and the beam diameter at the LLG. In this initial prototype, the beam diameter is larger than the entrance aperture of the LLG, and light outside of the entrance aperture is discarded. By contrast, the TFTF system features a single beam that is orthogonally incident upon the LLG entrance aperture (as opposed to an off angle) and LLG coupling is more efficient. Hence, further refinement of the prototype LED-based system is needed to match the power output characteristics of the TFTF-based system and, ideally, to allow spectral data to be acquired at high speeds with negligible time delays introduced by the electronic wavelength switching of LEDs. These capabilities are important to support live, real-time, multi-label cellular studies.

Model and prototype validation

A conceptual model and a subsequent series of ray trace simulations were performed to optimize optical power transmission by systematically adjusting geometric and optical parameters of the system. Upon optimization at a single wavelength, the model was expanded to simulate transmission of multiple wavelengths. However, the full parametric sensitivity study and optimization process was performed on just a single wavelength band before expanding to all wavelength bands, in order to streamline the simulation process. Hence, there may be subtle compromises in component spacing or alignment to allow approximately uniform optical transmission across all wavelength bands that were required to be made during the prototyping and benchtop testing phases and which could conceivably have been accounted for during the modeling phase, albeit at the expense of increased computational burden and more complex designs for optical alignment components to adjust geometry independently for each wavelength. A revised simulation that included 5 wavelength bands was used to compare wavelength- and LED placement-dependent effects between the simulation and benchtop measurements (Figure 19). For imaging experiments, sample refocus was not performed for each wavelength band as it was assumed that the chromatically-corrected objective provided an equivalent focal length across the range of wavelengths utilized in this study.

In addition, the geometry of the initial prototype was designed to match the optimal optical power transmission characteristics provided by a particular combination of mirror and lens diameter and focal length. This included limiting the number of excitation wavelengths to 13, due to packing constraints in designing the lens array cage plate. In future prototypes, it is likely that alternative lens packing geometries may be

implemented that will allow a greater number of wavelength bands to allow for increased wavelength sampling between 350 nm and 600 nm. One compromise to note was that shorter focal lengths of the concave mirror resulted in an incident angle of illumination that was greater than the acceptance angle (as determined by the numerical aperture) of the LLG. Ultimately, a shorter focal length (76.2 mm) mirror was implemented because the highest simulated transmission optical transmission could be improved by ensuring that the incident angle of light was within the LLG acceptance angle.

A design restriction maintained in both the design and prototype was the lenses and flat mirror were secured using the same cage plate (Figure 18.b). This restriction was necessary as a separate cage plate for the flat mirror would have occluded the light path between the lens and curved mirror. However, this design restriction also served to limit the range of adjustment in the spacing between the flat mirror and the lenses (this distance can be minimally adjusted through the threaded lens tube that secures the flat mirror). Related, the constraint of mounting all lenses within a single cage plate, also limited the amount of adjustment that could be performed to mitigate effects from chromatic aberration.

Future modeling goals include the development of an illuminator geometry with 32+ wavelengths and that can allow increased geometric translation of individual optical components, while maintaining accurate alignment. In addition, the use of longer lens tubes will be simulated to assess the utility of enabling individual movement of lenses to compensate for chromatic effects.

Uniform spectral output

A benefit of the LED-based spectral illuminator is the control of the power output for individual wavelengths. This allows the ability to implement uniform excitation illumination (flat spectral output) across a range of wavelengths. For this initial study, the optical transmission through the liquid light guide and microscope body resulted in a low illumination power at the microscope stage. Based on benchtop testing of the integrated system with power measurements made at the microscope stage, we determined that a uniform spectral output of 0.017 mW could be achieved, or that, alternatively, LEDs could be operated at maximum output ranging between 0.017 – 0.063 mW, depending on wavelength band. The proof-of-principle imaging results described here were performed using the maximum power output setting per wavelength band to maximize signal-to-noise characteristics of the acquired images. Post-acquisition correction was used to restore spectral image data back to a uniform spectral response (this same process used to correct spectral data acquired from the TFTF-based system)¹⁷⁴. However, in future prototypes, if the optical power output available at the stage is increased, it may be advantageous to operate the system in a uniform spectral output mode and to remove the need for post-acquisition spectral correction while also increasing the useable lifetime of the LEDs as they would not be operated at 95% of maximal rated output.

Future system design objectives

The prototype LED-based system described in this research presented with reduced illumination throughput due to light losses when coupling to the LLG, likely a result of beam diameter and incident angle mismatch. This loss resulted in a lower photon budget when acquiring fluorescence images. In order to achieve a moderate SNR, the

acquisition speed was reduced when compared to the TTF-based system. Future work will focus on reducing the beam diameter for each LED. If necessary, the concave mirror and hence incident angle on the LLG may be adjusted. Based upon the LLG manufacturer specifications, 3 mm beam diameter and $\leq 36^\circ$ incident angle are needed to achieve optimal coupling. Meeting these parameters will provide increased illumination power, and a corresponding increase in available acquisition speed. An additional future objective is to modify the geometry of the system so as to allow for 32 excitation wavelength bands.

Of note, the LED-based spectral illuminator module described here features a streamlined and compact optical design. This design provides benefits in terms of production scalability and translatability to other imaging platforms. We anticipate that the spectral illumination source could be commercialized in a manner that is simple and moderately priced when manufactured at large-scale. In specific, the streamlined and modular nature of the light path would allow for hardware and cage system components to be manufactured using 3D printing additive techniques to minimize production costs. Similarly, optical components would have pre-defined placement within the assembly that would require minimal alignment or adjustment. In addition, the spectral illuminator design could be modified to allow more LEDs or wavelengths by increasing the mirror diameter and/or allowing for concentric rings of LEDs. It may also be possible to further increase the number of wavelength bands of the spectral illuminator by using band-pass filters, placed immediately after LEDs, to further select specific wavelength bands for illumination and when using wide bandwidth LEDs, to select more than one wavelength band from a specific model of LED. The modular spectral illumination source could also

be translated to other platforms, such as high throughput imaging systems, microscope slide scanners, or endoscopes. Hence, the streamlined design presented here has potential for high-speed spectral imaging for fluorescence microscopy, as well as potentially a range of alternative imaging platforms.

Funding

The authors would like to acknowledge support from the NASA/Alabama Space Grant Consortium, NASA grant award NNH19ZHA001C, NSF grant award 1725937, NIH grant awards UL1TR001417, P01HL066299, R01HL137030, the University of Alabama at Birmingham Center for Clinical and Translational Science (CCTS), and the Economic Development Partnership of Alabama.

Acknowledgements

Optical design support was provided by Lambda Research Corp., TracePro Expert non-profit thesis version. Optical design support and component fabrication were contracted through ThorLabs, Inc.

Disclosures

Drs. Leavesley and Rich disclose financial interest in a start-up company, SpectraCyte LLC, founded to commercialize spectral imaging technologies.

Data underlying the results in this paper are available in Ref.²²⁹

See Supplement 1 for supporting content.

References

The reference section for this manuscript has been combined in the dissertation reference section.

CHAPTER VI: DISSERTATION PORTFOLIO SUMMARY AND FUTURE DIRECTIONS

This dissertation presents endoscopy from a system engineering perspective and evaluates two novel optical configurations for hyperspectral imaging. Current endoscopic systems strive to distinguish normal and abnormal, neoplasia or inflamed tissue. However, endoscopy technology is limited when detecting small or flat abnormalities. Undetected lesions or inflammation have the potential to grow and become high-risk. Therefore, detecting abnormalities early is vital to a patient's long-term health. Additionally, a way to quantify or determine the risk of these early detections would significantly benefit endoscopic screenings in accuracy and efficiency (full confidence of when to resect and how much to resect). The next iteration of the endoscope system needs to improve the definition or contrast of neoplasia to the surrounding mucosa and quantify risk for mitigation decisions. The system engineering analysis (Chapter III) detailed the architecture at vital milestones throughout the lifetime of the technology, finding trends in subsystems or components and theorizing what the next milestone will be. Based on the current endoscope modalities and similar technologies on the market, of future systems will need to be capable of contrasting many molecular and/or tissue components and displaying these differences in a meaningful way that a clinician can use

to make diagnostic decisions. This could be accomplished by one or many technologies as long as they can be implemented for real-time detection and analysis.

One of the scenarios suggested in Chapter III involved hyperspectral imaging (either with chromoendoscopy or autofluorescence imaging) and the subsequent chapters explored possible hyperspectral configurations. Traditionally, hyperspectral imaging is accomplished by filtering a broadband light source (including the sun) on the excitation and/or the emission side of the light path. Filtering allows for precise spectral selection but decreases the photon budget or transmission of light through the light path. The hyperspectral modules in Chapters IV and V aimed to minimize filtering needs by removing emission filters and replacing broadband illumination (and associated excitation filters) with many wavelength-specific LEDs combined to a common output. Combining the LEDs was accomplished by multi-furcated solid light guide (Chapter IV) or Cassegrain-style dual mirror array (Chapter V). In addition to transmission losses with filtering optics, in a subset of hyperspectral setups there is a mechanical tuning to filter band-passes of a broadband light source to acquire the hyperspectral image. This limits acquisition rates to the speed of the mechanical motor changing the bandpass. Using LEDs, the mechanical limitation is eliminated. Therefore, both spectral illuminators, detailed in Chapters IV and V, have increased illumination and faster wavelength switching rates. However, narrowband LEDs produce a more diffuse light output than spectrally filtered broadband illumination from a Xe arc lamp; focusing and combining many LEDs proved challenging. Transmission to the distal end of an endoscope or the microscope stage was lower than current technologies due to limitations in coupling the diffuse light source into a fiber optic or a liquid light guide. However, even with lower

illumination throughput, feasibility testing proved that LED-based excitation-scanning hyperspectral imaging is possible for real-time spectroscopic analysis on an endoscope and microscope platform. Spectral images were acquired on both setups, demonstrating proof-of-principle results for spectral autofluorescence and similar-to-NBI reflected light imaging of *ex vivo* swine colon using the endoscope, and imaging and spectral separation of 6 exogenous fluorophores on fixed cell slides with the microscope. Throughout each manuscript, definitive trade-offs between spatial resolution, spectral sampling and acquisition rates are discussed²³⁰. This applies to other multidimensional imaging techniques (i.e., OCT, VE) as well. Any future endoscopic system that implements complex imaging techniques will have to minimize trade-offs. In summary, this dissertation included three manuscripts to meet the objective stated in Chapter I: integrate hyperspectral imaging into an endoscopic platform to provide reflectance, fluorescence or mixed spectroscopic data as a technique to enhance contrast in endoscopic screening. Chapter III displayed a systems engineering perspective of past, current and future endoscopic technology. Chapters IV and V integrate hyperspectral technology into endoscope and microscope platforms. The data from these two chapters successfully produced reflectance and fluorescence spectroscopic data and spectrally unmixed many components to enhance contrast. The singular part of the objective that was not met was the real-time aspect of the data acquisition. However, both Chapters IV and V mentioned the ability acquire video-rate hyperspectral data with these systems that is expected to be achievable within the next design iteration. Therefore, the objective was successfully met with the work described in the previous chapters. Imaging results from these new technologies will provide the basis for further studies and systems design objectives.

The future directions of the work presented in this dissertation have several different avenues including: further development of the concept of operations (ConOps) for the future endoscope iterations discussed in Chapter III, optimizing optical throughput of the spectral prototypes presented in Chapters IV and V, design of a new light path to combine many LED sources to accomplish real-time hyperspectral imaging, implement machine learning (ML)/artificial intelligence (AI) to analyze the excitation-scanning hyperspectral image data or test other spectroscopic aspects that were not accomplished in this dissertation. The future endoscopes conceptualized and ranked in Chapter III were based on exploring other technologies already in existence. Complete systems analysis requires detailing the use case scenarios and continual feedback from stakeholders to create the ConOps for (ideally) each theorized setup. Future ConOps would emphasize the utility of each scenario adding another metric to the decision-making process of which path is optimal.

Optimization of the two light paths detailed in Chapters IV and V were discussed in the respective chapters. The goal is to focus and preserve as much illumination from each diffuse LED prior to combination. Ideally, if LEDs were collimated instead of diffuse, then manipulation of the light paths in combination and coupling optics to the respective platforms would be straightforward. In the real world, non-ideal case, the goal is to focus as much of the light through the light combining optics accounting for focal points, angle of reflection, refraction and acceptance angles (or numerical aperture) of the coupling optics. The latter independent variables are based on the wavelength combining optics design. Chapter IV includes an optimization of the multi-furcated solid light guide simulation. The results demonstrated that some optimal designs are not easily fabricated.

Hence, it is important to consider both theoretical operations and real-world manufacturing constraints when designing these new optics to combine many LEDs to a common output. The dual mirror setup in Chapter V is likely the best current option for combining illumination of multiple LEDs. The mirrors can be optimized to account for focus, reflection and numerical aperture. A minimum of doubling the current transmission throughput would prove a substantial increase in photon budget to increase acquisition rates (potentially video-rate) and provide improved spatial resolution.

Completely different multi-LED spectral light path designs prove to be an interesting point of future work but also the most challenging. Any design would need to be cognizant of the spatial-spectral-temporal trade-off and meet the requirement of video-rate and high-definition resolution. Combining light sources could use a multi-faceted mirror similar to a reverse flashlight or an array of mirrors that maintain all pathways in 2-dimensions instead of the 3-dimensional version of Chapter VI. Returning to filtering broadband sources could be an option if the light path was simple to maintain high transmission and acquisition rates.

As mentioned in Chapter III, the future of endoscopy is big data and one way to screen through the data quickly is the use of ML/AI. A primary technique is implementing a neural network (NN) to classify the dataset into categories. In the case of these data, the goal would be to classify tissues as normal, cancerous or neoplastic. The spectroscopic information of hyperspectral images would provide additional information to aid the network's decision. Preliminary work is in progress to create NNs for these data in collaboration with Dr. Na Gong.

Similar to new designs, there are spectroscopic studies that would provide insight in design choices. One important study is spectral sampling of a library of endogenous and exogenous fluorophores. Determining a sufficient number of LEDs or wavelength sampling to correctly identify biomarkers and a mixture of biomarkers could reduce the number of LEDs or band-passes needed in the optical light path. Additionally, test the illumination output and spectral imaging with multiple of the same bandwidth (either LEDs or band-passes) in the array to observe an increased throughput of weaker bandwidths. Another spectroscopic study of interest would be to test an excitation-scanning hyperspectral unit that operates in the near infrared (NIR) wavelength range. Most NIR imaging systems are single wavelength for fluorescence or phototherapy^{152,231,232}. There is potential for a new layer of information when imaging with several NIR wavelengths in a hyperspectral design. Both widefield and interferometry settings would be interesting to test for image results. Future spectroscopic analyses could involve optics and sensors sensitive to the visible and NIR spectrum to capture a range of spectral features of biological systems.

The focus of this dissertation is to develop LED-based excitation-scanning hyperspectral imaging within the endoscope system, however, this technology or subsystem can be implemented for other applications. A palpable (and previously discussed) option is utilizing this technology for microscopy. The ability to acquire real-time (mixed) spectroscopic data for microscopic imaging would be highly beneficial. Live transport phenomena or ultrafast second messenger signaling (i.e., Ca²⁺ “sparks” or cyclic AMP) could be captured and decomposed by component for deeper understanding for cellular functions. This HSI technique could be implemented in certain cases for

remote sensing or agriculture with an altered optical pathway on an unmanned aerial vehicle (UAV) providing some of the first excitation-based data in these fields. There is possible value in this technology for applications of food or chemical screenings, security biometrics, even hobby or personal photography. LED-based excitation-scanning hyperspectral imaging has great potential for a range of fields to produce more image data for further analysis, contrast and enhancement.

In summary, this dissertation provided a condensed system architecture of the endoscope throughout the system lifetime to the current iteration. This architecture can be the basis for future endoscope systems but for the scope of this work the system trends were analyzed for optimums, areas of improvement and new technology implementation. One such technology (hyperspectral imaging) was detailed and tested in subsequent chapters. The two spectral illuminator designs proved feasible for real-time hyperspectral imaging with some optimization. Future prototypes will be designed to increase transmission throughput and provide real-time spectroscopic analysis in high-definition. The future of endoscopy is complex and computationally focused to provide increased contrast between normal tissue and small abnormalities or neoplasia. This dissertation accomplished an original system architecture for endoscopy and two spectral illuminators for a novel hyperspectral imaging technique as building blocks for the future endoscope.

REFERENCES

REFERENCES

- [1] Bronte, C., [Jane Eyre - Charlotte Bronte] , Lumbreras Classics Books (2021).
- [2] “Advertising,” in Syd. Mail New South Wales Advert., New South Wales (1906).
- [3] [Every Picture Tells A Story] (1971).
- [4] Siegel, R.L., Miller, K.D., and Jemal, A., “Cancer statistics, 2016,” *CA: a cancer journal for clinicians* 66(1), 7–30 (2016).
- [5] Siegel, R.L., Miller, K.D., and Jemal, A., “Cancer statistics, 2017,” *CA: A Cancer Journal for Clinicians* 67(1), 7–30 (2017).
- [6] Siegel, R.L., Miller, K.D., and Jemal, A., “Cancer statistics, 2019,” *CA: a cancer journal for clinicians* 69(1), 7–34 (2019).
- [7] Siegel, R.L., Miller, K.D., Sauer, A.G., Fedewa, S.A., Butterly, L.F., Anderson, J.C., Cercek, A., Smith, R.A., and Jemal, A., “Colorectal cancer statistics, 2020,” *CA: A Cancer Journal for Clinicians* 70(3), 145–164 (2020).
- [8] Rex, D.K., Cutler, C.S., Lemmel, G.T., Rahmani, E.Y., Clark, D.W., Helper, D.J., Lehman, G.A., and Mark, D.G., “Colonoscopic miss rates of adenomas determined by back-to-back colonoscopies,” *Gastroenterology* 112(1), 24–28 (1997).
- [9] van Rijn, J., Reitsma, J., Stoker, J., Bossuyt, P., van Deventer, S., and Dekker, E., “Polyp miss rate determined by tandem colonoscopy: a systematic review.,” *The American journal of gastroenterology* 101(2), 343 (2006).
- [10] Church, J.M., “Clinical significance of small colorectal polyps,” *Diseases of the colon & rectum* 47(4), 481–485 (2004).
- [11] Kim, N.H., Jung, Y.S., Jeong, W.S., Yang, H.-J., Park, S.-K., Choi, K., and Park, D.I., “Miss rate of colorectal neoplastic polyps and risk factors for missed polyps in consecutive colonoscopies,” *Intestinal Research* 15(3), 411–418 (2017).
- [12] Lee, J., Park, S.W., Kim, Y.S., Lee, K.J., Sung, H., Song, P.H., Yoon, W.J., and Moon, J.S., “Risk factors of missed colorectal lesions after colonoscopy,” *Medicine* 96(27), (2017).
- [13] Schowengerdt, R.A., [Remote sensing: models and methods for image processing] , Elsevier (2006).
- [14] Mulla, D.J., “Twenty five years of remote sensing in precision agriculture: Key advances and remaining knowledge gaps,” *Biosystems Engineering* 114(4), 358–371 (2013).
- [15] Lu, R., and Chen, Y.-R., “Hyperspectral imaging for safety inspection of food and agricultural products,” presented at Photonics East (ISAM, VVDC, IEMB), 1999, 121–133.

- [16] Cavalli, R.M., Colosi, F., Palombo, A., Pignatti, S., and Poscolieri, M., “Remote hyperspectral imagery as a support to archaeological prospection,” *Journal of Cultural Heritage* 8(3), 272–283 (2007).
- [17] Lu, G., and Fei, B., “Medical hyperspectral imaging: a review,” *Journal of biomedical optics* 19(1), 010901 (2014).
- [18] Bolin, S., Nilsson, E., and Sjö Dahl, R., “Carcinoma of the colon and rectum--growth rate.,” *Annals of Surgery* 198(2), 151–158 (1983).
- [19] Pickhardt, P.J., Kim, D.H., Pooler, B.D., Hinshaw, J.L., Barlow, D., Jensen, D., Reichelderfer, M., and Cash, B.D., “Assessment of volumetric growth rates of small colorectal polyps with CT colonography: a longitudinal study of natural history,” *The Lancet Oncology* 14(8), 711–720 (2013).
- [20] Matsumoto, T., Esaki, M., Fujisawa, R., Nakamura, S., Yao, T., and Iida, M., “Chromoendoscopy, narrow-band imaging colonoscopy, and autofluorescence colonoscopy for detection of diminutive colorectal neoplasia in familial adenomatous polyposis.,” *Diseases of the Colon & Rectum* 52(6), 1160–1165 (2009).
- [21] Chiu, H.-M., Chang, C.-Y., Chen, C.-C., Lee, Y.-C., Wu, M.-S., Lin, J.-T., Shun, C.-T., and Wang, H.-P., “A prospective comparative study of narrow-band imaging, chromoendoscopy, and conventional colonoscopy in the diagnosis of colorectal neoplasia,” *Gut* 56(3), 373–379 (2007).
- [22] Chung, S.J., Kim, D., Song, J.H., Kang, H.Y., Chung, G.E., Choi, J., Kim, Y.S., Park, M.J., and Kim, J.S., “Comparison of detection and miss rates of narrow band imaging, flexible spectral imaging chromoendoscopy and white light at screening colonoscopy: a randomised controlled back-to-back study,” *Gut* 63(5), 785–791 (2014).
- [23] Togashi, K., Osawa, H., Koinuma, K., Hayashi, Y., Miyata, T., Sunada, K., Nokubi, M., Horie, H., and Yamamoto, H., “A comparison of conventional endoscopy, chromoendoscopy, and the optimal-band imaging system for the differentiation of neoplastic and non-neoplastic colonic polyps.,” *Gastrointestinal endoscopy* 69(3 Pt 2), 734 (2009).
- [24] Davila, R., “Chromoendoscopy.,” *Gastrointestinal endoscopy clinics of North America* 19(2), 193 (2009).
- [25] Chung, S.J., Kim, D., Song, J.H., Park, M.J., Kim, Y.S., Kim, J.S., Jung, H.C., and Song, I.S., “Efficacy of computed virtual chromoendoscopy on colorectal cancer screening: a prospective, randomized, back-to-back trial of Fuji Intelligent Color Enhancement versus conventional colonoscopy to compare adenoma miss rates,” *Gastrointestinal Endoscopy* 72(1), 136–142 (2010).
- [26] Jang, J.-Y., “The Past, Present, and Future of Image-Enhanced Endoscopy,” *Clinical Endoscopy* 48(6), 466–475 (2015).
- [27] Gono, K., “Narrow Band Imaging: Technology Basis and Research and Development History,” *Clinical Endoscopy* 48(6), 476–480 (2015).
- [28] Kaltenbach, T., Friedland, S., and Soetikno, R., “A randomised tandem colonoscopy trial of narrow band imaging versus white light examination to compare neoplasia miss rates.,” *Gut* 57(10), 1406 (2008).

- [29] Ignjatovic, A., East, J., Guenther, T., Hoare, J., Morris, J., Ragnath, K., Shonde, A., Simmons, J., Suzuki, N., et al., “What is the most reliable imaging modality for small colonic polyp characterization? Study of white-light, autofluorescence, and narrow-band imaging,” *Endoscopy* 43(2), 94–99 (2011).
- [30] Lee, C.K., Lee, S.-H., and Hwangbo, Y., “Narrow-band imaging versus I-Scan for the real-time histological prediction of diminutive colonic polyps: a prospective comparative study by using the simple unified endoscopic classification,” *Gastrointestinal Endoscopy* 74(3), 603–609 (2011).
- [31] Nakamura, M., Nishikawa, J., Hamabe, K., Goto, A., Nishimura, J., Shibata, H., Nagao, M., Sasaki, S., Hashimoto, S., et al., “Preliminary study of photodynamic diagnosis using 5-aminolevulinic acid in gastric and colorectal tumors,” *World Journal of Gastroenterology : WJG* 21(21), 6706–6712 (2015).
- [32] van der Heijden, E.H., Hoefsloot, W., van Hees, H.W., and Schuurbijs, O.C., “High definition bronchoscopy: a randomized exploratory study of diagnostic value compared to standard white light bronchoscopy and autofluorescence bronchoscopy,” *Respiratory Research* 16(1), 33 (2015).
- [33] Moghissi, K., Dixon, K., and Stringer, M.R., “Current indications and future perspective of fluorescence bronchoscopy: A review study,” *Photodiagnosis and Photodynamic Therapy* 5(4), 238–246 (2008).
- [34] Melgani, F., and Bruzzone, L., “Classification of hyperspectral remote sensing images with support vector machines,” *IEEE Transactions on Geoscience and Remote Sensing* 42(8), 1778–1790 (2004).
- [35] Lee, W.S., Alchanatis, V., Yang, C., Hirafuji, M., Moshou, D., and Li, C., “Sensing technologies for precision specialty crop production,” *Computers and Electronics in Agriculture* 74(1), 2–33 (2010).
- [36] Sankaran, S., Mishra, A., Ehsani, R., and Davis, C., “A review of advanced techniques for detecting plant diseases,” *Computers and Electronics in Agriculture* 72(1), 1–13 (2010).
- [37] Ishida, T., Kurihara, J., Viray, F.A., Namuco, S.B., Paringit, E.C., Perez, G.J., Takahashi, Y., and Marciano, J.J., “A novel approach for vegetation classification using UAV-based hyperspectral imaging,” *Computers and Electronics in Agriculture* 144, 80–85 (2018).
- [38] Cavalli, R.M., Licciardi, G.A., and Chanussot, J., “Detection of anomalies produced by buried archaeological structures using nonlinear principal component analysis applied to airborne hyperspectral image,” *IEEE Journal of Selected Topics in Applied Earth Observations and Remote Sensing* 6(2), 659–669 (2013).
- [39] ElMasry, G., and Wold, J.P., “High-Speed Assessment of Fat and Water Content Distribution in Fish Fillets Using Online Imaging Spectroscopy,” *Journal of Agricultural and Food Chemistry* 56(17), 7672–7677 (2008).
- [40] Sun, D.-W., [Hyperspectral imaging for food quality analysis and control] , Elsevier (2010).
- [41] Kim, S.J., Zhuo, S., Deng, F., Fu, C.-W., and Brown, M., “Interactive visualization of hyperspectral images of historical documents,” *IEEE transactions on visualization and computer graphics* 16(6), 1441–1448 (2010).

- [42] Goltz, D., Attas, M., Young, G., Cloutis, E., and Bedynski, M., “Assessing stains on historical documents using hyperspectral imaging,” *Journal of cultural heritage* 11(1), 19–26 (2010).
- [43] Duraipandian, S., Bergholt, M.S., Zheng, W., Ho, K.Y., Teh, M., Yeoh, K.G., So, J.B.Y., Shabbir, A., and Huang, Z., “Real-time Raman spectroscopy for in vivo, online gastric cancer diagnosis during clinical endoscopic examination,” *Journal of biomedical optics* 17(8), 081418 (2012).
- [44] Halicek, M., Fabelo, H., Ortega, S., Callico, G.M., and Fei, B., “In-vivo and ex-vivo tissue analysis through hyperspectral imaging techniques: Revealing the invisible features of cancer,” *Cancers* 11(6), 756 (2019).
- [45] Han, Z., Zhang, A., Wang, X., Sun, Z., Wang, M.D., and Xie, T., “In vivo use of hyperspectral imaging to develop a noncontact endoscopic diagnosis support system for malignant colorectal tumors,” *Journal of biomedical optics* 21(1), 016001 (2016).
- [46] Wang, W., Zhao, J., Short, M., and Zeng, H., “Real-time *in vivo* cancer diagnosis using raman spectroscopy: Real-time in vivo cancer diagnosis using raman spectroscopy,” *Journal of Biophotonics* 8(7), 527–545 (2015).
- [47] Baltussen, E.J., Kok, E.N., de Koning, S.G.B., Sanders, J., Aalbers, A.G., Kok, N.F., Beets, G.L., Flohil, C.C., Bruin, S.C., et al., “Hyperspectral imaging for tissue classification, a way toward smart laparoscopic colorectal surgery,” *Journal of biomedical optics* 24(1), 016002 (2019).
- [48] Deal, J.A., Favreau, P., Weber, D., Rich, T., and Leavesley, S., “Potential of Hyperspectral Imaging for Label-free Tissue and Pathology Classification,” *The FASEB Journal* 30(1 Supplement), 51–2 (2016).
- [49] Lim, H.-T., and Murukeshan, V.M., “A four-dimensional snapshot hyperspectral video-endoscope for bio-imaging applications,” *Scientific Reports* 6(1), 1–10 (2016).
- [50] Leavesley, S.J., Annamdevula, N., Boni, J., Stocker, S., Grant, K., Troyanovsky, B., Rich, T.C., and Alvarez, D.F., “Hyperspectral imaging microscopy for identification and quantitative analysis of fluorescently-labeled cells in highly autofluorescent tissue,” *Journal of biophotonics* 5(1), 67–84 (2012).
- [51] Taruttis, A., and Ntziachristos, V., “Advances in real-time multispectral optoacoustic imaging and its applications,” *Nature Photonics* 9(4), 219–227 (2015).
- [52] Siddiqi, A.M., Li, H., Faruque, F., Williams, W., Lai, K., Hughson, M., Bigler, S., Beach, J., and Johnson, W., “Use of hyperspectral imaging to distinguish normal, precancerous, and cancerous cells,” *Cancer* 114(1), 13–21 (2008).
- [53] Akbari, H., Uto, K., Kosugi, Y., Kojima, K., and Tanaka, N., “Cancer detection using infrared hyperspectral imaging,” *Cancer Science* 102(4), 852–857 (2011).
- [54] Shao, X., Zheng, W., and Huang, Z., “In vivo diagnosis of colonic precancer and cancer using near-infrared autofluorescence spectroscopy and biochemical modeling,” *Journal of biomedical optics* 16(6), 067005 (2011).
- [55] Lu, G., Halig, L.V., Wang, D., Qin, X., Chen, Z.G., and Fei, B., “Spectral-spatial classification for noninvasive cancer detection using hyperspectral imaging,” *Journal of biomedical optics* 19(10), 106004 (2014).

- [56] Lin, D., Feng, S., Pan, J., Chen, Y., Lin, J., Chen, G., Xie, S., Zeng, H., and Chen, R., “Colorectal cancer detection by gold nanoparticle based surface-enhanced Raman spectroscopy of blood serum and statistical analysis,” *Optics Express* 19(14), 13565 (2011).
- [57] Jing Wang, and Chein-I Chang, “Independent component analysis-based dimensionality reduction with applications in hyperspectral image analysis,” *IEEE Transactions on Geoscience and Remote Sensing* 44(6), 1586–1600 (2006).
- [58] Ji, S., Xu, W., Yang, M., and Yu, K., “3D Convolutional Neural Networks for Human Action Recognition,” *IEEE Transactions on Pattern Analysis and Machine Intelligence* 35(1), 221–231 (2013).
- [59] Chen, Y., Jiang, H., Li, C., Jia, X., and Ghamisi, P., “Deep feature extraction and classification of hyperspectral images based on convolutional neural networks,” *IEEE Transactions on Geoscience and Remote Sensing* 54(10), 6232–6251 (2016).
- [60] Karpathy, A., Toderici, G., Shetty, S., Leung, T., Sukthankar, R., and Fei-Fei, L., “Large-Scale Video Classification with Convolutional Neural Networks,” in 2014 *IEEE Conf. Comput. Vis. Pattern Recognit.*, 1725–1732 (2014).
- [61] Simonyan, K., and Zisserman, A., [Two-Stream Convolutional Networks for Action Recognition in Videos] , in *Adv. Neural Inf. Process. Syst.* 27, Z. Ghahramani, M. Welling, C. Cortes, N. D. Lawrence, and K. Q. Weinberger, Eds., Curran Associates, Inc., 568–576 (2014).
- [62] Tran, D., Bourdev, L., Fergus, R., Torresani, L., and Paluri, M., “Learning Spatiotemporal Features with 3D Convolutional Networks,” in 2015 *IEEE Int. Conf. Comput. Vis. ICCV*, 4489–4497 (2015).
- [63] Cervone, H.F., “Applied digital library project management: Using Pugh matrix analysis in complex decision-making situations,” *OCLC Systems & Services: International digital library perspectives* 25(4), 228–232 (2009).
- [64] Guler, K., and Petrisor, D.M., “A Pugh Matrix based product development model for increased small design team efficiency,” *Cogent Engineering* 8(1), 1923383 (2021).
- [65] Georgiadis, D.R., Mazzuchi, T.A., and Sarkani, S., “Using multi criteria decision making in analysis of alternatives for selection of enabling technology,” *Systems Engineering* 16(3), 287–303 (2013).
- [66] Bevilacqua, V., Cassano, F., Mininno, E., and Iacca, G., [Optimizing Feed-Forward Neural Network Topology by Multi-objective Evolutionary Algorithms: A Comparative Study on Biomedical Datasets] , in *Adv. Artif. Life Evol. Comput. Syst. Chem.* 587, F. Rossi, F. Mavelli, P. Stano, and D. Caivano, Eds., Springer International Publishing, Cham, 53–64 (2016).
- [67] Olofsson, S., Mehrian, M., Calandra, R., Geris, L., Deisenroth, M.P., and Misener, R., “Bayesian Multiobjective Optimisation With Mixed Analytical and Black-Box Functions: Application to Tissue Engineering,” *IEEE Transactions on Biomedical Engineering* 66(3), 727–739 (2019).
- [68] Ross, A.M., Rhodes, D.H., and Hastings, D.E., “Defining changeability: Reconciling flexibility, adaptability, scalability, modifiability, and robustness for maintaining system lifecycle value,” *Systems Engineering* 11(3), 246–262 (2008).

- [69] Boehm, B.W., “A spiral model of software development and enhancement,” *Computer* 21(5), 61–72 (1988).
- [70] Hossain, N.U.I., Dayarathna, V.L., Nagahi, M., and Jaradat, R., “Systems thinking: A review and bibliometric analysis,” *Systems* 8(3), 23 (2020).
- [71] Lieberman, D.A., and Garewal, H., “Use of Colonoscopy to Screen Asymptomatic Adults for Colorectal Cancer,” *The New England Journal of Medicine* 7 (2000).
- [72] Levin, B., and Murphy, G.P., “Revision in American Cancer Society recommendations for the early detection of colorectal cancer,” *CA: A Cancer Journal for Clinicians* 42(5), 296–299 (1992).
- [73] Cho, J.-H., “Advanced imaging technology other than narrow band imaging,” *Clinical endoscopy* 48(6), 503 (2015).
- [74] Negreanu, L., Preda, C., Ionescu, D., and Ferechide, D., “Progress in digestive endoscopy: Flexible Spectral Imaging Colour Enhancement (FICE)-technical review,” *Journal of Medicine and Life* 8(4), 416–422 (2015).
- [75] Yung, D.E., Carvalho, P.B., Giannakou, A., Kopylov, U., Rosa, B., Rondonotti, E., Toth, E., Plevris, J.N., and Koulaouzidis, A., “Clinical validity of flexible spectral imaging color enhancement (FICE) in small-bowel capsule endoscopy: a systematic review and meta-analysis,” *Endoscopy* 49(3), 258–269 (2017).
- [76] Blachar, A., and Sosna, J., “CT Colonography (Virtual Colonoscopy): Technique, Indications and Performance,” *Digestion* 76(1), 34–41 (2007).
- [77] Bressler, B., Paszat, L.F., Chen, Z., Rothwell, D.M., Vinden, C., and Rabeneck, L., “Rates of New or Missed Colorectal Cancers After Colonoscopy and Their Risk Factors: A Population-Based Analysis,” *Gastroenterology* 132(1), 96–102 (2007).
- [78] Siegel, R., Desantis, C., and Jemal, A., “Colorectal cancer statistics, 2014,” *CA: a cancer journal for clinicians* 64(2), 104–117 (2014).
- [79] Burke, J.R., Brown, P., Quyn, A., Lambie, H., Tolan, D., and Sagar, P., “Tumour growth rate of carcinoma of the colon and rectum: retrospective cohort study,” *BJS Open* 4(6), 1200–1207 (2020).
- [80] Comroe, J.H., “Retrospectroscope: Insights into medical discovery” (1977).
- [81] Lau, W.Y., Leow, C.K., and Li, A.K.C., “History of Endoscopic and Laparoscopic Surgery,” *World Journal of Surgery* 21(4), 444–453 (1997).
- [82] Berci, G., and Forde, K., “History of endoscopy,” *Surgical endoscopy* 14(1), 5–15 (2000).
- [83] De Groen, P.C., “History of the Endoscope [Scanning Our Past],” *Proceedings of the IEEE* 105(10), 1987–1995 (2017).
- [84] Abbott, R., “History of neuroendoscopy,” *Neurosurgery Clinics of North America* 15(1), 1–7 (2004).
- [85] Achord, J.L., and Muthusamy, V.R., [The History of Gastrointestinal Endoscopy], in *Clin. Gastrointest. Endosc.*, Elsevier, 2-11.e1 (2019).
- [86] Bozzini, P., “Lichtleiter, eine Erfindung zur Anschauung innerer Theile und Krankheiten nebst der Abbildung,” *Journal der practischen Heilkunde, Berlin* 24(1), 107–124 (1806).
- [87] Doglietto, F., Prevedello, D.M., Jane, J.A., Han, J., and Laws, E.R., “A brief history of endoscopic transsphenoidal surgery—from Philipp Bozzini to the First

- World Congress of Endoscopic Skull Base Surgery,” *Neurosurgical Focus* 19(6), 1–6 (2005).
- [88] Mann, G., Bozzini, P., and Bozzini, D., “Der Frankfurter Lichtleiter: Neues über Philipp Bozzini und sein Endoskop,” *Medizinhistorisches Journal* 8(2/3), 105–130 (1973).
- [89] Cecchini, R., and Pelosi, G., “Alessandro Volta and his battery,” *IEEE Antennas and Propagation Magazine* 34(2), 30–37 (1992).
- [90] Chatterjee, S., “Michael Faraday: Discovery of electromagnetic induction,” *Resonance* 7(3), 35–45 (2002).
- [91] Holmes, R., “Humphry Davy and the Chemical Moment,” *Clinical Chemistry* 57(11), 1625–1631 (2011).
- [92] Rue, W.D.L., Muller, H., and Spottiswoode, W., “II. Experiments to ascertain the cause of stratification electrical discharges in vacuo,” *Proceedings of the Royal Society of London* 23(156–163), 356–361 (1875).
- [93] Zajackowski, T., and Zamann, A.P., “Julius Bruck (1840?1902) and his influence on the endoscopy of today,” *World Journal of Urology* 22(4), 293–303 (2004).
- [94] Zissis, G., and Kitsinelis, S., “State of art on the science and technology of electrical light sources: from the past to the future,” *Journal of Physics D: Applied Physics* 42(17), 173001 (2009).
- [95] Chirnside, R.C., “Sir Joseph Swan and the invention of the electric lamp,” *Electronics and Power* 25(2), 96- (1979).
- [96] Spear, B., “Let there be light! Sir Joseph Swan and the incandescent light bulb,” *World Patent Information* 35(1), 38–41 (2013).
- [97] “The Light Bulb, Cystoscopy, and Thomas Alva Edison” (15 July 2022).
- [98] Wise, G., “Innovation: Swan’s way: A study in style: With the birth of the electric light bulb, two modern styles of inventing emerged: Thomas Edison’s and Joseph Swan’s,” *IEEE Spectrum* 19(4), 66–71 (1982).
- [99] Smith, N., “The whole story of... light bulbs,” *Engineering & Technology* 13(9), 54–59 (2018).
- [100] Mouton, W.G., Bessell, J.R., and Maddern, G.J., “Looking Back to the Advent of Modern Endoscopy: 150th Birthday of Maximilian Nitze,” *World Journal of Surgery* 22(12), 1256–1258 (1998).
- [101] Rehnberg, V., and Walters, E., “The life and work of Adolph Kussmaul 1822–1902: ‘Sword swallows in modern medicine,’” *Journal of the Intensive Care Society* 18(1), 71–72 (2017).
- [102] Payne, S., Eardley, I., and O’Flynn, K., Eds., [Imaging and Technology in Urology], Springer London, London (2012).
- [103] Gow, J.G., “HAROLD HOPKINS AND OPTICAL SYSTEMS FOR UROLOGY—AN APPRECIATION”6 (1998).
- [104] Dobson, S.J., and Hopkins, H.H., “A new rod-lens relay system offering improved image quality,” *Journal of Physics E: Scientific Instruments* 22(7), 450–455 (1989).
- [105] Commissioner, O. of the, “FDA History,” FDA, 29 March 2021, <<https://www.fda.gov/about-fda/fda-history>> (22 September 2022).

- [106] Roux, G., and Halstead, J.A., [Issues and trends in nursing] , Jones & Bartlett Learning (2017).
- [107] Shah, J., “Endoscopy through the ages,” *BJU International* 89(7), 645–652 (2002).
- [108] Reuter, M., “The historical development of endophotography,” *World Journal of Urology* 18(4), 299–302 (2000).
- [109] Beer, J.J., “Capitalizing on Invention,” *Science* 192(4240), 658–660 (1976).
- [110] Evans, R.M., “Maxwell’s Color Photograph,” *Scientific American* 205(5), 118–131 (1961).
- [111] Epstein, E., and Tennant, J.A., “Frederic Eugene Ives,” *Journal of Applied Physics* 9(4), 226–236 (1938).
- [112] Nudds, J.R., “The Life and Work of John Joly (1857-1933),” *Irish Journal of Earth Sciences* 8(1), 81–94 (1986).
- [113] Fechet, I., “Jonas Ferdinand Gabriel Lippmann: The pioneer of color photography or primus inter pares,” *Comptes Rendus Chimie* 19(8), 903–908 (2016).
- [114] Leskosky, R.J., “Phenakoscope: 19th Century Science Turned to Animation,” *Film History* 5(2), 176–189 (1993).
- [115] Spehr, P., [The Man Who Made Movies: W.K.L. Dickson] , Indiana University Press (2008).
- [116] Salazard, B., Desouches, C., and Magalon, G., “Auguste and Louis Lumière, inventors at the service of the suffering,” *European Journal of Plastic Surgery* 28(7), 441–447 (2006).
- [117] Berci, G., and Davids, J., “Endoscopy and Television,” *British Medical Journal* 1(5292), 1610–1613 (1962).
- [118] Smith, G.E., “The invention and early history of the CCD,” *Journal of Applied Physics* 109(10), 102421 (2011).
- [119] Fossum, E.R., “The Invention of CMOS Image Sensors: A Camera in Every Pocket,” in 2020 Pan Pac. Microelectron. Symp. Pan Pac., 1–6 (2020).
- [120] Abe, H., “Device technologies for high quality and smaller pixel in CCD and CMOS image sensors,” in *IEDM Tech. Dig. IEEE Int. Electron Devices Meet.* 2004, 989–992 (2004).
- [121] Gouveia, L.C.P., and Choubey, B., “On Evolution of CMOS Image Sensors,” *International Journal on Smart Sensing and Intelligent Systems* 7(5), 1–6 (2014).
- [122] Gouveia, L.C.P., and Choubey, B., “Advances on CMOS image sensors,” *Sensor Review* 36(3), 231–239 (2016).
- [123] Suzuki, T., “Challenges of image-sensor development,” in 2010 IEEE Int. Solid-State Circuits Conf. - ISSCC, 27–30 (2010).
- [124] Liu, Y.T., “REVIEW AND DESIGN A MOBILE PHONE CAMERA LENS FOR 21.4 MEGA” (2017).
- [125] Morrissey, S., [iOS Forensic Analysis for iPhone, iPad, and iPod touch] , Apress, Berkeley, CA (2010).
- [126] Abdallah, S., Saleh, B., and Aboulsoud, A.K., “A general overview of solid state imaging sensors types,” in *Third Workshop Photonics Its Appl.* Egypt. Eng. Fac. Inst. Cat No02EX509, 1–10 (2002).
- [127] Oto, A., “Virtual endoscopy,” *European Journal of Radiology* 42(3), 231–239 (2002).

- [128] Adler, S.N., and Metzger, Y.C., “PillCam COLON capsule endoscopy: recent advances and new insights,” *Therapeutic Advances in Gastroenterology* 4(4), 265–268 (2011).
- [129] Gossum, A.V., Fernandez-Urien, I., Delvaux, M., Neuhaus, H., Riccioni, M.E., Fraser, C., Hagenmuller, F., and Devière, J., “Capsule Endoscopy versus Colonoscopy for the Detection of Polyps and Cancer,” *n engl j med* 7 (2009).
- [130] Azevedo, I.L., Morgan, M.G., and Morgan, F., “The Transition to Solid-State Lighting,” *Proceedings of the IEEE* 97(3), 481–510 (2009).
- [131] Smith, S., “The Scientist & Engineer’s Guide to Digital Signal Processing (California: California Technical Pub)” (1997).
- [132] Tsai, T.-H., Fujimoto, J.G., and Mashimo, H., “Endoscopic optical coherence tomography for clinical gastroenterology,” *diagnostics* 4(2), 57–93 (2014).
- [133] Gaab, M.R., “Instrumentation: Endoscopes and Equipment,” *World Neurosurgery* 79(2), S14.e11-S14.e21 (2013).
- [134] Swain, P., “Role of video endoscopy in managing small bowel disease,” *Gut* 53(12), 1866–1875 (2004).
- [135] Iakovidis, D.K., “Software engineering applications in gastroenterology,” *Global Journal of Gastroenterology & Hepatology* 2(1), 11–18 (2014).
- [136] van der Sommen, F., de Groof, J., Struyvenberg, M., van der Putten, J., Boers, T., Fockens, K., Schoon, E.J., Curvers, W., de With, P., et al., “Machine learning in GI endoscopy: practical guidance in how to interpret a novel field,” *Gut* 69(11), 2035–2045 (2020).
- [137] Hounnou, G., Destrieux, C., Desme, J., Bertrand, P., and Velut, S., “Anatomical study of the length of the human intestine,” *Surgical and radiologic anatomy* 24(5), 290–294 (2002).
- [138] Soulas, A., Dubois De Montreynaud, J.M., Edwards, R.J., and Gladu, A.J., “Bronchoscopy and Television,” *Diseases of the Chest* 31(5), 580–584 (1957).
- [139] Berci, G., Shulman, A., Morgenstern, L., Paz-Partlow, M., Cuschieri, A., and Wood, R., “Television choledochoscopy,” *Surgery, gynecology & obstetrics* 160(2), 176–177 (1985).
- [140] Baillie, J., “The endoscope,” *Gastrointestinal Endoscopy* 65(6), 886–893 (2007).
- [141] Jacobson, M.C., White, R.W. deVere, and Demos, S.G., “In vivo testing of a prototype system providing simultaneous white light and near infrared autofluorescence image acquisition for detection of bladder cancer,” *Journal of biomedical optics* 17(3), 036011 (2012).
- [142] McWade, M.A., Paras, C., White, L.M., Phay, J.E., Solórzano, C.C., Broome, J.T., and Mahadevan-Jansen, A., “Label-free Intraoperative Parathyroid Localization With Near-Infrared Autofluorescence Imaging,” *The Journal of Clinical Endocrinology & Metabolism* 99(12), 4574–4580 (2014).
- [143] Iseki, K., Tatsuta, M., Iishi, H., Sakai, N., Yano, H., and Ishiguro, S., “Effectiveness of the near-infrared electronic endoscope for diagnosis of the depth of involvement of gastric cancers,” *Gastrointestinal Endoscopy* 52(6), 755–762 (2000).
- [144] Ortiz-Fernandez-Sordo, J., Sami, S.S., Mansilla-Vivar, R., Subramanian, V., Mannath, J., Telakis, E., and Ragunath, K., “Evaluation of a novel infra-red

- endoscopy system in the assessment of early neoplasia in Barretts esophagus: pilot study from a single center,” *Diseases of the Esophagus* 31(3), dox137 (2018).
- [145] Betz, C.S., Stepp, H., Janda, P., Arbogast, S., Grevers, G., Baumgartner, R., and Leunig, A., “A comparative study of normal inspection, autofluorescence and 5-ALA-induced PPIX fluorescence for oral cancer diagnosis,” *International Journal of Cancer* 97(2), 245–252 (2002).
- [146] Zhao, H.L., Zhang, C.P., Zhu, H., Jiang, Y.F., and Fu, X.B., “Autofluorescence of collagen fibres in scar,” *Skin Research and Technology* 23(4), 588–592 (2017).
- [147] Deal, J., Mayes, S., Browning, C., Hill, S., Rider, P., Boudreaux, C., Rich, T.C., and Leavesley, S.J., “Identifying molecular contributors to autofluorescence of neoplastic and normal colon sections using excitation-scanning hyperspectral imaging,” *Journal of Biomedical Optics* 24(2), 021207 (2018).
- [148] Takeuchi, Y., Hanaoka, N., Hanafusa, M., Ishihara, R., Higashino, K., Iishi, H., and Uedo, N., “Autofluorescence imaging of early colorectal cancer,” *Journal of Biophotonics* 4(7–8), 490–497 (2011).
- [149] Bae, S.-J., Lee, D.-S., Berezin, V., Kang, U., and Lee, K.-H., “Multispectral autofluorescence imaging for detection of cervical lesions: A preclinical study,” *Journal of Obstetrics and Gynaecology Research* 42(12), 1846–1853 (2016).
- [150] Chen, W., Gao, X., Tian, Q., and Chen, L., “A comparison of autofluorescence bronchoscopy and white light bronchoscopy in detection of lung cancer and preneoplastic lesions: a meta-analysis,” *Lung Cancer* 73(2), 183–188 (2011).
- [151] Falk, G.W., “Autofluorescence endoscopy,” *Gastrointestinal endoscopy clinics of North America* 19(2), 209–220 (2009).
- [152] Becker, A., Hessenius, C., Licha, K., Ebert, B., Sukowski, U., Semmler, W., Wiedenmann, B., and Grötzinger, C., “Receptor-targeted optical imaging of tumors with near-infrared fluorescent ligands,” *Nature biotechnology* 19(4), 327–331 (2001).
- [153] Guo, Z., Park, S., Yoon, J., and Shin, I., “Recent progress in the development of near-infrared fluorescent probes for bioimaging applications,” *Chem. Soc. Rev.* 43(1), 16–29 (2014).
- [154] “Definition of -SCOPY,” <<https://www.merriam-webster.com/dictionary/-scopy>> (24 September 2020).
- [155] Higashi, R., Uraoka, T., Kato, J., Kuwaki, K., Ishikawa, S., Saito, Y., Matsuda, T., Ikematsu, H., Sano, Y., et al., “Diagnostic accuracy of narrow-band imaging and pit pattern analysis significantly improved for less-experienced endoscopists after an expanded training program,” *Gastrointestinal Endoscopy* 72(1), 127–135 (2010).
- [156] Ignjatovic, A., Thomas-Gibson, S., East, J.E., Haycock, A., Bassett, P., Bhandari, P., Man, R., Suzuki, N., and Saunders, B.P., “Development and validation of a training module on the use of narrow-band imaging in differentiation of small adenomas from hyperplastic colorectal polyps,” *Gastrointestinal Endoscopy* 73(1), 128–133 (2011).
- [157] Andolfi, M., Potenza, R., Capozzi, R., Liparulo, V., Puma, F., and Yasufuku, K., “The role of bronchoscopy in the diagnosis of early lung cancer: a review,” *Journal of thoracic disease* 8(11), 3329 (2016).

- [158] Asano, F., “Advanced bronchoscopy for the diagnosis of peripheral pulmonary lesions,” *Respiratory investigation* 54(4), 224–229 (2016).
- [159] Sato, R., Fujiya, M., Watari, J., Ueno, N., Moriichi, K., Kashima, S., Maeda, S., Ando, K., Kawabata, H., et al., “The diagnostic accuracy of high-resolution endoscopy, autofluorescence imaging and narrow-band imaging for differentially diagnosing colon adenoma,” *Endoscopy* 43(10), 862–868 (2011).
- [160] Talens, P., Mora, L., Morsy, N., Barbin, D.F., ElMasry, G., and Sun, D.-W., “Prediction of water and protein contents and quality classification of Spanish cooked ham using NIR hyperspectral imaging,” *Journal of Food Engineering* 117(3), 272–280 (2013).
- [161] Panasyuk, S.V., Yang, S., Faller, D.V., Ngo, D., Lew, R.A., Freeman, J.E., and Rogers, A.E., “Medical hyperspectral imaging to facilitate residual tumor identification during surgery,” *Cancer Biology & Therapy* 6(3), 439–446 (2007).
- [162] Zuzak, K.J., Francis, R.P., Wehner, E.F., Litorja, M., Cadeddu, J.A., and Livingston, E.H., “Active DLP Hyperspectral Illumination: A Noninvasive, in Vivo, System Characterization Visualizing Tissue Oxygenation at Near Video Rates,” *Analytical Chemistry* 83(19), 7424–7430 (2011).
- [163] Ortega, S., Fabelo, H., Iakovidis, D.K., Koulaouzidis, A., and Callico, G.M., “Use of hyperspectral/multispectral imaging in gastroenterology. Shedding some–different–light into the dark,” *Journal of clinical medicine* 8(1), 36 (2019).
- [164] Lin, J., Clancy, N.T., Qi, J., Hu, Y., Tatla, T., Stoyanov, D., Maier-Hein, L., and Elson, D.S., “Dual-modality endoscopic probe for tissue surface shape reconstruction and hyperspectral imaging enabled by deep neural networks,” *Medical Image Analysis* 48, 162–176 (2018).
- [165] Martin, M.E., Wabuye, M.B., Chen, K., Kasili, P., Panjehpour, M., Phan, M., Overholt, B., Cunningham, G., Wilson, D., et al., “Development of an advanced hyperspectral imaging (HSI) system with applications for cancer detection,” *Annals of biomedical engineering* 34(6), 1061–1068 (2006).
- [166] Kester, R.T., Bedard, N., Gao, L., and Tkaczyk, T.S., “Real-time snapshot hyperspectral imaging endoscope,” *Journal of biomedical optics* 16(5), 056005–056005 (2011).
- [167] Goto, A., Nishikawa, J., Kiyotoki, S., Nakamura, M., Nishimura, J., Okamoto, T., Ogihara, H., Fujita, Y., Hamamoto, Y., et al., “Use of hyperspectral imaging technology to develop a diagnostic support system for gastric cancer,” *Journal of biomedical optics* 20(1), 016017 (2015).
- [168] Schaefer, P.M., Kalinina, S., Rueck, A., Arnim, C.A.F. von, and Einem, B. von, “NADH Autofluorescence—A Marker on its Way to Boost Bioenergetic Research,” *Cytometry Part A* 95(1), 34–46 (2019).
- [169] Fjeld, C.C., Birdsong, W.T., and Goodman, R.H., “Differential binding of NAD⁺ and NADH allows the transcriptional corepressor carboxyl-terminal binding protein to serve as a metabolic sensor,” *Proceedings of the National Academy of Sciences* 100(16), 9202–9207 (2003).
- [170] Puchtler, H., Waldrop, F.S., and Valentine, L.S., “Fluorescence microscopic distinction between elastin and collagen,” *Histochemie* 35(1), 17–30 (1973).

- [171] Fang, M., Yuan, J., Peng, C., and Li, Y., “Collagen as a double-edged sword in tumor progression,” *Tumour Biology* 35(4), 2871–2882 (2014).
- [172] Skala, M.C., Riching, K.M., Gendron-Fitzpatrick, A., Eickhoff, J., Eliceiri, K.W., White, J.G., and Ramanujam, N., “In vivo multiphoton microscopy of NADH and FAD redox states, fluorescence lifetimes, and cellular morphology in precancerous epithelia,” *Proceedings of the National Academy of Sciences* 104(49), 19494–19499 (2007).
- [173] Favreau, P.F., Deal, J.A., Weber, D.A., Rich, T.C., and Leavesley, S.J., “Assessment of autofluorescent signatures in multiple tissue types with novel excitation-scanning hyperspectral imaging,” *The FASEB Journal* 30(1 Supplement), 51–1 (2016).
- [174] Favreau, P.F., Hernandez, C., Heaster, T., Alvarez, D.F., Rich, T.C., Prabhat, P., and Leavesley, S.J., “Excitation-scanning hyperspectral imaging microscope,” *Journal of biomedical optics* 19(4), 046010–046010 (2014).
- [175] Leavesley, S.J., Walters, M., Lopez, C., Baker, T., Favreau, P.F., Rich, T.C., Rider, P.F., and Boudreaux, C.W., “Hyperspectral imaging fluorescence excitation scanning for colon cancer detection,” *Journal of Biomedical Optics* 21(10), 104003–104003 (2016).
- [176] Shrestha, R., and Hardeberg, J., “Multispectral imaging using LED illumination and an RGB camera,” *Color and Imaging Conference* (2013).
- [177] Parmar, M., Lansel, S., and Farrell, J., “An LED-based lighting system for acquiring multispectral scenes,” *Proceedings of SPIE - The International Society for Optical Engineering* 8299, 23 (2012).
- [178] Galbán, J., Sanz-Vicente, I., Navarro, J., and de Marcos, S., “The intrinsic fluorescence of FAD and its application in analytical chemistry: a review,” *Methods and Applications in Fluorescence* 4(4), 042005 (2016).
- [179] Morgan, R., Barton, J.S., Harper, P.G., and Jones, J.D.C., “Wavelength dependence of bending loss in monomode optical fibers: effect of the fiber buffer coating,” *Optics Letters* 15(17), 947 (1990).
- [180] van Eijkelenborg, M., Canning, J., Ryan, T., and Lyytikainen, K., “Bending-induced colouring in a photonic crystal fibre,” *Optics Express* 7(2), 88 (2000).
- [181] Landgrebe, D.A., “Multispectral land sensing: where from, where to?,” *IEEE Transactions on Geoscience and Remote Sensing* 43(3), 414–421 (2005).
- [182] Schott, J.R., [Remote sensing: the image chain approach] , Oxford University Press on Demand (2007).
- [183] Wang, L., Jin, J., Song, Z., Wang, J., Zhang, L., Rehman, T.U., Ma, D., Carpenter, N.R., and Tuinstra, M.R., “LeafSpec: An accurate and portable hyperspectral corn leaf imager,” *Computers and Electronics in Agriculture* 169, 105209 (2020).
- [184] ElMasry, G., and Wold, J.P., “High-Speed Assessment of Fat and Water Content Distribution in Fish Fillets Using Online Imaging Spectroscopy,” *Journal of Agricultural and Food Chemistry* 56(17), 7672–7677 (2008).
- [185] ElMasry, G., Sun, D.-W., and Allen, P., “Near-infrared hyperspectral imaging for predicting colour, pH and tenderness of fresh beef,” *Journal of Food Engineering* 110(1), 127–140 (2012).

- [186] Li, Q., He, X., Wang, Y., Liu, H., Xu, D., and Guo, F., “Review of spectral imaging technology in biomedical engineering: achievements and challenges,” *Journal of biomedical optics* 18(10), 100901 (2013).
- [187] Favreau, P.F., Deal, J.A., Harris, B., Weber, D.S., Rich, T.C., and Leavesley, S.J., “Label-free spectroscopic tissue characterization using fluorescence excitation-scanning spectral imaging,” *Journal of Biophotonics* 13(2), e201900183 (2020).
- [188] Fei, B., [Hyperspectral imaging in medical applications] , in *Data Handl. Sci. Technol.* 32, Elsevier, 523–565 (2020).
- [189] Browning, C.M., Deal, J., Mayes, S., Arshad, A., Rich, T.C., and Leavesley, S.J., “Excitation-scanning hyperspectral video endoscopy: enhancing the light at the end of the tunnel,” *Biomedical Optics Express* 12(1), 247 (2021).
- [190] Michael Ebner, Nabavi, E., Shapey, J., Xie, Y., Liebmann, F., Spirig, J.M., Hoch, A., Farshad, M., Saeed, S.R., et al., “Intraoperative hyperspectral label-free imaging: from system design to first-in-patient translation,” *Journal of Physics D: Applied Physics* 54(29), 294003 (2021).
- [191] Cutrale, F., Trivedi, V., Trinh, L.A., Chiu, C.-L., Choi, J.M., Artiga, M.S., and Fraser, S.E., “Hyperspectral phasor analysis enables multiplexed 5D in vivo imaging,” *Nature methods* 14(2), 149–152 (2017).
- [192] Annamdevula, N.S., Sweat, R., Griswold, J.R., Trinh, K., Hoffman, C., West, S., Deal, J., Britain, A.L., Jalink, K., et al., “Spectral imaging of FRET-based sensors reveals sustained cAMP gradients in three spatial dimensions,” *Cytometry Part A* 93(10), 1029–1038 (2018).
- [193] Leavesley, S.J., Britain, A.L., Cichon, L.K., Nikolaev, V.O., and Rich, T.C., “Assessing FRET using spectral techniques,” *Cytometry Part A* 83(10), 898–912 (2013).
- [194] Levy, S., Wilms, C.D., Brumer, E., Kahn, J., Pnueli, L., Arava, Y., Eilers, J., and Gitler, D., “SpRET: Highly Sensitive and Reliable Spectral Measurement of Absolute FRET Efficiency,” *Microscopy and Microanalysis* 17(2), 176–190 (2011).
- [195] Zimmermann, T., Rietdorf, J., and Pepperkok, R., *FEBS letters* 546(1), 87–92 (2003).
- [196] Leavesley, S.J., Annamdevula, N., Boni, J., Stocker, S., Grant, K., Troyanovsky, B., Rich, T.C., and Alvarez, D.F., “HyperSpectral imaging microscopy for identification and quantitative analysis of fluorescently-labeled cells in highly autofluorescent tissue,” *Journal of biophotonics* 5(1), 67 (2012).
- [197] Mansfield, J.R., Gossage, K.W., Hoyt, C.C., and Levenson, R.M., “Autofluorescence removal, multiplexing, and automated analysis methods for in-vivo fluorescence imaging,” *Journal of biomedical optics* 10(4), 041207 (2005).
- [198] Giannoni, L., Lange, F., Sajic, M., Smith, K.J., and Tachtsidis, I., “A Hyperspectral Imaging System for Mapping Haemoglobin and Cytochrome-c-Oxidase Concentration Changes in the Exposed Cerebral Cortex,” *IEEE Journal of Selected Topics in Quantum Electronics* 27(4), 1–11 (2021).
- [199] Okubo, K., Kitagawa, Y., Hosokawa, N., Umezawa, M., Kamimura, M., Kamiya, T., Ohtani, N., and Soga, K., “Visualization of quantitative lipid distribution in

- mouse liver through near-infrared hyperspectral imaging,” *Biomedical Optics Express* 12(2), 823 (2021).
- [200] Felli, E., Al-Taher, M., Collins, T., Baiocchini, A., Felli, E., Barberio, M., Ettore, G.M., Mutter, D., Lindner, V., et al., “Hyperspectral evaluation of hepatic oxygenation in a model of total vs. arterial liver ischaemia,” *Scientific Reports* 10(1), 15441 (2020).
- [201] Garini, Y., Young, I.T., and McNamara, G., “Spectral imaging: principles and applications,” *Cytometry Part A* 69(8), 735–747 (2006).
- [202] Khan, M.J., Khan, H.S., Yousaf, A., Khurshid, K., and Abbas, A., “Modern Trends in Hyperspectral Image Analysis: A Review,” *IEEE Access* 6, 14118–14129 (2018).
- [203] Renkoski, T.E., Utzinger, U., and Hatch, K.D., “Wide-field spectral imaging of human ovary autofluorescence and oncologic diagnosis via previously collected probe data,” *Journal of biomedical optics* 17(3), 036003 (2012).
- [204] Park, K.S., Kim, D.U., Lee, J., Kim, G.H., and Chang, K.S., “Simultaneous multicolor imaging of wide-field epi-fluorescence microscopy with four-bucket detection,” *Biomedical Optics Express* 7(6), 2285 (2016).
- [205] Favreau, P., Hernandez, C., Lindsey, A.S., Alvarez, D.F., Rich, T., Prabhat, P., and Leavesley, S.J., “Thin-film tunable filters for hyperspectral fluorescence microscopy,” *Journal of biomedical optics* 19(1), 011017–011017 (2014).
- [206] St-Georges-Robillard, A., Masse, M., Cahuzac, M., Strupler, M., Patra, B., Orimoto, A.M., Kendall-Dupont, J., Péant, B., Mes-Masson, A.-M., et al., “Fluorescence hyperspectral imaging for live monitoring of multiple spheroids in microfluidic chips,” *The Analyst* 143(16), 3829–3840 (2018).
- [207] Choi, H., Wadduwage, D., Matsudaira, P.T., and So, P.T.C., “Depth resolved hyperspectral imaging spectrometer based on structured light illumination and Fourier transform interferometry,” *Biomedical Optics Express* 5(10), 3494 (2014).
- [208] Sinclair, M.B., Haaland, D.M., Timlin, J.A., and Jones, H.D., “Hyperspectral confocal microscope,” *Applied optics* 45(24), 6283–6291 (2006).
- [209] Vermaas, W.F., Timlin, J.A., Jones, H.D., Sinclair, M.B., Nieman, L.T., Hamad, S.W., Melgaard, D.K., and Haaland, D.M., “In vivo hyperspectral confocal fluorescence imaging to determine pigment localization and distribution in cyanobacterial cells,” *Proceedings of the National Academy of Sciences* 105(10), 4050–4055 (2008).
- [210] Zhang, Y., Haskins, C., Lopez-Cruzan, M., Zhang, J., Centonze, V.E., and Herman, B., “Detection of Mitochondrial Caspase Activity in Real Time *In Situ* in Live Cells,” *Microscopy and Microanalysis* 10(4), 442–448 (2004).
- [211] Zucker, R.M., Rigby, P., Clements, I., Salmon, W., and Chua, M., “Reliability of confocal microscopy spectral imaging systems: Use of multispectral beads,” *Cytometry Part A* 71A(3), 174–189 (2007).
- [212] Chen, K., Yan, R., Xiang, L., and Xu, K., “Excitation spectral microscopy for highly multiplexed fluorescence imaging and quantitative biosensing,” *Light: Science & Applications* 10(1), 97 (2021).
- [213] Lohumi, S., Cho, B.-K., and Hong, S., “LCTF-based multispectral fluorescence imaging: System development and potential for real-time foreign object detection

- in fresh-cut vegetable processing,” *Computers and Electronics in Agriculture* 180, 105912 (2021).
- [214] Bartczak, P., Iso-Mustajarvi, M., Vrzakova, H., Bednarik, R., Fraunberg, M., and Elomaa, A.-P., “A Portable System for On-Site Medical Spectral Imaging: Pre-Clinical Development and Early Evaluation,” in 2018 IEEE 31st Int. Symp. Comput.-Based Med. Syst. CBMS, 256–261 (2018).
- [215] Poudel, C., and Kaminski, C.F., “Supercontinuum radiation in fluorescence microscopy and biomedical imaging applications,” *JOSA B* 36(2), A139–A153 (2019).
- [216] Luo, J., Zhang, H., Forsberg, E., Hou, S., Li, S., Xu, Z., Chen, X., Sun, X., and He, S., “Confocal hyperspectral microscopic imager for the detection and classification of individual microalgae,” *Optics Express* 29(23), 37281 (2021).
- [217] Zhang, S., Xin Cheng, J.Y., Chua, J.J., and Olivo, M., “Characterization of Quantum Dots with Hyperspectral Fluorescence Microscopy for Multiplexed Optical Imaging of Biomolecules,” preprint, *Bioengineering* (2022).
- [218] “Fluorescence Microscopy | LED Illuminators,” CoolLED, <<https://www.coolled.com/>> (14 April 2022).
- [219] Bradter, U., O’Connell, J., Kunin, W.E., Boffey, C.W.H., Ellis, R.J., and Benton, T.G., “Classifying grass-dominated habitats from remotely sensed data: The influence of spectral resolution, acquisition time and the vegetation classification system on accuracy and thematic resolution,” *Science of The Total Environment* 711, 134584 (2020).
- [220] Annamdevula, N.S., Sweat, B., Favreau, P., Lindsey, A.S., Alvarez, D.F., Rich, T.C., and Leavesley, S.J., “An approach for characterizing and comparing hyperspectral microscopy systems,” *Sensors* 13(7), 9267–9293 (2013).
- [221] Shao, H., Li, S., Watkins, S.C., and Wells, A., “ α -Actinin-4 Is Required for Amoeboid-type Invasiveness of Melanoma Cells,” *Journal of Biological Chemistry* 289(47), 32717–32728 (2014).
- [222] Thakore, P., Pritchard, H.A., Griffin, C.S., Yamasaki, E., Drumm, B.T., Lane, C., Sanders, K.M., Feng Earley, Y., and Earley, S., “TRPML1 channels initiate Ca²⁺ sparks in vascular smooth muscle cells,” *Science signaling* 13(637), eaba1015 (2020).
- [223] Sutherland, V.L., Timlin, J.A., Nieman, L.T., Guzowski, J.F., Chawla, M.K., Worley, P.F., Roysam, B., McNaughton, B.L., Sinclair, M.B., et al., “Advanced imaging of multiple mRNAs in brain tissue using a custom hyperspectral imager and multivariate curve resolution,” *Journal of Neuroscience Methods* 160(1), 144–148 (2007).
- [224] Valm, A.M., Cohen, S., Legant, W.R., Melunis, J., Hershberg, U., Wait, E., Cohen, A.R., Davidson, M.W., Betzig, E., et al., “Applying systems-level spectral imaging and analysis to reveal the organelle interactome,” *Nature* 546(7656), 162–167 (2017).
- [225] Bares, A.J., Mejooli, M.A., Pender, M.A., Leddon, S.A., Tilley, S., Lin, K., Dong, J., Kim, M., Fowell, D.J., et al., “Hyperspectral multiphoton microscopy for in vivo visualization of multiple, spectrally overlapped fluorescent labels,” *Optica* 7(11), 1587 (2020).

- [226] Leavesley, S.J., Sweat, B., Abbott, C., Favreau, P., and Rich, T.C., “A theoretical-experimental methodology for assessing the sensitivity of biomedical spectral imaging platforms, assays, and analysis methods,” *Journal of Biophotonics* 11(1), e201600227 (2018).
- [227] Mayes, S.G., Mayes, S.A., Browning, C., Parker, M., Rich, T.C., and Leavesley, S.J., “A spherical mirror-based illumination system for fluorescence excitation-scanning hyperspectral imaging,” presented at *Imaging, Manipulation, and Analysis of Biomolecules, Cells, and Tissues XVII*, 2019, 108810N.
- [228] Wurm, C.A., Neumann, D., Schmidt, R., Egner, A., and Jakobs, S., [Sample Preparation for STED Microscopy] , in *Live Cell Imaging 591*, D. B. Papkovsky, Ed., Humana Press, Totowa, NJ, 185–199 (2010).
- [229] “BioImaging and BioSystems | University of South Alabama,” <<https://www.southalabama.edu/centers/bioimaging/>> (18 May 2022).
- [230] Gao, L., Shao, L., Higgins, C.D., Poulton, J.S., Peifer, M., Davidson, M.W., Wu, X., Goldstein, B., and Betzig, E., “Noninvasive imaging beyond the diffraction limit of 3D dynamics in thickly fluorescent specimens,” *Cell* 151(6), 1370–1385 (2012).
- [231] Demos, S.G., Gandour-Edwards, R., Ramsamooj, R., and de Vere White, R., “Near-infrared autofluorescence imaging for detection of cancer,” *Journal of biomedical optics* 9(3), 587–592 (2004).
- [232] Wang, Q., Xu, J., Geng, R., Cai, J., Li, J., Xie, C., Tang, W., Shen, Q., Huang, W., et al., “High performance one-for-all phototheranostics: NIR-II fluorescence imaging guided mitochondria-targeting phototherapy with a single-dose injection and 808 nm laser irradiation,” *Biomaterials* 231, 119671 (2020).

APPENDICES

Appendix A: Supplemental Document 1

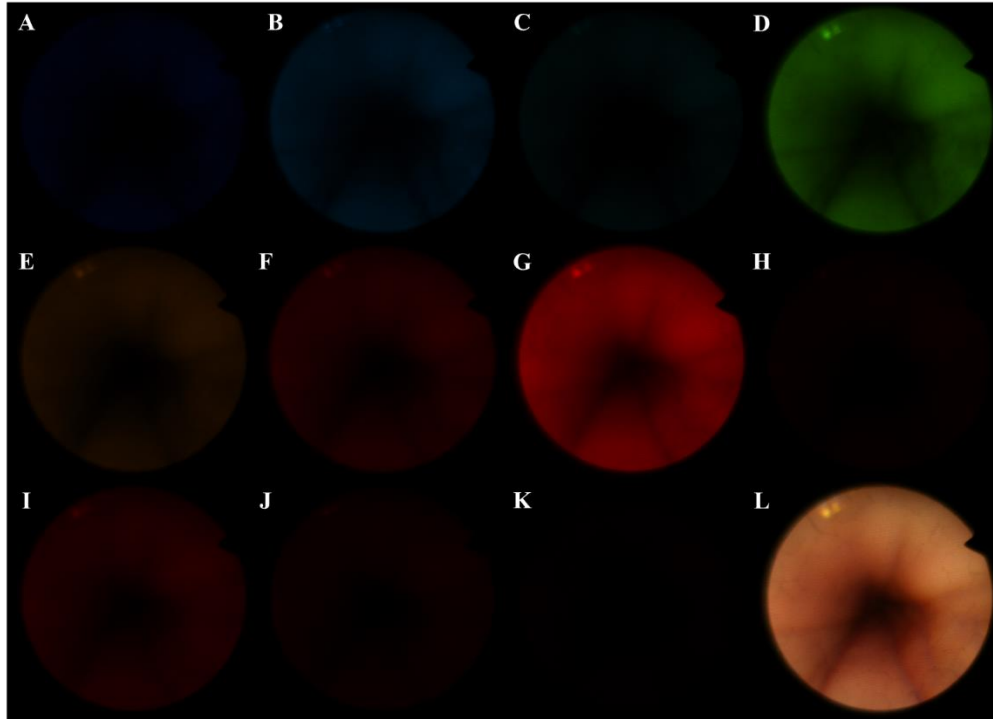


Figure A1. Image data corresponding to Figure 13.E where reflectance spectral images have been divided by wavelength band and false colored for visualization. The channels are presented in respective wavelength order: (A) 450 nm, (B) 470 nm, (C) 490 nm, (D) 525 nm, (E) 590 nm, (F) 620 nm, (G) 670 nm, (H) 680 nm, (I) 750 nm, (J) 810 nm, (K) 850 nm and (L) the overlaid image as seen in Figure 13.E. The 940 nm channel was omitted due to indiscernible signal and increased noise collected. False-coloring was applied using the wavelength coloring function in NIS Elements software; hence the near-infrared wavelengths have all been false-colored at the maximum wavelength (800 nm) available. Each channel look up table (LUT) was uniformly scaled to increase intensity while displaying which channels produced a higher reflectance signal.

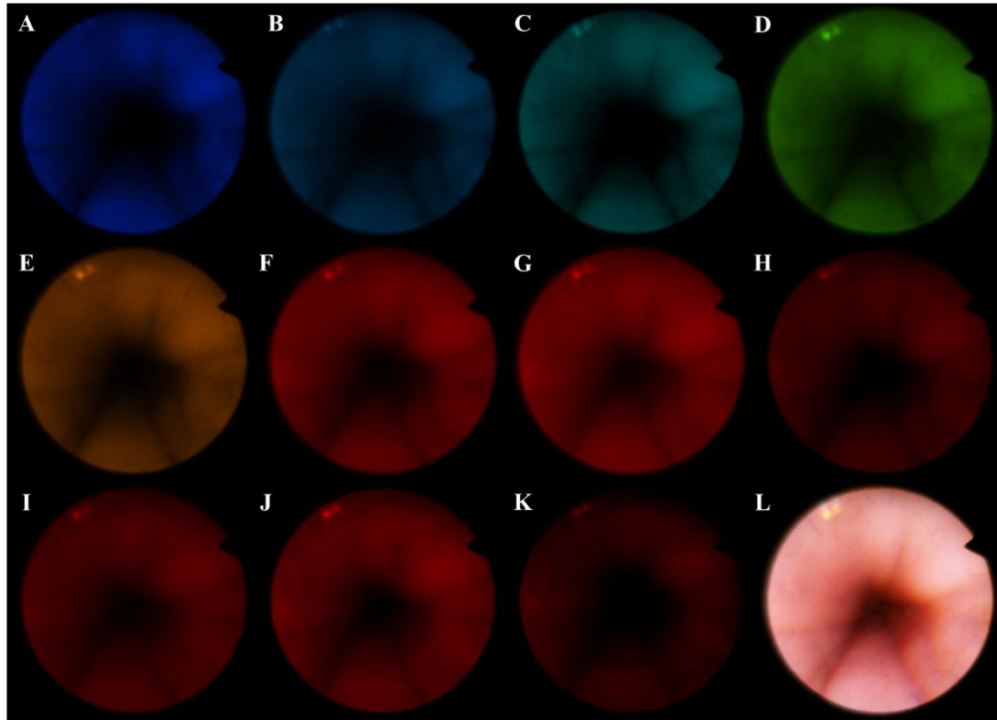


Figure A2. Data from Figure A1 and corresponding Figure 13.E, where the look-up table for each wavelength band has been scaled independently. The channels are presented in respective wavelength order: (A) 450 nm, (B) 470 nm, (C) 490 nm, (D) 525 nm, (E) 590 nm, (F) 620 nm, (G) 670 nm, (H) 680 nm, (I) 750 nm, (J) 810 nm, (K) 850 nm and (L) the overlaid image as seen in Figure 13.E. The 940 nm channel was omitted due to indiscernible signal and increased noise collected. False-coloring was applied using the wavelength coloring function in NIS Elements software; hence the near-infrared wavelengths have all been false-colored at the maximum wavelength (800 nm) available. Channel look up tables (LUT) were individually scaled to display each channel for visual clarity (i.e., the min and max intensity levels to map to the color look-up table were adjusted on a per-channel basis to enhance visualization of each channel). Enhanced contrast can be seen by vasculature in the blue and green channels.

Appendix B: Supplemental Document 2

Table A1. Product specifications for the LEDs used in prototype light source

| Product # | Viewing Angle (°) | Bandwidth (nm) | Total Radiated Power (mW) |
|---------------|-------------------|----------------|---------------------------|
| SMB1N-365V-02 | 18 | 9 | 640 |
| SMB1N-375V-02 | 18 | 11 | 560 |
| SMB1N-385V-02 | 20 | 11 | 720 |
| SMB1N-395V-02 | 22 | 12 | 750 |
| SMB1N-405V-02 | 20 | 14 | 710 |
| SMB1N-415H-02 | 22 | 15 | 300 |
| SMB1N-420H-02 | 36 | 13 | 420 |
| SMB1N-430H-02 | 22 | 15 | 500 |
| SMB1N-D450-02 | 22 | 20 | 480 |
| SMB1N-D470-02 | 20 | 20 | 470 |
| SMB1N-490H-02 | 22 | 26 | 240 |
| SMB1N-515V-02 | 18 | 29 | 250 |
| SMB1N-525V-02 | 22 | 35 | 230 |

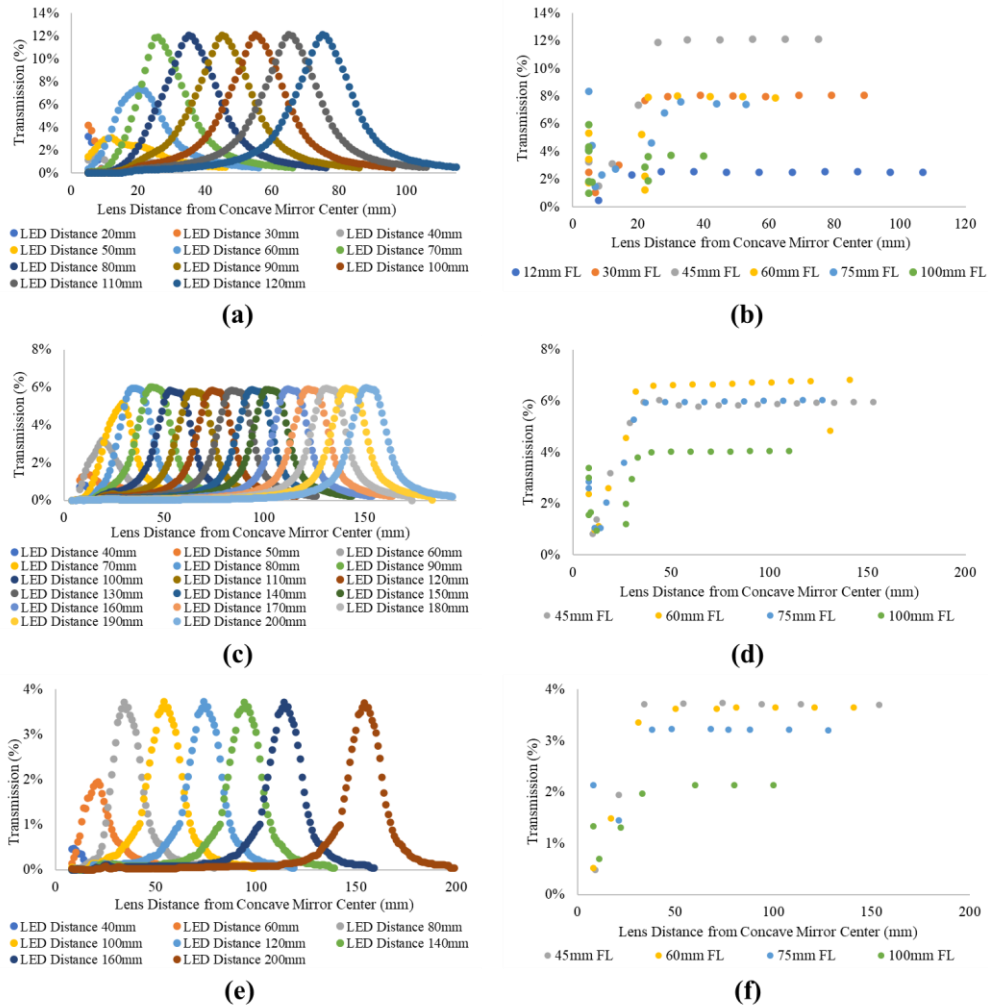


Figure A3. Summary of the TracePro simulation irradiance data for a one lens configuration. These data represent one iteration using a 45 mm FL lens and a 76.2 mm FL concave mirror. (a) Each curve represents a LED position in the model and each data point on the respective curve represents a lens position, both with respect to the z-axis origin of the model. Video representation of the simulation data collection can be seen in Visualization 1. (b) The maximum output for each lens evaluated (see Table 8 in main text) and a 76.2 mm FL concave mirror was plotted with respect to the lens position to summarize the data and allow identification of optimal parameters. Therefore, the 45 mm dataset (grey line and marker) of the right column is the trend of the maximum output for each dataset of the left column. (c) Representative data are also shown for a 114.3 mm FL concave mirror with 45 mm FL lens and (e) 152.4 mm FL concave mirror with 45 mm FL lens and (d) maximal output summarized for all lenses evaluated for the 114.3 mm FL mirror and (f) 152.4 mm FL mirror.

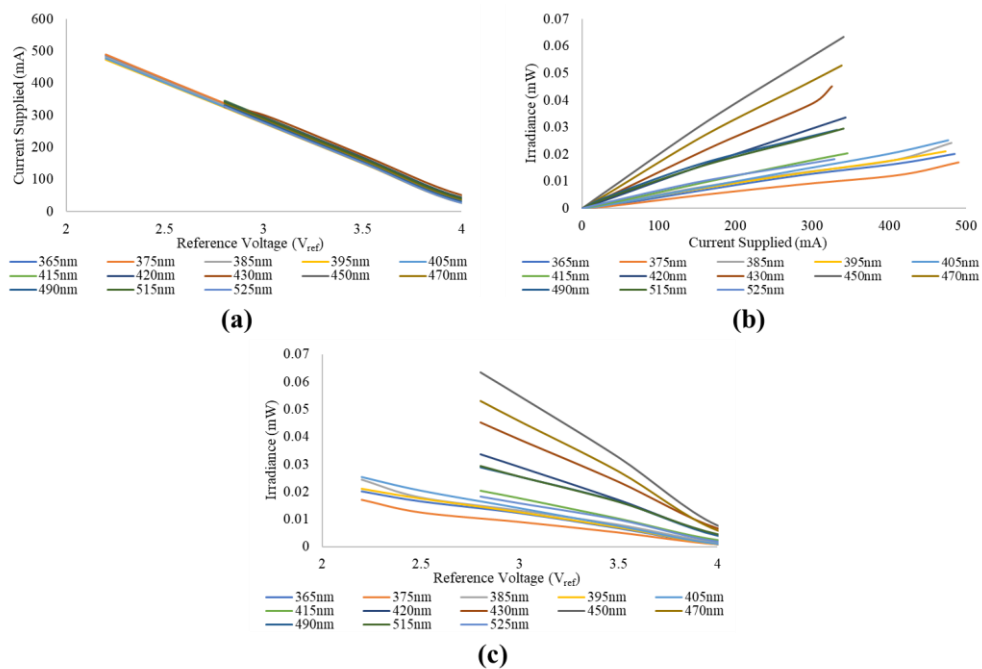


Figure A4. LED measurements for irradiance control. (a) Measured current supplied to individual LEDs based on the software input reference voltage (V_{ref}). (b) Irradiance measurements with respect to the current supplied and (c) with respect to the software inputs.

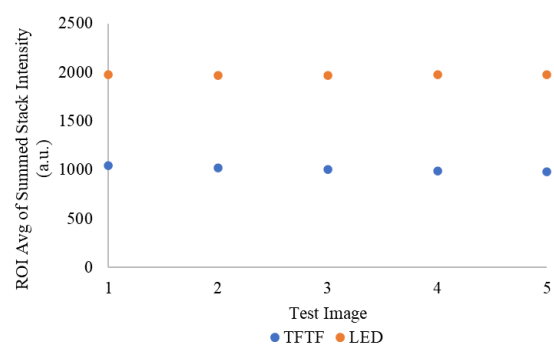


Figure A5. Test for photobleaching on the TFTF-based system and the LED-based system for repeated imaging (5x) of the same FOV. The wavelength summed fluorescence for a selected ROI is plotted as a function of image number.

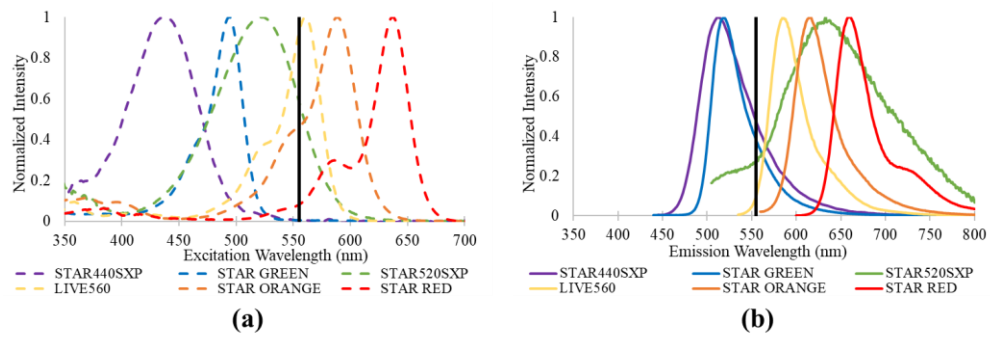


Figure A6. Manufacturer-supplied spectral data for the labels used for the labels used in this study. Data are separated into (a) excitation spectrum and (b) emission spectrum for each respective label. The black line represents the dichroic cut-off wavelength used to separate excitation from fluorescence emission.

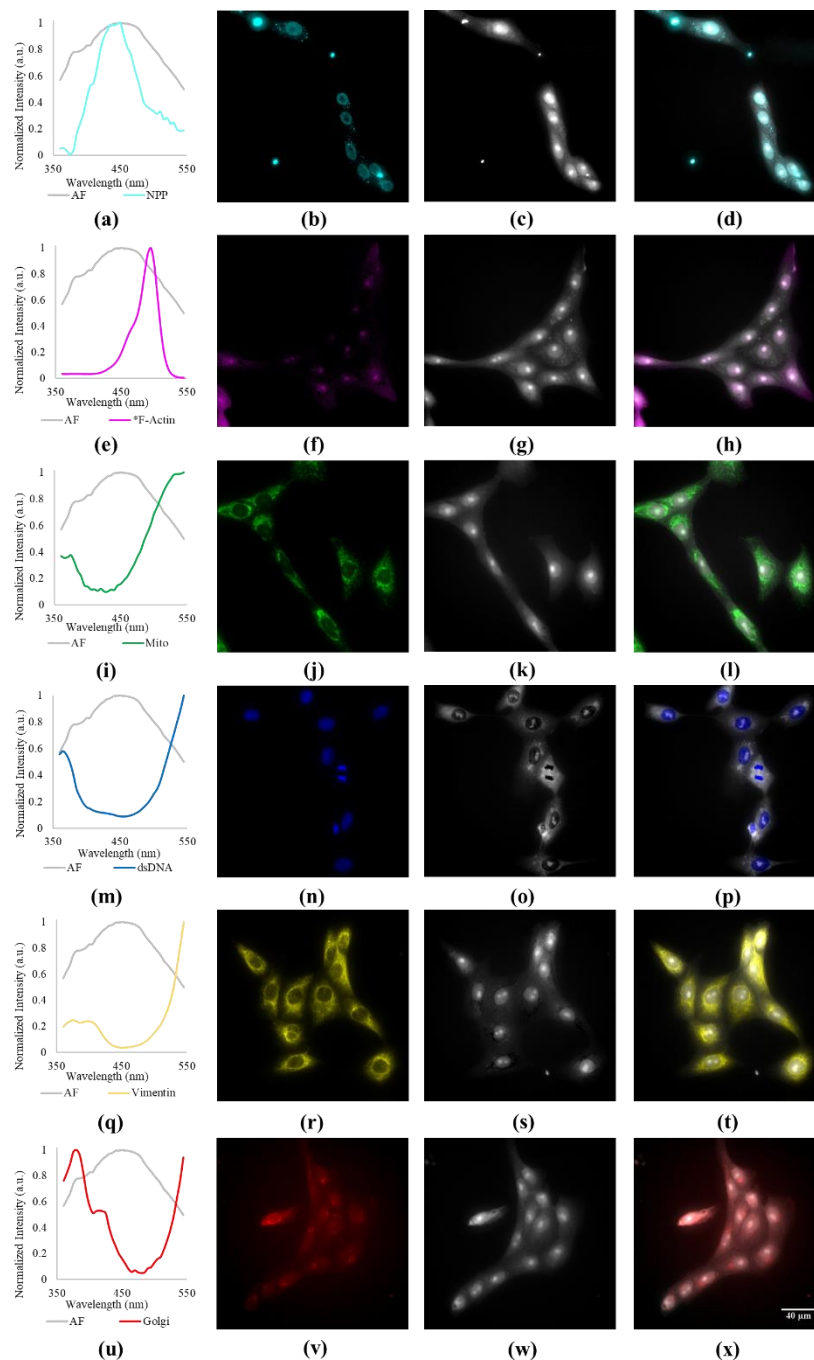


Figure A7. Validation of spectral specificity for the TFTF-based system. Endmember spectra for each fluorescent label were acquired from single labeled control slides, a region was drawn, the region-averaged spectrum extracted, and a 2-component spectral library containing the spectrum of the label and the spectrum of autofluorescence defined (column 1). The 2-component library was used with non-negatively constrained linear unmixing to identify the signal (abundance) from the label of interest and autofluorescence (columns 2 and 3, respectively). The unmixed fluorescent label image was false-colored and merged with the autofluorescence image to allow visualization of both components in a composite image (column 4).

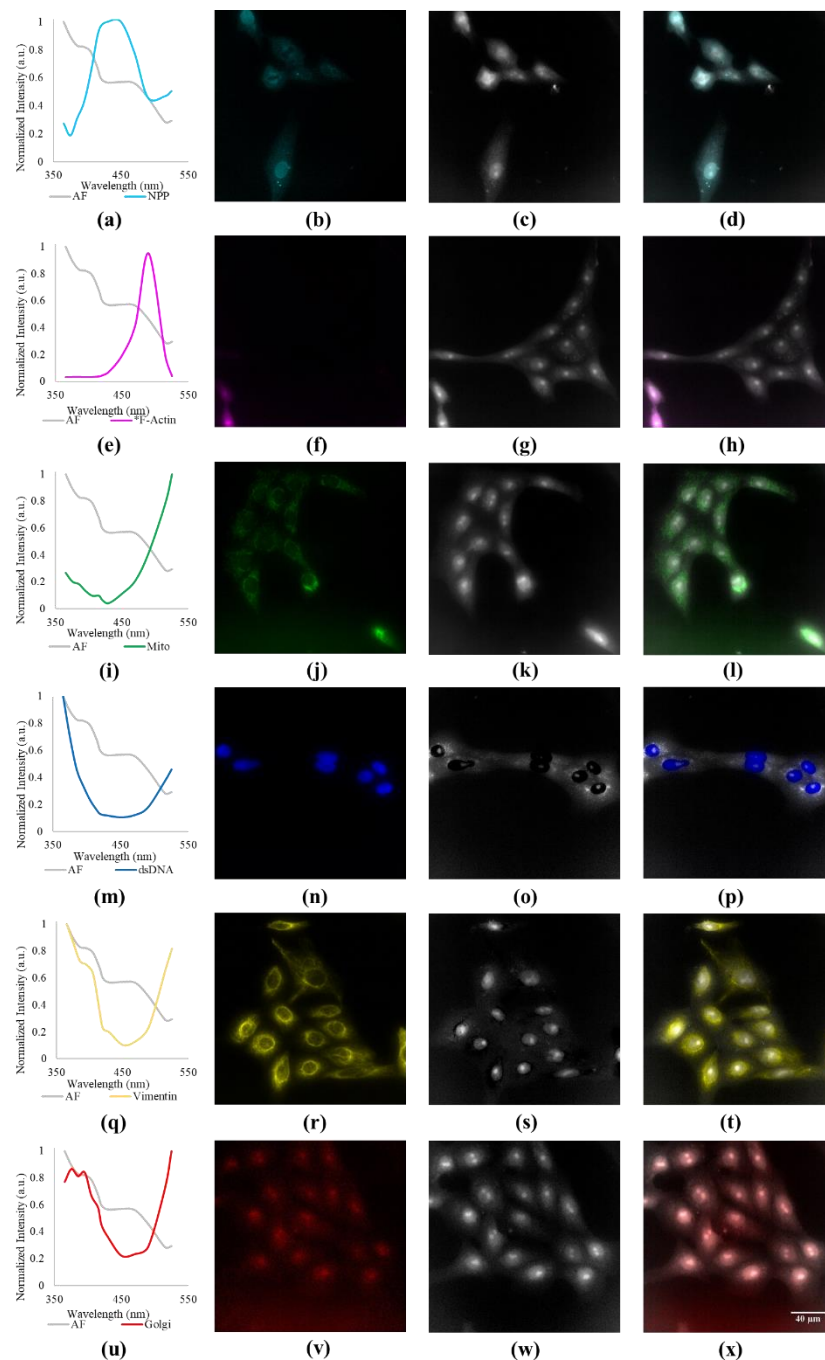


Figure A8. Validation of spectral specificity for the LED-based system. Endmember spectra for each fluorescent label were acquired from single labeled control slides, a region was drawn, the region-averaged spectrum extracted, and a 2-component spectral library containing the spectrum of the label and the spectrum of autofluorescence defined (column 1). The 2-component library was used with non-negatively constrained linear unmixing to identify the signal (abundance) from the label of interest and autofluorescence (columns 2 and 3, respectively). The unmixed fluorescent label image was false-colored and merged with the autofluorescence image to allow visualization of both components in a composite image (column 4).

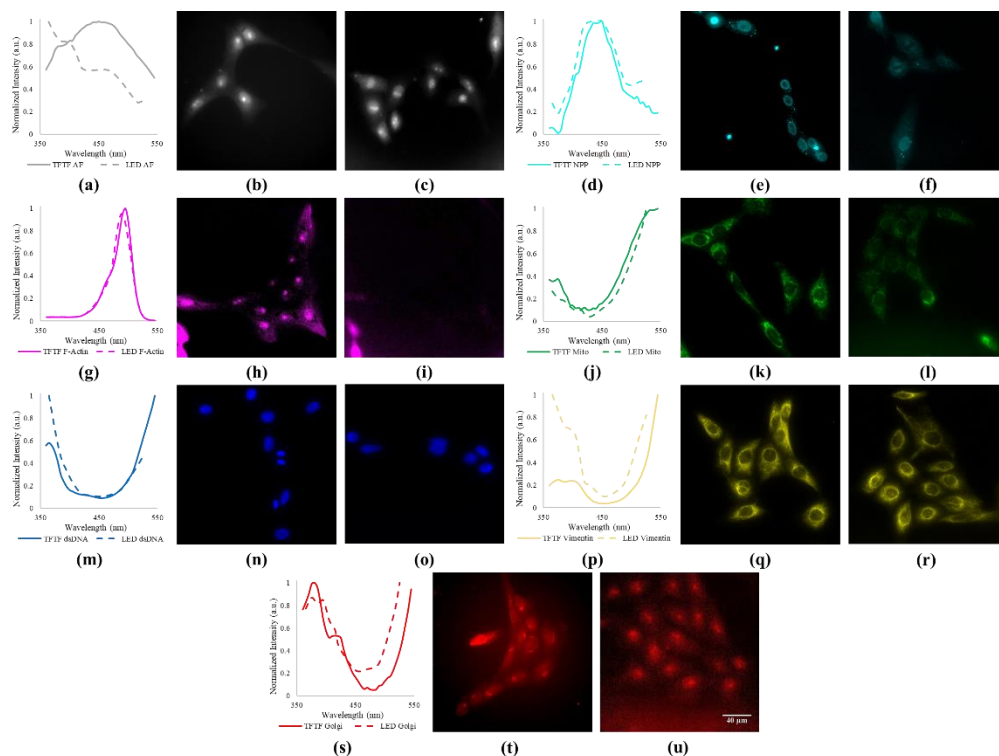


Figure A9. Comparison of individual endmember spectra utilized for linear unmixing for the TFTF-based system and the LED-based system. Each fluorescent label is represented in 3 panels: the first panel is a graphical comparison of normalized spectra of the endmember for both the TFTF- (solid line) and LED-based (dashed line) systems, the second panel is the unmixed fluorescent label image acquired through the TFTF-based system when using the respective 2-component library shown in Figure A7 and the third panel is the unmixed label image acquired through the LED-based system when using the respective 2-component library shown in Figure A8. The fluorescent labels include: (a-c) autofluorescence, (d-f) NPP, (g-i) f-actin, (j-l) mitochondria, (m-o) dsDNA, (p-r) vimentin and (s-u) Golgi.

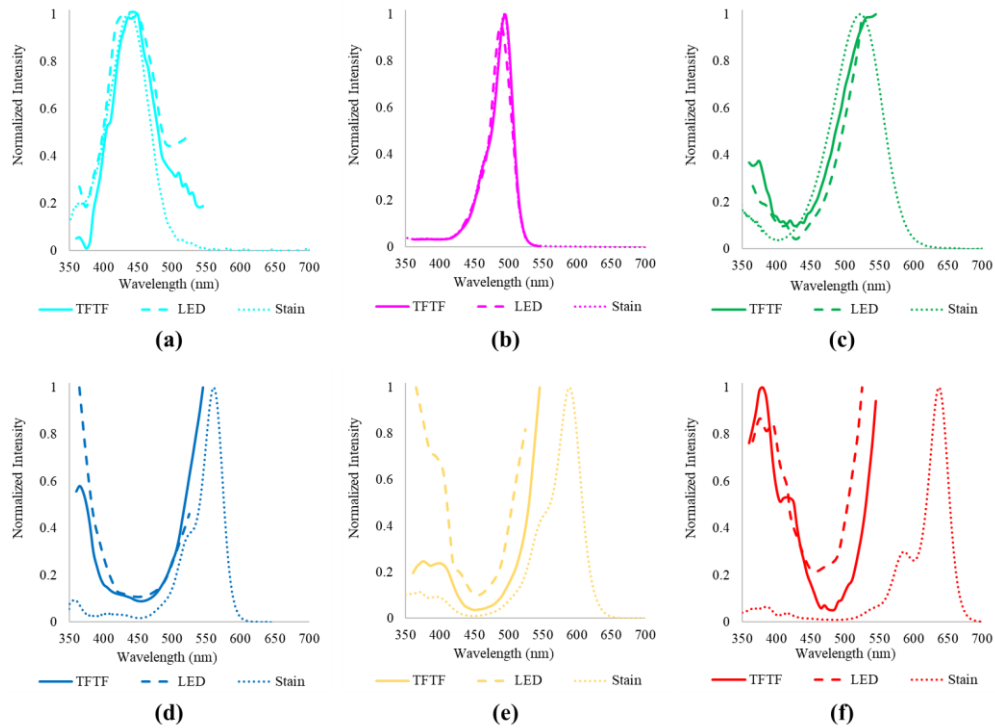


Figure A10. A comparison of manufacturer-supplied spectral data and measured excitation spectrum using both the TFTF- and LED-based spectral light sources. The labels include: (a) STAR440XSP (nuclear pore protein), (b) STAR GREEN (f-Actin), (c) STAR520SXP (mitochondria), (d) LIVE560 (double stranded DNA), (e) STAR ORANGE (vimentin) and (f) STAR RED (Golgi apparatus). Note that spectral images from the f-actin single label slide were highly contaminated with cellular autofluorescence, and hence it was not possible to identify a region corresponding to pure f-actin signal. Because of this, the pure spectrum of f-actin was instead taken from manufacturer-supplied data and normalized intensity values were extracted for every wavelength channel scanned with both spectral light sources. The LED-based “signal” resulted in a 13 point spectrum causing the skew to the left compared to the TFTF-based “signal” and the manufacturer-supplied spectral data. The excitation spectral scan range for labels (d-f) did not include the peak excitation wavelength for the fluorescent label and hence only a partial spectrum of the fluorescent label was shown, however, each spectrum is normalized to its respective highest value and local maximums were different. The shape (therefore the spectrum) comparison between the two spectral light source setups and the manufacturer-supplied spectral data is in high agreement despite the opposing local maximums.

Appendix C: Copyright Permission

Optica Publishing Group: Because you are the author of the source paper from which you wish to reproduce material, Optica Publishing Group considers your requested use of its copyrighted materials to be permissible within the author rights granted in the Copyright Transfer and Open Access Publishing Agreement submitted by the requester on acceptance for publication of his/her manuscript. It is requested that a complete citation of the original material be included in any publication. This permission assumes that the material was not reproduced from another source when published in the original publication. If the entire article is being included, it is permissible to use the version of record.

https://opg.optica.org/submit/review/copyright_permissions.cfm?source=authornav§ion=oa_posting#posting

MDPI: No special permission is required to reuse all or part of article published by MDPI, including figures and tables. For articles published under an open access Creative Common CC BY license, any part of the article may be reused without permission provided that the original article is clearly cited. Reuse of an article does not imply endorsement by the authors or MDPI.

<https://www.mdpi.com/openaccess>

BIOGRAPHICAL SKETCH

BIOGRAPHICAL SKETCH

Name of Author: Craig M. Browning

Graduate and Undergraduate Schools Attended:

University of South Alabama, Mobile, Alabama

Degrees Awarded:

Bachelor of Science in Chemical Engineering, 2016, Mobile, Alabama

Master of Science in Chemical Engineering, 2018, Mobile, Alabama

Doctorate of Philosophy in Systems Engineering, 2022, Mobile, Alabama

Awards and Honors:

Alabama Space Grant Consortium Fellowship – University of Alabama in Huntsville (2019-2022)

Outstanding Thesis of the Year Award Nominee – University of South Alabama (2018-2019)

Cyto Student Travel Award – ISAC International Congress (2018)

GSAEP Travel Award – University of South Alabama (2018)

Graduate Assistantship – University of South Alabama Systems Engineering (2016-2018)

SPIE Student Travel Award - Photonics West (2017)

Cameron Davis Chick-fil-A Scholarship – Spanish Fort, AL Chick-fil-A (2017)

USA Presidential Scholarship – University of South Alabama (2011-2013)

Chick-fil-A Leadership Scholarship – Chick-fil-A (2011)

Journal Publications:

Browning, C.M., Cloutier, R., Rich, T.C., and Leavesley, S.J., “Endoscopy Lifetime Systems Architecture: Scoping Out the Past to Diagnose the Future Technology,” *Systems* 10(5), (2022).

Browning, C.M., Mayes, S., Mayes, S.A., Rich, T.C., and Leavesley, S.J., “Microscopy is better in color: development of a streamlined spectral light path for real-time multiplex fluorescence microscopy,” *Biomedical Optics Express* 13(7), 3751 (2022).

C. M. Browning, J. Deal, S. Mayes, A. Arshad, T. C. Rich, and S. J. Leavesley, "Excitation-scanning hyperspectral video endoscopy: enhancing the light at the end of the tunnel," *Biomed. Opt. Express* 12, 247 (2021).

Joshua Deal, Sam Mayes, **Craig Browning**, Shante Hill, Paul Rider, Carole Boudreaux, Thomas C. Rich, Silas J. Leavesley, "Identifying molecular contributors to autofluorescence of neoplastic and normal colon sections using excitation-scanning hyperspectral imaging," *J. Biomed. Opt.* 24(2), 021207 (2019), doi: 10.1117/1.JBO.24.2.021207.

Conference Publications:

Parker, M., Mayes, S.A., **Browning, C.M.**, Deal, J., Gunn-Mayes, S., Rich, T.C., and Leavesley, S.J., “Validation of excitation-scan hyperspectral multi-faceted mirror array prototype system advancements to hyperspectral imaging applications,” presented at Three-Dimensional and Multidimensional Microscopy: Image Acquisition and Processing XXIX, 2022, 27–32.

Browning, C.M., Parker, M., Rich, T.C., and Leavesley, S.J., “Illuminating the optical properties of an LED-based spectral light source for hyperspectral endoscopy,” presented at Optical Biopsy XIX: Toward Real-Time Spectroscopic Imaging and Diagnosis, 2021, 1163608.

Browning, C.M., Deal, J., Mayes, S.G., Parker, M., Rich, T.C., and Leavesley, S.J., “Optical simulations for determining efficacy of new light source designs for excitation-scanning high-speed hyperspectral imaging systems,” presented at Multiscale Imaging and Spectroscopy, 2020, 112160W.

Deal, J., Annamdevula, N., Pleshinger, D.J., Griswold, J.R., Odom, A., Tayara, A., Lall, M., **Browning, C.**, Parker, M., et al., “Comparison of spectral FRET microscopy approaches for single-cell analysis,” presented at Imaging, Manipulation, and Analysis of Biomolecules, Cells, and Tissues XVIII, 2020, 112430Y.

Parker, M., **Browning, C.M.**, Mayes, S.A., Deal, J., Gunn-Mayes, S., Rich, T.C., and Leavesley, S.J., “Excitation-scan mirror array system advancements to hyperspectral imaging applications,” presented at Three-Dimensional and Multidimensional Microscopy: Image Acquisition and Processing XXVII, 2020, 112450Y.

Mayes, S.G., **Browning, C.**, Mayes, S.A., Parker, M., Rich, T.C., and Leavesley, S.J., “Spectral illumination system utilizing spherical reflection optics,” presented at Imaging, Manipulation, and Analysis of Biomolecules, Cells, and Tissues XVIII, 2020, 112430L.

Browning, C. M., Mayes, S., Deal, J., Arshad, A., Mayes, S. G., Parker, M., Rich, T. C. and Leavesley, S. J., “Sensitivity analysis of a multibranching light guide for real time hyperspectral imaging systems,” presented at Multimodal Biomedical Imaging XIV, 2019, 1087107, International Society for Optics and Photonics.

Leavesley, S. J., Griswold, J. R., Deal, J., McAlister, K., Mayes, S., **Browning, C.**, Parker, M., Mayes, S. G. and Rich, T. C., “Hyperspectral imaging fluorescence excitation scanning (HIFEX) microscopy for live cell imaging,” presented at Three-Dimensional and Multidimensional Microscopy: Image Acquisition and Processing XXVI, 2019, 108831A, International Society for Optics and Photonics.

Mayes, S. G., Mayes, S. A., **Browning, C.**, Parker, M., Rich, T. C. and Leavesley, S. J., “A spherical mirror-based illumination system for fluorescence excitation-scanning hyperspectral imaging,” presented at Imaging, Manipulation, and Analysis of Biomolecules, Cells, and Tissues XVII, 2019, 108810N, International Society for Optics and Photonics.

Parker, M., **Browning, C. M.**, Rich, T. C. and Leavesley, S. J., “Optimization of light transmission through an excitation-scan hyperspectral mirror array system,” presented at Imaging, Manipulation, and Analysis of Biomolecules, Cells, and Tissues XVII, 2019, 108810O, International Society for Optics and Photonics.

Rich, T. C., Griswold, J., Deal, J., Annamdevula, N., McAlister, K., Mayes, S., **Browning, C.**, Parker, M. and Leavesley, S. J., “Hyperspectral imaging microscopy for measurement of localized second messenger signals in single cells,” presented at Imaging, Manipulation, and Analysis of Biomolecules, Cells, and Tissues XVII, 2019, 108811F, International Society for Optics and Photonics.

Browning, C.M., Mayes, S., Rich, T.C., and Leavesley, S.J., “Endoscopic hyperspectral imaging: light guide optimization for spectral light source,” presented at Multimodal Biomedical Imaging XIII, SPIE BIOS, 2018, 104870H.

Mayes, S.A., Moore, K., **Browning, C.M.**, Klomkaew, P., Rich, T.C., and Leavesley, S.J., “Applications and assessment of an excitation-scanning hyperspectral imaging system,” presented at Imaging, Manipulation, and Analysis of Biomolecules, Cells, and Tissues XVI, SPIE BIOS, 2018, 1049706.

Browning, C.M., Mayes, S., Rich, T.C., and Leavesley, S.J., “Design of a modified endoscope illuminator for spectral imaging of colorectal tissues,” presented at Optical Biopsy XV: Toward Real-Time Spectroscopic Imaging and Diagnosis, SPIE BIOS, 2017, 1006015.

Browning, C.M., Mayes, S., Favreau, P., Rich, T.C., and Leavesley, S.J., “LED-based endoscopic light source for spectral imaging,” presented at Optical Biopsy XIV: Toward Real-Time Spectroscopic Imaging and Diagnosis, SPIE BIOS, 2016, 97031I.